Version 1

The MultiPurpose Detector (MPD) to study Heavy Ion Collisions at NICA

Letter of Intent

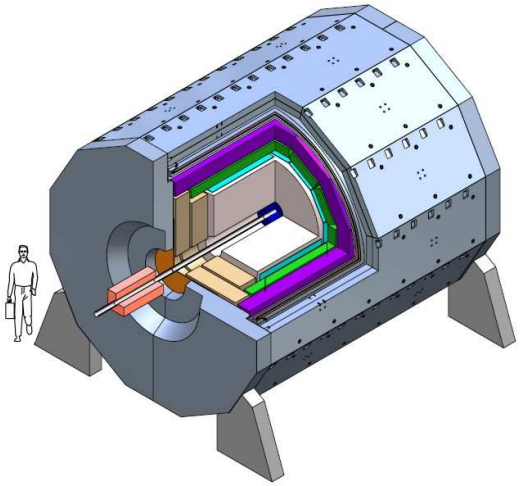

Dubna, 2008

The MultiPurpose Detector – MPD

to study Heavy Ion Collisions at NICA
(Letter of Intent)

Project leaders: A.N. Sissakian, A.S. Sorin, V.D. Kekelidze

The MPD Collaboration:[1]

H.U. Abramyan, S.V. Afanasiev, N.N. Agapov, N.V. Anfimov, D.A. Arkhipkin, V.A. Babkin, S.N. Bazylev, I.V. Boguslavski, V.V. Borisov, S.P. Chernenko, V.F. Chepurnov, G.A. Cheremukhina, D.E. Donetz, K.I. Davkov, V.I. Davkov, D. Drnojan, E. Egorov, O.V. Fateev, Yu.I. Fedotov, V.M. Golovatyuk, Yu. Gorbunov, N.S. Grigalashvili, Yu.A. Gornushkin, A.Yu. Isupov, V. Jejer, G.D. Kekelidze, V.D. Kekelidze, V.A. Kizka, A.D. Kovalenko, N. Krahotin, Yu.T. Kiryushin, Z.V. Krumshtein, H.G. Khodzhibagiyan, R. Lednicky, A.G. Litvinenko, E.I. Litvinenko, S.P. Lobastov, V.M. Lysan, J. Lukstins, V.M. Lucenko, D.T. Madigozhin, A.I. Malakhov, I. Manjavidze, I.N. Meshkov, V.V. Mialkovski, I.I. Migulina, N.A. Molokanova, Yu.A. Murin, G. Musulmanbekov, V.A. Nikitin, A.G. Olchevski, V.F. Peresedov, D.V. Peshekhonov, V.D. Peshekhonov, I.A. Polenkevich, Yu.K. Potrebenikov, V.S. Pronskikh, A.M. Raportirenko, S.V. Razin, O.V. Rogachevsky, A.B. Sadovsky, Z.Ja. Sadygov, A.A. Savenkov, B.G. Shchinov, A.V. Shabunov, A.O. Sidorin, V.V. Skokov, I.V. Slepnev, V.M. Slepnev, A.N. Sissakian, A.S. Sorin, V.D. Toneev, T.P. Topuria, G.V. Trubnikov, I.A. Tyapkin, N.M. Vladimirova, S.V. Volgin, Yu.V. Zanevsky, A.I. Zinchenko, V.N. Zrjuev, R.Ya. Zulkarneev, Yu.R. Zulkarneeva
Joint Institute for Nuclear Research, Dubna, Russian Federation

M.B. Golubeva, F.F. Guber, A.P. Ivashkin, T.L. Karavicheva, A.B. Kurepin, A.I. Maevskaya, V.A. Matveev, A.I. Reshetin
Institute for Nuclear Research, Russian Academy of Sciences, Moscow, Russian Federation

G.M. Zinovjev
Bogolyubov Institute for Theoretical Physics, National Academy of Sciences, Kiev, Ukraine

A.I. Demianov, A.A. Ershov, A.M. Gribushin, L.V. Malinina, L.I. Sarycheva, V.I. Savrin
Nuclear Physics Institute of Moscow State University, Moscow, Russian Federation

M.I. Baznat, K.K. Gudima
Institute of Applied Physics, Academy of Sciences of Moldova, Chisinau, Republic of Moldova

[1]The list of participating Institutes is currently a subject of update.

Abstract

A conceptual design of the MultiPurpose Detector (MPD) is proposed for a study of hot and dense baryonic matter in collisions of heavy ions over atomic mass range A = 1–238 at a centre-of-mass energy up to $\sqrt{s_{NN}} = 9\ GeV$ (for U^{92+}). The MPD experiment is foreseen to be carried out at a future JINR accelerator complex facility for heavy ions – the Nuclotron-based Ion Collider fAcility (NICA) which is designed to reach the required parameters with an average luminosity of $L = 10^{27}\mathrm{cm}^{-2}\mathrm{s}^{-1}$.

Contents

Introduction

Investigation of hot and dense baryonic matter is a challenging task in modern physics. It provides information on the in-medium properties of hadrons and nuclear matter equation of state, allows a search for possible manifestations of the deconfinement and/or chiral symmetry restoration, phase transition, mixed phase and critical end point, as well as sheding light on the evolution of the Early Universe and formation of neutron stars.

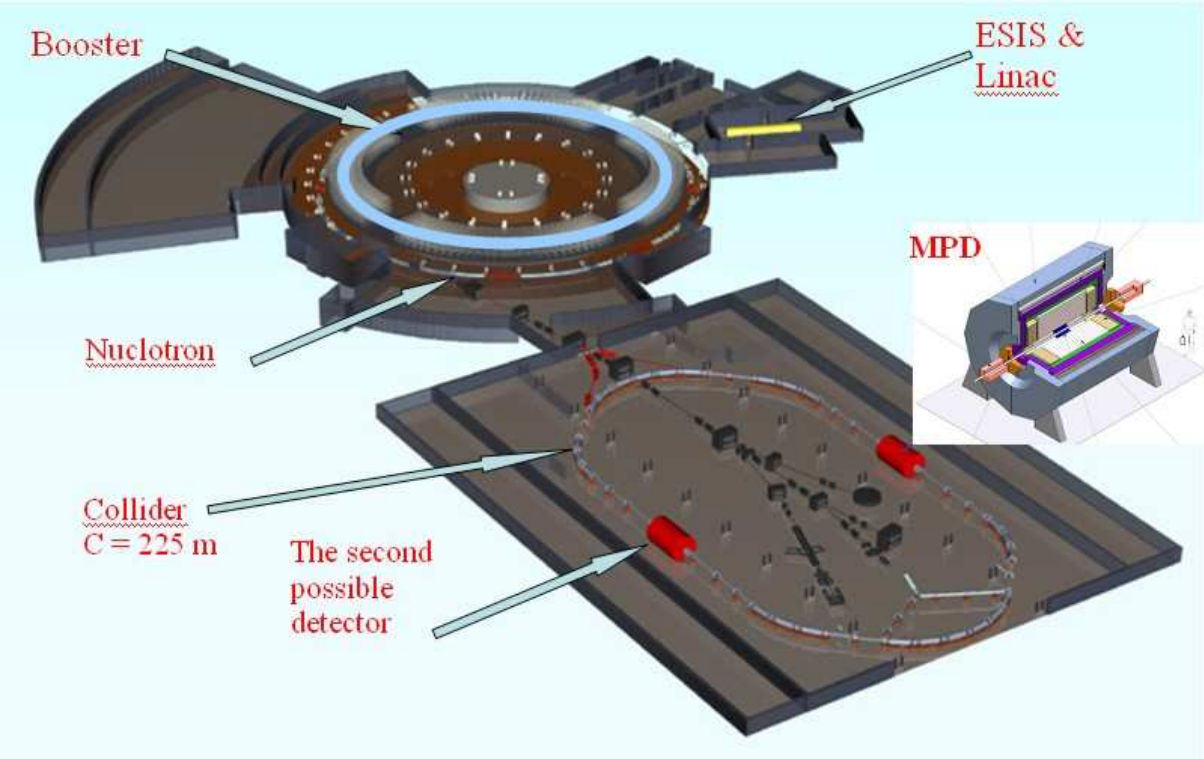

Fig. 1: The location of the NICA collider in the JINR accellerator complex area.

An essential part of the JINR scientific program resulting from many discussions in view of the Dubna Nuclotron upgrade is dedicated to the study of hot and dense baryonic matter [1, 2, 3, 4]. Realization of this ambitious goal is related to the construction of a new JINR accelerator complex – the Nuclotron-based Ion Collider fAcility (NICA) [5] providing collisions of heavy ions over a large range of atomic masses from Uranium+Uranium at the centre-of-mass energy $\sqrt{s_{NN}} = 9\ GeV$ (for U^{92+}) and an average luminosity of $L = 10^{27}\mathrm{cm}^{-2}\mathrm{s}^{-1}$ to proton-proton collisions with $\sqrt{s_{pp}} = 20\ GeV$ and $L \approx 10^{30} cm^{-2} s^{-1}$. The NICA collider will be located in the existing experimental hall in the building 205 at the Joint Institute for Nuclear Research (JINR) (Fig. 1). Two interaction points are foreseen at the NICA collider, which provides a possibility for two detectors to be operated simultaneously. One of these detectors, the MultiPurpose Detector (MPD), is optimized for the study of heavy-ion collisions and the search for manifestations of the possible phase transition, mixed phase and critical end point.

Chapter 1

Physics Overview

1.1 Physics Goals

To search for new phenomena in heavy ion collisions, it is necessary to explore the phase diagram of the strongly interacting matter in the region of highly compressed baryonic matter. This matter exists in neutron stars and in the cores of supernova explosions, while in the early Universe one meets the opposite conditions of very high temperature (T) and vanishing baryonic density (μ_B). In terrestrial experiments, high-density nuclear matter can be transiently created in a certain reaction volume in relativistic heavy ion collisions. In these collisions a large fraction of the beam energy is spent for hadron production, including excited resonances whose properties may be noticeably modified by the surrounding hot and dense medium. At very high temperatures or densities, the hadron mixture melts and its constituents, quarks and gluons, form a new phase of matter, the quark-gluon plasma. The various phases of strongly interacting matter are shown in the phase diagram in Fig. 1.1.

As is seen from this phase diagram, several heavy-ion experiments at CERN-SPS, BNL-RHIC and CERN-LHC probe the region of high temperatures and low net baryon densities, where circumstantial evidence was obtained for a new phase of matter existing above the temperature $T \sim 160 - 170$ MeV. In another region of the phase diagram, at lower temperature T and moderate baryonic density μ_B, the GSI-SIS experiments definitely show no hint of a phase transition but certainly there are in–medium modification effects. At very high μ_B and very low T the matter is deconfined and, as predicted, correlated quark-antiquark pairs form a colour superconductive phase. This phase may be formed in the interior of neutron stars.

One of the most interesting regions of the phase diagram is the intermediate one, where essential evidence was obtained by the NA49 collaboration at CERN-SPS that the hadronic system enters a new phase at a beam energy of about 30 AGeV. A fascinating particularity of this energy range is a critical end point located, according to recent lattice Quantum Chromodynamics (QCD) calculations, at temperature $T_E = (162 \pm 2)$ MeV and baryonic chemical potential $\mu_E = (360 \pm 40)$ MeV [8], while model predictions are very spread covering the area of $T_E \approx 50 - 170$ MeV and $\mu_E \approx 200 - 1400$ MeV [9]. The importance of these conclusions is emphasized in the GSI scientific programs. Thus, the CBM (Compressed Baryon Matter) experiment to study baryonic matter in this promising region of the phase diagram was proposed within the FAIR program. The same approach was recently proposed in the BNL-RHIC experiments, where it was suggested to decrease the RHIC beam energy $\sqrt{s_{NN}}$ to reach this domain of the phase diagram. The low-energy RHIC at BNL [10, 11], the CBM@FAIR at GSI [12, 13], the proposed NICA/MPD at JINR, and the ongoing work at the CERN-SPS [14, 15] with lighter systems can be considered as complementary facilities aimed at the study of relevant physics problems of hot and dense baryonic matter by various experimental techniques.

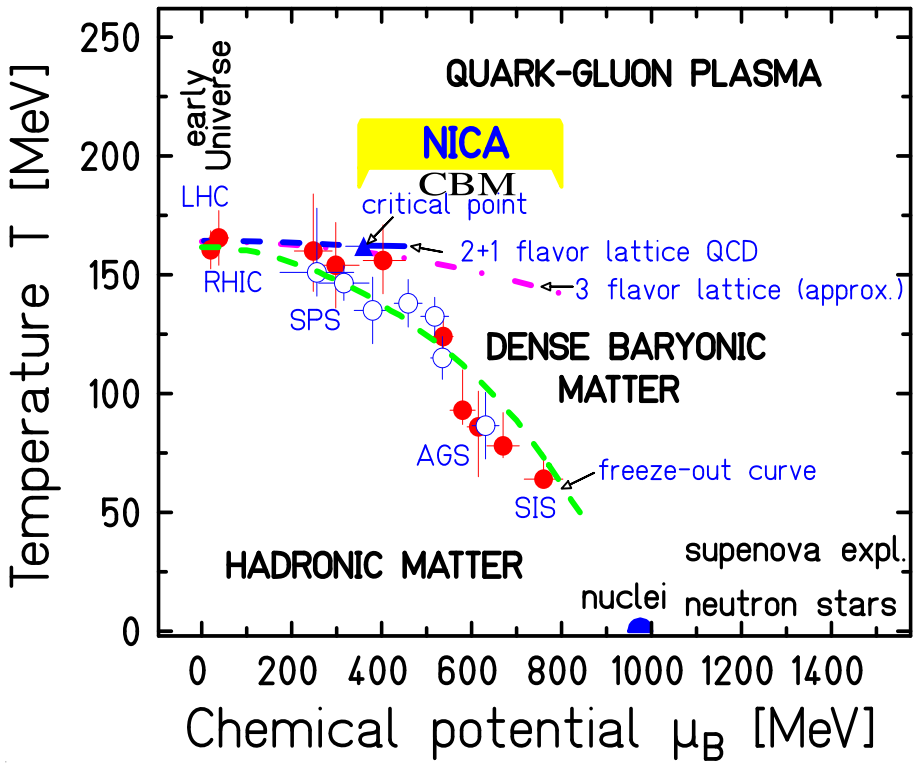

Fig. 1.1: The phase diagram of strongly interacting QCD matter. The symbols represent freeze-out points obtained with a statistical model analysis of particle ratios measured at the mid rapidity (open circles) and with the 4π acceptance (filled ones) in cental heavy-ion collisions [6]. The dashed curve is the chemical freeze-out calculation at the kinetic energy per baryon ratio $E/N_B = 1$ GeV [7]. The phase boundary is shown for the $N_f = 2 + 1$ lattice QCD calculation with a critical point (triangle) at temperature $T_E = (162 \pm 2)$ MeV and baryonic chemical potential $\mu_E = (360 \pm 40)$ MeV [8]. The dot-dashed line is a parabola with the slope corresponding to the lattice predictions of $d^2T/d\mu_B^2$ of the transition line at $\mu_B = 0$.

The phase diagram translates the properties of strong interactions and their underlying theory, the QCD, into a visible pattern. In particular, such fundamental QCD phenomena as confinement and broken chiral symmetry, whose quantitative understanding is still lacking, are a challenge for future heavy-ion research. As is demonstrated in Fig. 1.2, the domain of excited dense baryonic matter accessible in the planned MPD experiment is located roughly between the dynamical trajectories presented for two colliding ions at limiting colliding energies covering the range of quasi-equilibrium states with the baryon density up to $n_B \approx 8 \cdot n_0$ (n_0 is the density of normal nuclear mater). The hadronic phase at high net baryon densities μ_B and moderate temperatures T as well as new states of matter beyond the deconfinement, chiral transition and a mixed phase may be reached in this sector of the phase diagram. Using lattice data on the temperature dependence of n_B/T^3 [8], the location of the critical point in Fig. 1.1 may be recalculated into this representation as $n_E \approx (1.5 - 2.0) \cdot n_0$. Therefore, the major goal of the MPD experiment is the study of the in-medium properties of hadrons and the nuclear matter equation of state, including a search for possible signals of deconfinement and/or chiral symmetry restoration, phase transitions and the QCD critical end point in the region of the collider energy $\sqrt{s_{NN}} = 4 - 9$ GeV (for U^{92+}). Due to the high complexity of this task and

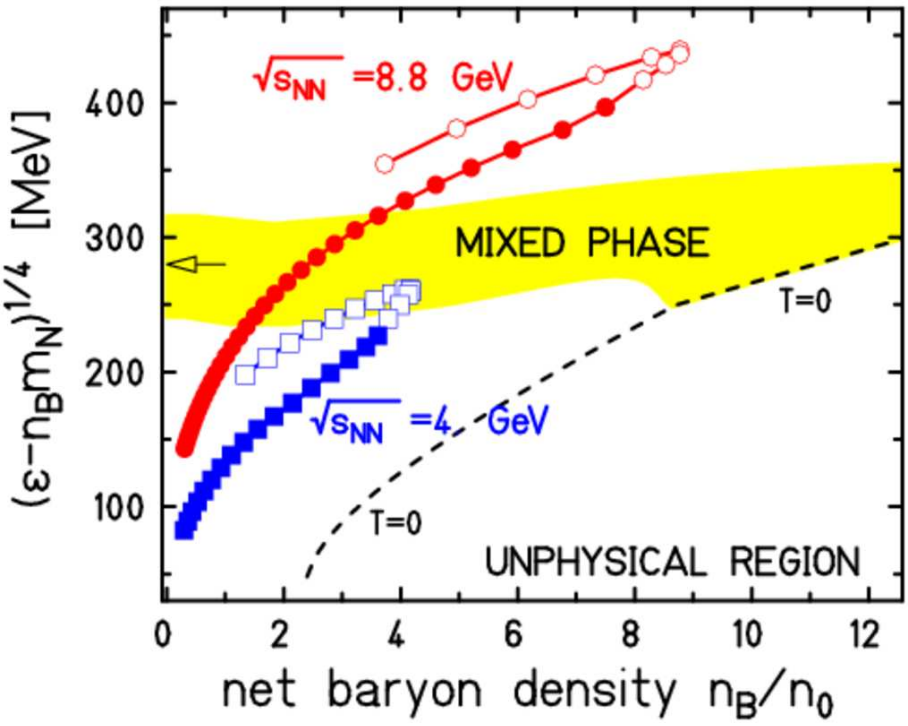

Fig. 1.2: The phase diagram in terms of the reduced energy density versus the net baryon density. The dynamical trajectories are shown for central (b = 2 fm) $Au + Au$ collisions at two limiting NICA energies. The trajectories are calculated with the hybrid model [16]. The highly nonequilibrium part of trajectories, starting from still not interacting two counter streaming flows, is evaluated within the kinetic Quark-Gluon String Model (QGSM) (open markers) and the subsequent locally equilibrium evolution is considered within the 3D relativistic hydrodynamics (filled markers). The obtained results correspond to the Lorentz-contracted cylinder of the radius R = 5 fm and the length $L = 2R/\gamma$, where γ is the centre-of-mass gamma-factor. The time differences between the points are 0.3 and 0.5 fm/c for $\sqrt{s_{NN}}$ = 8.8 and 4 GeV ($Au + Au$), respectively. The shaded region is a quark-hadron mixed phase estimated according to the phenomenological two phase EoS [17]. The dashed curve separates the unphysical region by the condition $T = 0$.

large uncertainties in the predicted signals, an accurate scanning of the considered phase diagram domain in the collision energy, impact parameter and system size is utterly needed. In this respect, one should note that it is essential to have uniform acceptance for observables over the whole energy range of interest. Operation in the collider mode, as proposed for the NICA/MPD Project, has an advantage of naturally satisfying this demand, as compared to the case of the fixed-target mode (SPS, FAIR). This advantage is inherent in low-energy RHIC program, but the RHIC luminosity planned for the low-energy exposure in 2010 is lower by 2–3 orders of magnitude than at the NICA/MPD [18].

1.2 Observables and Requirements

The MPD envisaged experimental program includes simultaneous measurements of observables that are presumably sensitive to high-density effects and phase transitions [4]. The obsevables measured on the event-by-event basis are particle yields, their phase-space distributions, correlations, and fluctuations. Different species probe different stages of the nucleus-nucleus interaction due to their differences in mass, energy, and interaction cross

sections. Heavy hadrons containing strange quarks are of particular interest: they are produced at the early high-temperature and high-density stage, but may decouple soon due to their interaction with the surrounding matter.

Among various characteristics the elliptic flow deserves special attention because this collective motion is formed mainly at the early stage of the collision. The space-time information on the particle freeze-out source, which depends on the preceding evolution of the system, is provided by the measurement of identical particle interference. Certainly, the direct information on hot and dense transient matter is provided by penetrating probes, photons and leptons. In this respect, the vector mesons, which provide information on the chiral symmetry restoration, are very attractive. An exciting possibility is opened by the study of the dilepton decay of hadrons with charm quarks. Charmonium, a charm-anticharm pair, disintegrates much easier in passing through quark-gluon matter than through hadron matter and, thereby, probes the phase structure of the formed system.

At the first stage the experiment will be focused on:

- **multiplicity and spectral characteristics** of the identified hadrons, including strange particles, multi-strange baryons and antibaryons characterizing entropy production and system temperature at the final interaction stage;
- **event-by-event fluctuations** in multiplicity, charges, transverse momenta and K/π ratios as generic properties of critical phenomena;
- **collective flows** (directed, elliptic, and higher ones) for observed hadrons including strange particles driven by the pressure in the system;
- **interferometry** with identified particles (femtoscopy) and HBT (Hanbury-Brown and Twiss) particle correlations [19, 20].

At the second stage of the experiment, the electromagnetic probes (photons and dileptons) will be used to study heavy ion interactions.

The MPD detector will be operated at an interaction rate of about $6 \cdot 10^3$ interactions per second with multiplicities up to 1400 charged particles per central $Au + Au$ collision at the maximum energy.[1]

Taking into account that short-lived vector mesons decay into lepton pairs with branching ratios of $10^{-4} - 10^{-5}$ and the mean multiplicity of ρ^0 mesons at $\sqrt{s_{NN}} = 9\ GeV$ $(Au + Au)$ is ≈ 10, one could obtain about one dilepton pair per second produced via this channel. The major issue is to suppress the physical background of electron-positron pairs from Dalitz decays and photon conversions.

An estimate of the multi-strange hyperons is quite model dependent. For example, the multiplicities of Ω baryons at the maximal colliding energy are approximately 0.6 and 0.1 for the central and minimum bias events, respectively. This results in production rates of 700/s and 200/s for 5% centrality and a minimum-bias collision, respectively. When one proceeds to the lowest colliding energy $\sqrt{s_{NN}} = 4\ GeV$ (for U^{92+}), these numbers

[1] Note that the CBM will have a reaction rate of up to $10^7/s = 10$ MHz with charged hadron multiplicities up to ~ 1000, so we lose more than three orders of magnitude in intensity. However, this noticeably simplifies demands of the fast operating MPD system. As to the low-energy RHIC [18], the cited BBC rates (i. e. events triggered by the BBC detector) are 100–700 Hz at the peak luminosity $1.5 \cdot 10^{24}$ for $\sqrt{s_{NN}} = 9.2$ GeV $(Au + Au)$. It means that the NICA/MPD advantage over RHIC is less than two orders of magnitude instead of three orders expected from a direct comparison of the luminosity values.

decrease by two orders of magnitude. So a decrease in luminosity at this energy by more than an order of magnitude may be quite crucial.

Energy dependence of antiproton production is stronger than that of the Ω hyperon production. In central $U + U$ collisions at $\sqrt{s_{NN}} = 4\ GeV$ the proton yield is two times lower but at $\sqrt{s_{NN}} = 9\ GeV$ it is by a factor of four larger than that for Ω hyperons. It is obvious that the geometrical acceptance, trigger efficiency, and particularities of the channel considered should be taken into account to estimate the required beam time.

One of the most promising observables that could serve as a sensitive diagnostic probe in the energy range considered is the strangeness-to-entropy ratio which can be evaluated through the kaon-to-pion and/or Lambda-to-pion ratios, as well as the multiplicity fluctuations, femtoscopic correlations, and collective flows of identified hadrons. A study of these observables allows extracting information on the nuclear equation of state for baryonic matter at high densities. To search for these effects, one should estimate a priori the kinematic characteristics of the produced particles, and then consider their peculiarities and trace their energy dependence. What the geometry parameters of the setup should be like to allow the study of the expected effects? The planned parameters of the MPD lead to the following restrictions for the kinematic characteristics of the emitted particles: $-1 < \eta < 1$ and $|p| > 100$ MeV. These parameters satisfy the objectives of the investigations proposed above for the first step of the experiment. At high densities and/or temperatures strange particles originating at the early stage of the collision process should have rather high transverse momenta. The elliptic flow of the strange and non-strange hadronic matter is essential at mid-rapidity. Correlations of identical particles are not so sensitive to the above kinematic restrictions. The observables affected by these restrictions are the charged multiplicity fluctuations and the yield of strange and multistrange baryons in the forward and backward rapidity space.

Table 1.1: Mean Multiplicities in $Au + Au$ minimum bias events.

$\sqrt{s}$, GeV	All	Charged	Protons	π^-	π^+	K^+	K^-
3	279.6	130.5	68.62	17.76	12.63	0.5206	0.0261
5	610.8	296.8	76.20	61.31	50.81	4.548	0.9366
7	876.2	424.5	80.62	95.66	83.06	7.758	2.471
9	1067	515.6	83.27	120.7	107.1	10.03	4.006

The $Au + Au$ inelastic collisions in the energy range from $\sqrt{s_{NN}} = 3$ GeV to 9 GeV were generated by means of the UrQMD code (version 1.3). The mean multiplicities of the produced particles are presented in Tables 1.1 and 1.2. Multiplicities in the whole kinematic region are given for both minimum bias and central events. For central events multiplicities in the kinematic region restricted by the detector acceptance are also shown. Strong decays of all resonances are taken into account. Figures 1.3 and 1.4 represent the multiplicity and pseudorapidity distributions of charged particles, respectively.

A pronounced peak of the K^+/π^+ ratio was found by the CERN-NA49 collaboration in central $Pb + Pb$ collisions at a beam energy of 30 AGeV. This structure cannot be explained by any of the available theoretical models (see Fig. 1.5).

The lambda/pion ratio exhibits a similar maximum at the same beam energy. The experimental task is to identify strange hadrons, in particular, Λ, Ξ, Ω hyperons among

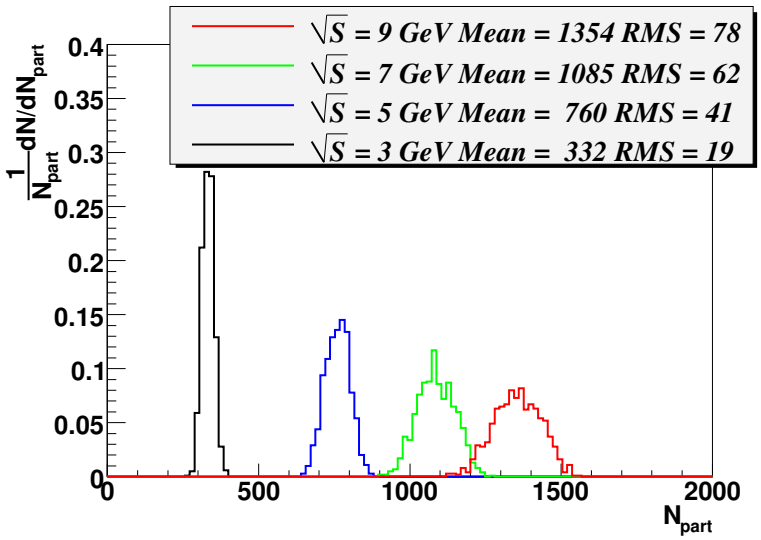

Fig. 1.3: Charged multiplicity distributions in central ($b = 0 - 3$ fm) collisions at various energies calculated by UrQMD.

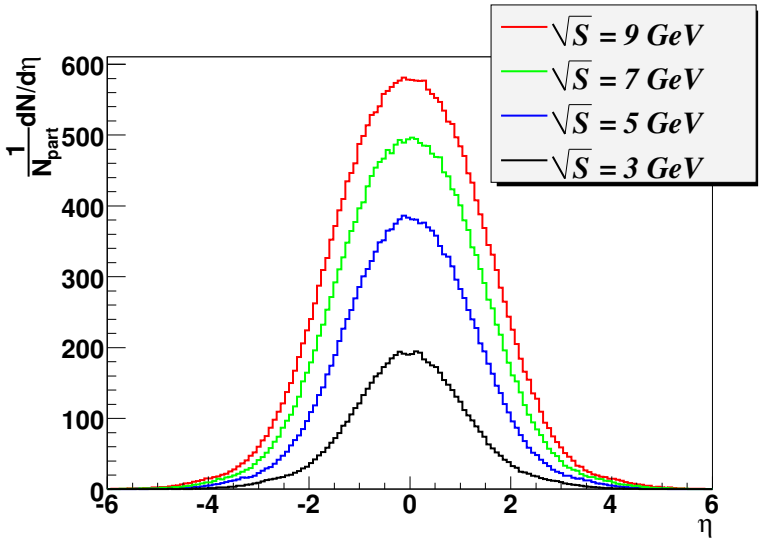

Fig. 1.4: Pseudorapidity distributions of charged particles in central ($b = 0 - 3$ fm) $Au + Au$ collisions calculated by UrQMD.

Table 1.2: Central events ($b = 0 - 3$ fm).

Part.	3 GeV			9 GeV		
		$p > 100$ MeV/c			$p > 100$ MeV/c	
	All	$\|\eta\| < 1$	$\|\eta\| < 2$	All	$\|\eta\| < 1$	$\|\eta\| < 2$
Char.	305.8	196.3	281.5	1332	635.7	1076
p	176.5	114.4	167.3	238.1	99.3	176.3
π^+	51.9	33.0	46.0	474.4	236.1	391.3
π^-	71.7	45.0	62.7	530.2	259.6	433.9
π^0	64.5	40.3	56.4	573.9	280.7	469.5
K^+	3.32	2.29	3.11	49.3	22.0	40.5
K^-	0.170	0.101	0.152	18.9	9.5	16.2
K^0	3.47	2.34	3.25	68.2	32.0	56.6
Λ	3.75	2.66	3.74	40.0	17.5	32.9
Σ^+	0.881	0.616	0.880	9.10	3.95	7.48
Σ^-	1.231	0.873	1.230	9.85	4.19	8.00
Σ^0	0.873	0.621	0.873	8.72	3.71	7.11
Ξ^-	0.009	0.006	0.009	1.21	0.56	1.03
Ξ^0	0.013	0.010	0.013	1.18	0.52	0.99
Ω^-	0	0	0	0.030	0.014	0.023
K^+/π^+	0.064	0.069	0.068	0.093	0.093	0.103
K^-/π^-	.0024	.0022	.0024	0.036	0.037	0.037
$\Lambda\Sigma^0/\pi^0$	0.072	0.081	0.082	0.085	0.077	0.085

about 1400 charged particles. The geometrical acceptance of the MPD covers from 20% to 30% of lambdas.

Event-by-event multiplicity fluctuations are expected to serve as an indication of crossing the boundary of the first order phase transition where fluctuations should be large. Fluctuations in multiplicities of positive (with protons excluded), negative, and all charged particles for the events simulated by UrQMD at the zero impact parameter of $Au + Au$ collisions are shown in Fig. 1.6. The essential dependence on the geometrical restrictions is clearly seen.

The elliptic flow (v_2) defined as a coefficient of expansion of the transverse angular distribution of emitted particles with respect to the reaction plane

$$dN/d\phi \propto [1 + 2v_1 \cos(\phi) + 2v_2 \cos(2\phi)]$$

is expected to be sensitive to the early pressure gradients and, therefore, to the equation of state (EoS) of the fireball formed in heavy-ion collisions. This angular distribution is non-isotropic, and v_2 is a measure of stretching. In principle, the elliptic flow of hadrons at low transverse momenta (p_t) can be related to the degree of thermalization, viscosity, and EoS of the produced matter. However the elliptic flow of the high p_t particles is related to the jet fragmentation and energy loss of the primordially produced hard antiquark-quark pair when travelling through a hot QCD medium. At low p_t experiments indicate a gradual increase of v_2 with p_t. Thus an accurate v_2 measurement might allow a deeper insight into the bulk properties of the produced matter. At the NICA/MPD energy v_2

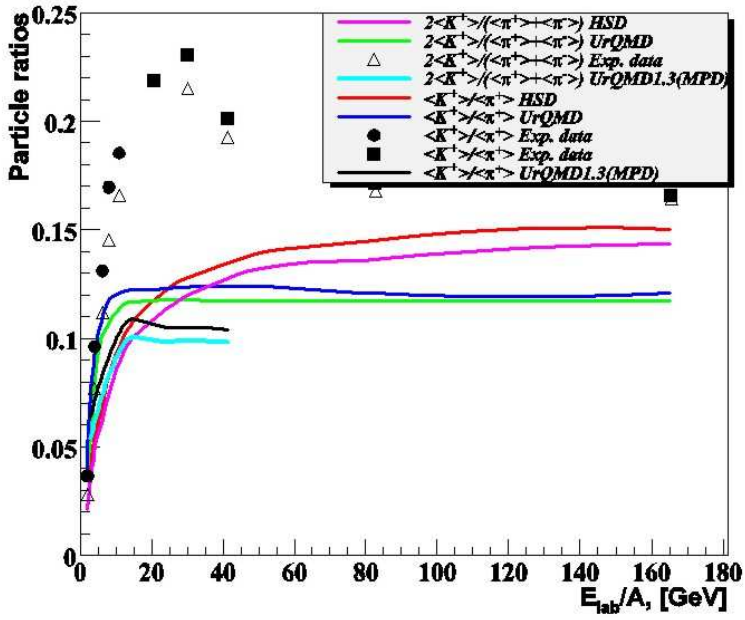

Fig. 1.5: Particle ratios for central $Au + Au$ collisions. The experimental data are from AGS [21, 22] and NA49 [23, 24] for Pb+Pb collisions. Calculations were performed by Bratkovskaya et al.

strongly depends on the collision energy and changes its sign. As is seen from Fig. 1.7, the elliptic flow shows an essentially linear dependence on the impact parameter b (for 1.5fm $< b <$ 8fm) with a negative slope at the beam energy $E_{beam} = 2$ AGeV, a positive slope at $E_{beam} = 6$ AGeV, and a near zero slope at $E_{beam} = 4$ AGeV. This dependence serves as an important constraint for discriminating between various EoS for high-density nuclear matter providing an important insight into the interplay between the collision geometry and expansion dynamics. However, experimental measurement of the elliptic flow is not a trivial task because of the uncertainty in the orientation of the reaction plane and various nonflow contributions such as the transverse momentum conservation, small angle azimuthal correlations (final state interactions), resonance decays, jet production, and quantum statistical correlations (HBT effect). Active simulations of the transverse asymmetry in both kinetic and hydrodynamic models are greatly needed as well as a study of higher orders of correlations in the transverse plane.

Information about the space-time structure of the particle emission source (fireball) can be extracted by the femtoscopy or HBT interferometry analysis. The UrQMD calculation results for the HBT-radii $R_{out}, R_{side}, R_{longitudinal}$ of the particle emission source demonstrate essential discrepancies with experiment. A good description of the SPS and RHIC data was obtained in various models based on hydro-inspired parameterizations of the freeze-out hypersurface. The HBT-radii for the NICA energy range were calculated using the fast hadron freeze-out Monte Carlo generator (FASTMC) [25]. Particles and hadronic resonances are generated on the thermal hypersurface. Figure 1.8 shows the FASTMC calculated transverse momentum dependence of the HBT radii for a pair of identical pions produced in central $Au + Au$ collisions at $\sqrt{s_{NN}} = 4$ GeV. These radii enter the correlation function (Fig. 1.9) as

$$C(q_o, q_S, q_L) = 1 + \lambda \exp(-R_L^2 q_L^2 - R_o^2 q_o^2 - R_S^2 q_S^2 - 2R_{oL}^2 q_o q_L).$$

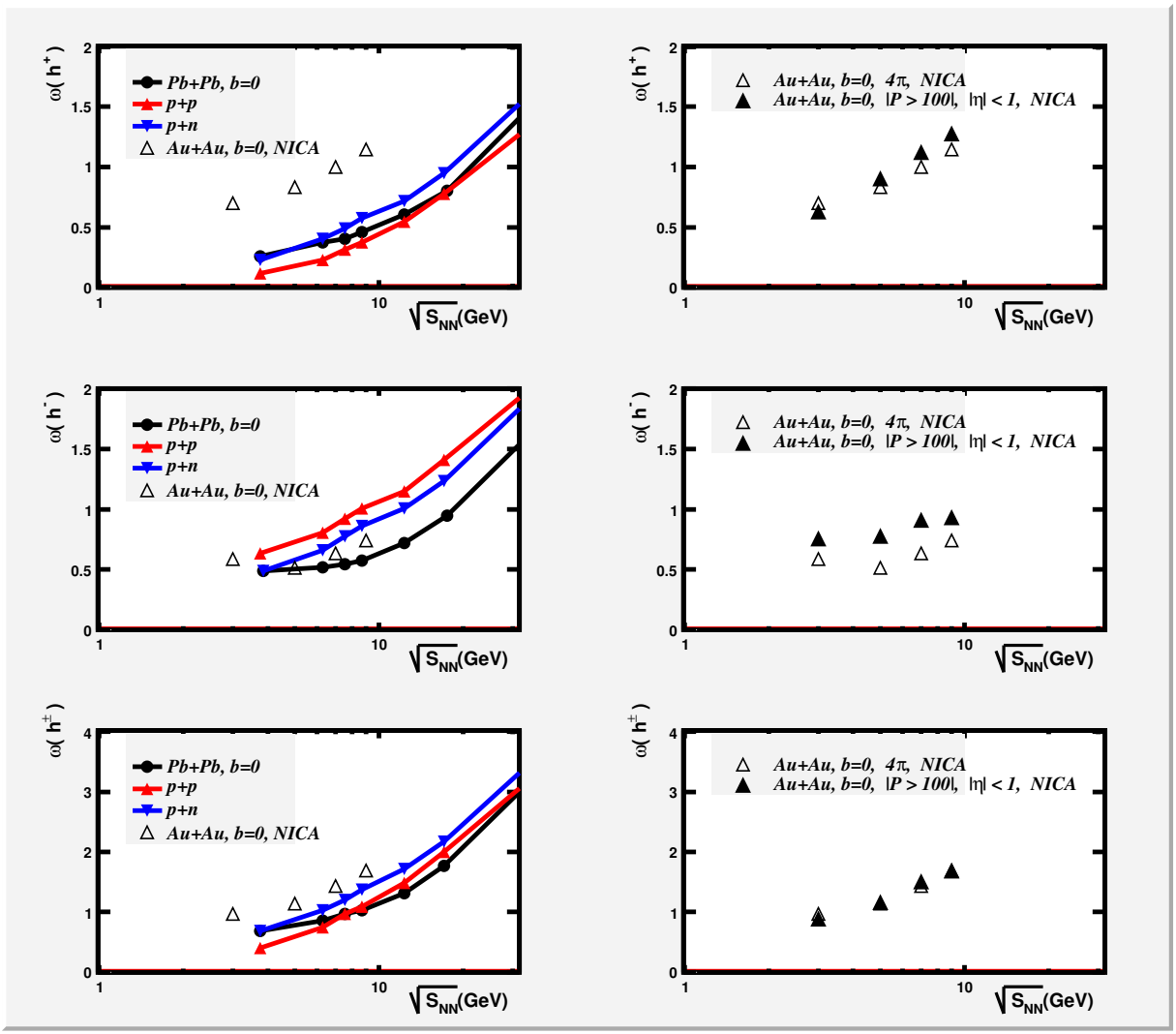

Fig. 1.6: Left column: scaled multiplicity variance data for pp, pn, and central Pb+Pb collisions compared with the UrQMD 4π predictions for the NICA energy range. Right column: UrQMD predictions for NICA for 4π and MPD geometrical acceptance.

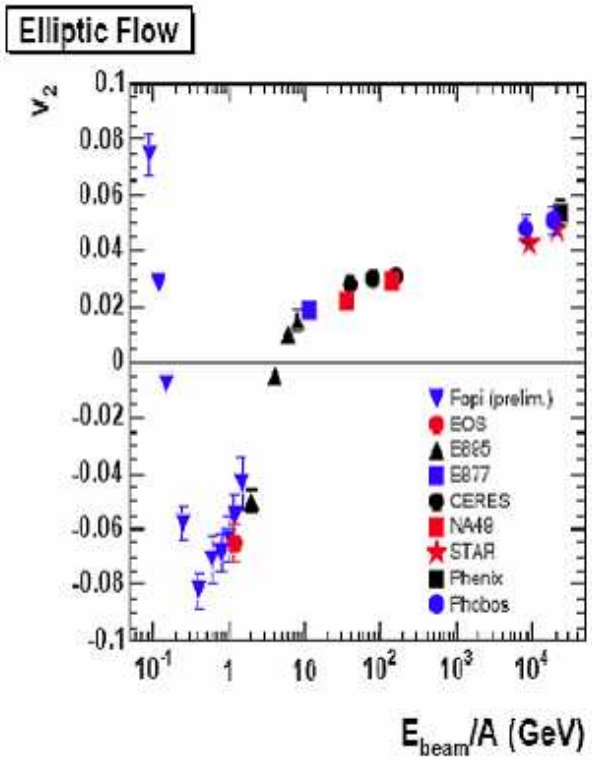

Fig. 1.7: Presently available data for the elliptic flow coefficient with integrated transverse momentum dependence.

Here q_i are the components of the pair momentum difference $\mathbf{q}$ in the i-th (out, side, longitudinal) directions. The factor λ is the incoherence parameter that ranges from 0 (complete coherence) to 1 (complete incoherence). The term R^2_{oL} is the so-called cross-term which vanishes at mid-rapidity for symmetric systems, and deviates from zero at large rapidities.

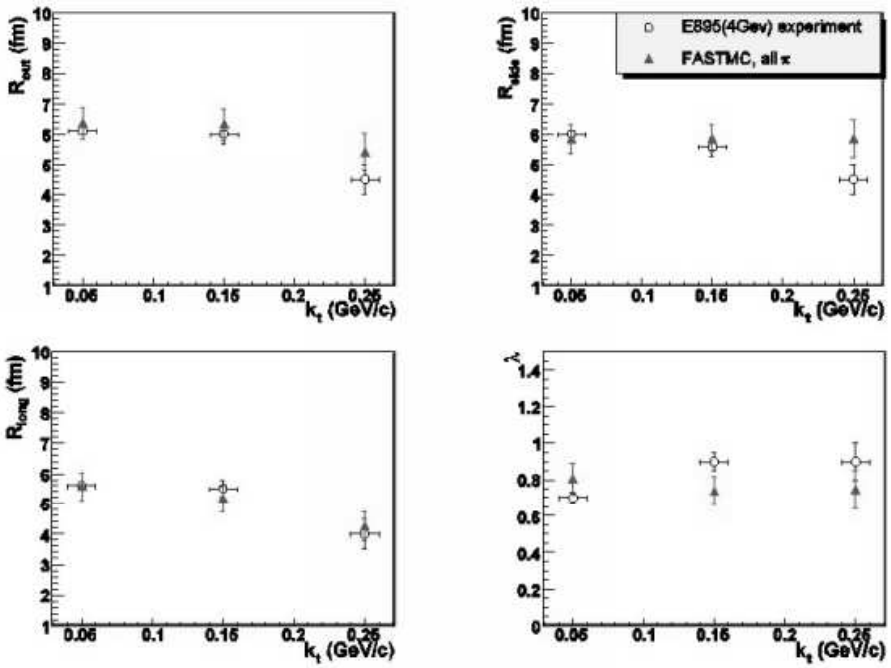

Fig. 1.8: Transverse momentum dependence of the identical pion–pion correlation radii and incoherence parameter for central $Au + Au$ collisions at $E_{beam} = 4$ GeV per nucleon calculated by the FASTMC code.

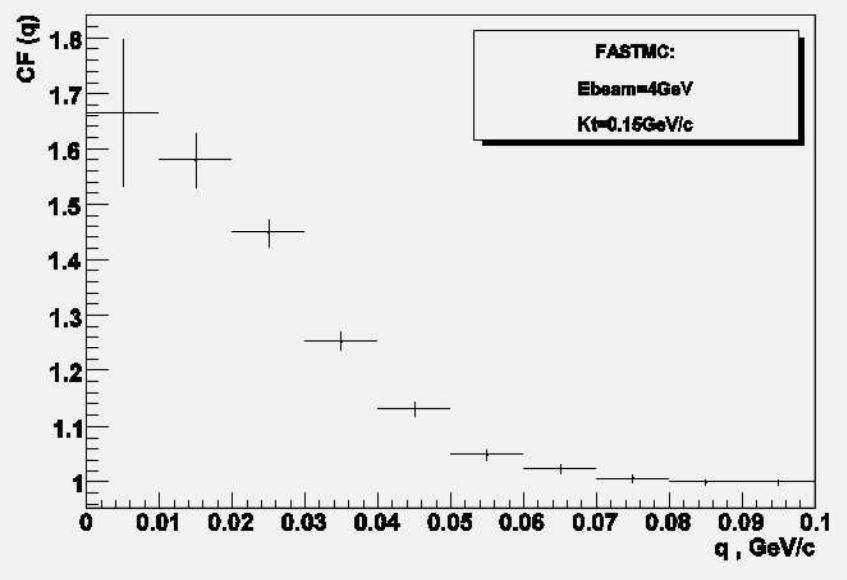

Fig. 1.9: Pair momentum difference dependence of the correlation function at the transverse momentum of pion pairs 0.15 GeV/c

Chapter 2

MPD Concept

2.1 General Design

The requirements to a detector at a heavy ion collider pose significant challenges for the general design, choice of subdetectors, and construction. The MPD will be located at one of the two interaction points of the NICA collider, and will be limited in space along the beam line by the collider magnetic optics. The detector should meet the following requirements:

- compatibility for the event rate up to 10 kHz with a multiplicity up to 1500 charged particles;
- efficient reconstruction of events, primarily in the pseudorapidity region of $\mid \eta \mid \leq 1.0$, with high angular and momentum resolution for charged particles (from 100 MeV to 2000 MeV);
- reliable identification of charged particles for those events and possibility to detect photons and π^0s;
- possibility to reconstruct tracks of charged particles and their momenta measurements in the region of $\mid \eta \mid \geq 1.0$;
- provision of reliable information for "centrality" definition, and the corresponding trigger logic.

The basic concept of the MPD is represented by a barrel and two endcaps located inside a magnetic field of a large solenoid. The barrel part is a shell-like set of various detector systems surrounding the interaction point and aimed to reconstruct and identify both charged and neutral particles in the region of $\mid \eta \mid \leq 1.0$. The two symmetric endcap parts are designed to reconstruct and to measure the momenta of charged particles with higher pseudorapidity. The basic design of the MPD is presented in Fig. 2.1.

The MPD general geometry is axially symmetrical taking into account the corresponding feature of events. The ion beams pass through the whole detector inside the beam pipe located along the z axis with the central interaction point at $z = 0$ in the centre of the detector. The interaction region covers an interval of $|z| \leq 25$ cm.

The barrel part consists of the trackers and particle identification system. The principal tracker is the time projection chamber (TPC) supplemented by the inner tracker (IT) inside the TPC. The outer tracker (OT) surrounding the TPC is an optional one. Both subdetectors (IT and OT) provide a good precision of charged track reconstruction and momentum measurement. The inner tracker is a silicon strip detector (as a baseline) representing a barrel of eight track position sensitive layers around the interaction region. A micromegas-based detector is considered as an optional one. The outer tracker consists of two double layers of straw tubes.

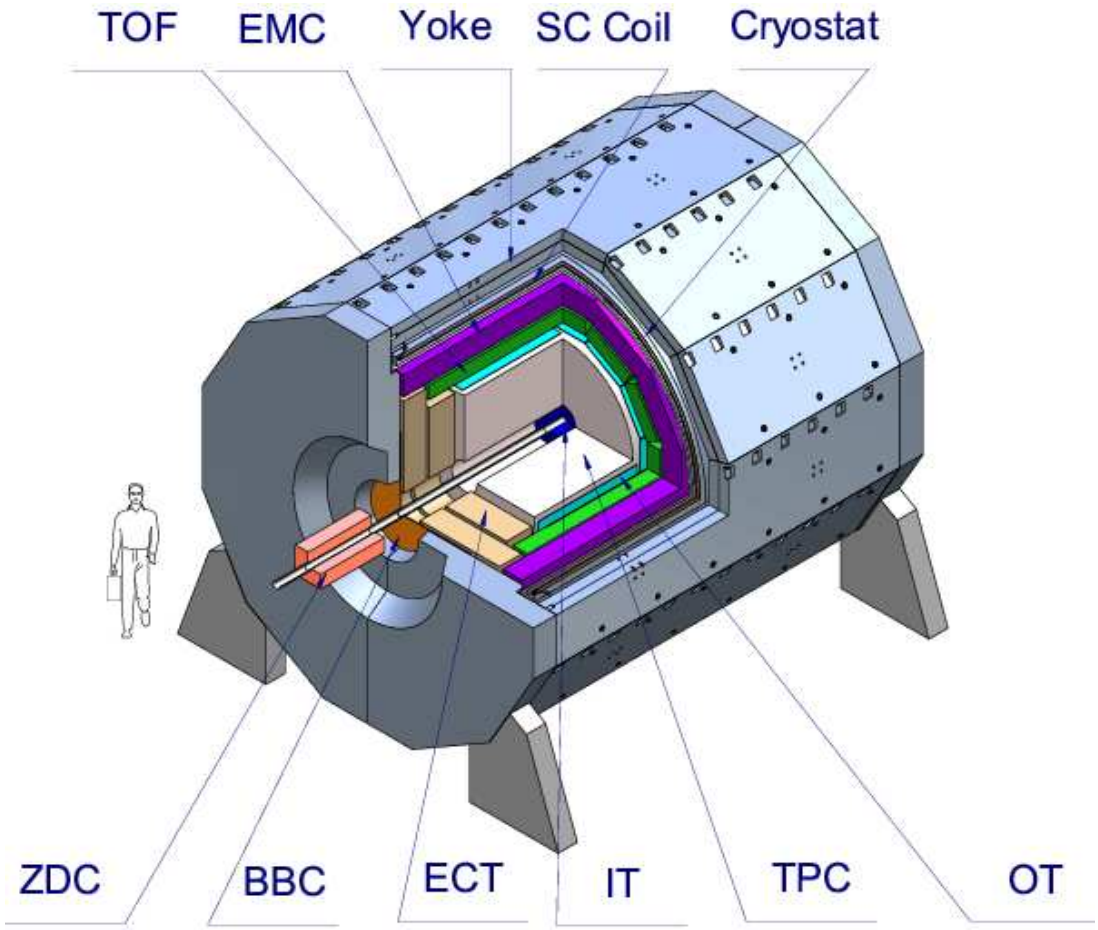

Fig. 2.1: General view of the MPD detector with end doors retracted for access to the inner detector components. The subsystems are indicated: superconductor solenoid (SC Coil) and magnet yoke, inner detector (IT), straw-tube tracker (ECT), time-projection chamber (TPC), straw tube outer tracker (OT), time-of-flight stop counters (TOF), electromagnetic calorimeter (EMC), beam-beam counter (BBC), and zero degree calorimeter (ZDC).

The time-of-flight (TOF) system is used for the charged track identification. It includes fast start detectors close to the z axis and Resistive Plate Chambers (RPC) surrounding the OT.

The electromagnetic calorimeter (EMC) is foreseen for gamma and electron/positron detection as well as for π^0 reconstruction. In addition to π^+ and π^- multiplicities, the yield of π^0 (or simply photons from π^0 decays) can be used as an independent observable in the search for high-density effects and phase transitions. The photon detector will also serve to measure the total energy flow. It reflects, to a large extent, the initial conditions which will occur in heavy-ion collisions at NICA.

The EMC is located in the barrel structure surrounding the barrel system of RPCs. Two possible options of the EMC are considered: the first is based on the crystals, and the other is a "shashlyk" type calorimeter.

Two ECTs are located on both sides of the TPC along the z axis. The current design includes wheel-like tracking detectors based on straw tubes. The ECT is designed in such a way as to provide more information (hit numbers) for tracks travelling at smaller radii

for which the TPC has poorer reconstruction ability. Thus a supplementary principle is exploited for tracking of the charged particles with high pseudorapidity ($\mid \eta \mid \geq 1.0$). It allows a precise definition of an azimuthal angle for charged tracks and momentum reconstruction with a sufficient precision.

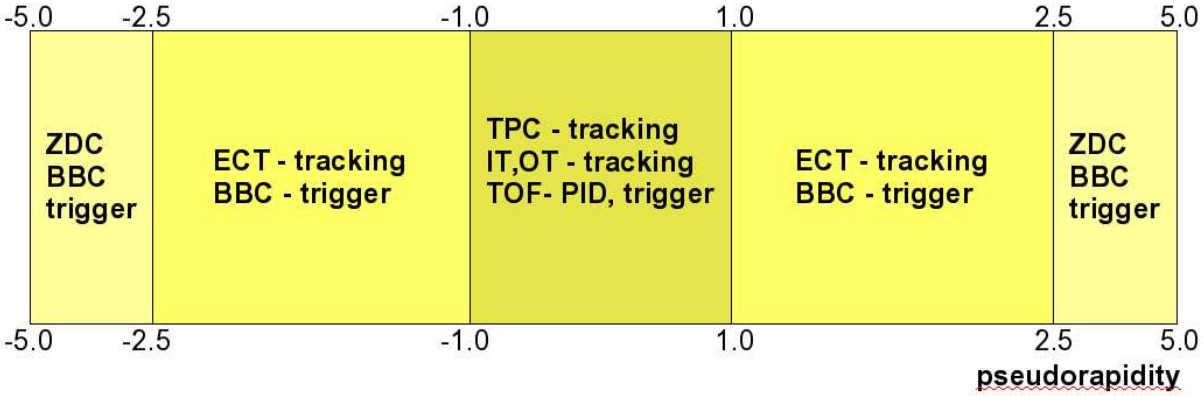

Fig. 2.2: MPD pseudorapidity coverage.

Particles emitted in very forward/backward directions are detected by the zero degree forward calorimeters (ZDC) which are used for centrality definition, event-by-event fluctuation measurements, and trigger signal formations.

Two beam-beam counter systems (BBC) located symmetrically along the z axis provide information for centrality determination, input for the L1 trigger, and additional information for the interaction point reconstruction.

The detector geometry is optimized taking into account some constrains and compromises. The length along the z axis is limited by a 800 cm gap between the collider optics. A radial scale is chosen as a compromise between the requirements of TOF and track reconstruction precision on one hand, and the requirements of a homogeneous magnetic field and limited cost of the magnet on the other hand. The radius of $\sim$ 200 cm inside the magnet defining a volume available for the subdetector allocation was chosen as an optimal one. This provides sufficient performance for track reconstruction and particle identification. The chosen scale allows construction a superconducting solenoidal magnet at a reasonable cost.

The overview of the MPD pseudorapidity coverage is shown in Fig. 2.2.

2.2 Magnet purposes

Fundamental detector performance and geometry considerations determine the design of both the solenoid and the flux return. The magnet should provide a field for the corresponding detectors to perform the following tasks:

- transversal momentum measurement with a high resolution for charged particles (from 100 MeV to 2000 MeV) in the pseudorapidity region of $|\eta| \lesssim 1.0$ by TPC;
- momentum measurement for charged particles in the region of $|\eta| \gtrsim 1.0$ by ECT.

For the transversal momentum measurements by TPC the magnet should have a solenoidal magnetic field with the homogeneity $Br/Bz < 10^{-4}$. The preferable momentum measurement technique in the region $|\eta| \gtrsim 1.0$ is the measurement with a field of

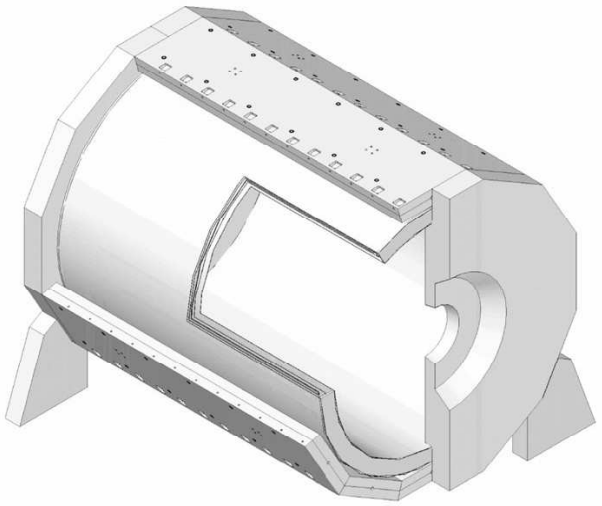

Fig. 2.3: Geometry of the MPD magnet system. Solenoid is shown within the barrel of the dodecahedral flux return. The endcaps are separable about the vertical centre to clear nearby fixed beamline components.

dipole magnet, but the geometry limits (defined by the collider optics) make this method unapplicable.

The option of non-uniform magnet field with a large radial component, formed by the return magnet flux (in the case of yoke design with a large endcap holes) will be studied in future.

Proposed here design is able to provide a field for the charged particles momentum measurements in the region of $|\eta| \gtrsim 1.0$ in homogeneous solenoidal field. The field is to be formed by a yoke with a small holes in endcaps. The size of the holes is defined by ZDC acceptance.

2.3 Magnet Coil and Flux Return

The MPD magnet is a 0.5 T superconducting solenoid design within a dodecahedral iron yoke for flux return and shaping of required homogeneity of a magnetic field, as shown in Fig. 2.3.

The design of the magnet and its operation factors satisfy the requirements identified during detector performance simulations, geometry studies, and cost evaluations. Development of the design should meet mounting and service requirements and magnet arrangements at the corresponding locations, possibilities and terms of its manufacture. Development and update of all these parameters and requirements will be continued until the technical design report is prepared. The magnet inner radius and length are optimized in conjunction with other detector subsystems. The anticipated inner radius is ≈ 200 cm with a cryostat length of 540 cm.

In general the magnet is similar to many operational detector magnets. In developing this design, physics criteria including central field magnitude and uniformity, size, and overall geometry were taken into account. The final specification of the magnet parameters satisfies the detector performance requirements and corresponds to acceptable operating and construction cost objectives.

2.4 Magnetic System

The magnet system consists of the solenoid, the flux return and supporting systems including cryogenics. Magnet requirements are derived from detector and accelerator performance objectives, engineering considerations, operational and facility requirements, and project constraints (cost, schedule, risk, and ES&H). Identification of these requirements and constraints began during the development of the Letter of Intent design, and will continue during the conceptual design.

2.4.1 Solenoid

The lower boundary of transversal momentum region of charged particles detected by the TOF (i.e. the radial position of TOF) depends on the magnetic field. For a field region $0.3 - 0.7\ T$ and TOF in radial position of 130 cm, boundary values of a transversal momentum detected by TOF will be 117–273 MeV/c, respectively. The magnetic spectrometer resolution is inversely proportional to the magnetic field B and the track transverse projection length squared ($\sim 1/(B \cdot l_p^2)$). Thus, the momentum resolution can be improved either by selecting a larger field or using a smaller field but with a bigger size. The comparative estimate of these two alternatives is necessary.

The interior warm bore of the solenoid varies over the range of 150–200 cm, and is determined by the composition, sizes, and the radial positions of detectors and technological gaps between them with noncylindrical shape of detectors taken into account($\approx 1/\cos(15^\circ)$). The minimum size is attained at a position and TOF size of 130 and 20 cm, gaps of 0.50 cm, and removal of the electromagnetic calorimeter from the detector. The maximum size is attained at the TPC external radius of 110 cm, and by using an additional straw tracker and an electromagnetic calorimeter. Supporting devices for detectors can increase the solenoid size as well.

The solenoid length is defined by sizes of detectors, pseudorapidity range of particles which should be detected in the barrel part of the detector, and the required high homogeneity of magnetic field in the TPC region: $B_r/B_z \leq 0.001$.

The length of the cryostat varies with bore radius over the range of 400–550 cm. The design of the solenoid coil should ensure the required homogeneity of a field.

2.4.2 Yoke

The magnet yoke serves to confine the inverse magnetic flux, and participates in shaping of the magnetic field with the required homogeneity. Homogeneity of a field very strongly depends on the inlet opening size. Thus this size should be minimized, which is a passive method of homogeneity improvement. Homogeneity of a field is also rather sensitive to the relative position of face devices of the yoke and the solenoid coil, especially in the region of their closeness, which demands optimization of the yoke shape.

The thickness of the yoke is dictated by steel type, and should match the demands on the admissible leakage field in peakly admissible operating modes of a magnet (e.g. for safety reasons). Predesigns show that the thickness of the yoke should not be less than 0.3 m. The size of the hole in the endcap parts of the yoke influences the value of the leakage field in the direction of collider elements. The construction should be optimized by taking into account mounting and arrangement requirements, as well as the delivery requirements.

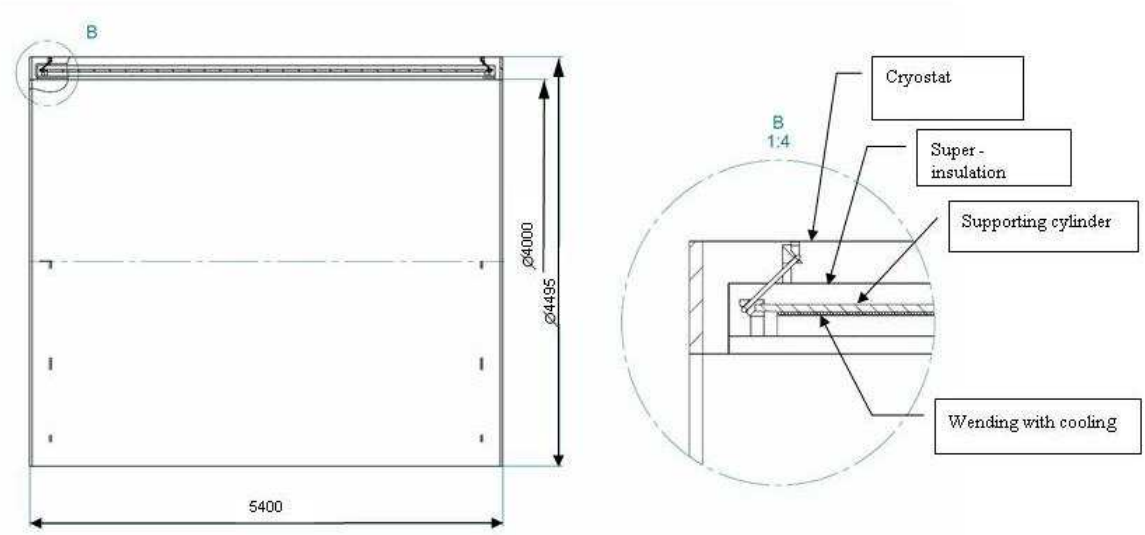

Fig. 2.4: Conceptual design of the solenoid (sizes in Table 2.1).

2.4.3 Magnet design

The magnet consists of the superconducting solenoid and the iron yoke. The general design of the magnet and solenoid follows the designs of analogous existing and designed magnets (for ILC); differences consist in design features of the superconducting solenoid. The used technology is highly developed at the LHE, and well proved in Nuclotron magnets of the tubular superconducting cable cooled by two-phase helium. It is proposed to use a hollow composite superconducting cable for the winding of MPD solenoid. Such a cable contains a cooling tube wrapped by 18 isolated SC wires. Good thermal contact between the wires and the tube is guaranteed by the bandage thread pressure. The cable for the solenoid could be similar to the cable of Nuclotron magnets, it can be produced on the cabling machine available in the Laboratory after modernization of equipment. Use of such a cable makes it possible to manufacture the winding and the support cylinder of MPD solenoid at JINR facilities without any involvement of industrial contractors. The single-layer winding of 4.2 m in diameter will be made of 10 parts 0.5 m length each. In our case the solenoid supporting cylinder is not a bridge for heat transfer. It could be made by wrapping around of a glass-fiber cloth impregnated with epoxy resin. The choice of this modified Nuclotron-type technology for a construction of MPD solenoid will essentially decrease the expenses.

The magnet yoke consists of the central dodecahedral part and two-face devices (see Fig. 2.4 and Table 2.1).

2.4.4 Field homogeneity

As mentioned above, homogeneity of the field depends on the geometry of face elements of the yoke and primarily on the size of inlet openings and design of the region of the yoke, face elements of devices, and solenoid closeness. Homogeneity can be refined by inducting inhomogeneities in coil. As the solenoid is a system of sequentially joint sections, for inhomogeneity making there is a possibility of variation of a number of turns in a section (diminishing from a maximum) and a dilatational size of a section (incrementing a positive

Table 2.1: The main construction parameters of the MPD magnet system.

item	units	characteristics
Support cylinder		
Material		Reinforced fiber glass (or Al alloy)
Winding		
Maximum operational central magnetic field, B0	T	1.0
Length	m	5.0
Mean radius	m	2.09
Number of layers		1
Number of sections		10
Number of cable turns		532
Number of wire turns		18 x 532
Operational current	A	415.5
Inductance	H	316.1
Stored energy, E	MJ	27.3
E / (M1+ M2) - ratio	kJ/kg	16.6
E /(M1+ M2+ M3) - ratio	kJ/kg	9.83
Total cold mass at 4.6 K	kg	7850
Cooling		
Method		forced two-phase He flow
Operating temperature	K	4.6
Load at operational condition	W	≤ 37
Load at energy input	W	≤ 73
He mass flow rate	kg/s	$2.73 \cdot 10^{-}3$
Number of parallel cooling channels		10
Allowable pressure in channel	MPa	10
Cool down time	hour	≥ 50
He consumption for current lead		absent
Cryostat		
Length	cm	540
Inner SS vacuum shell diameter	cm	400
Outer SS vacuum shell diameter	cm	440

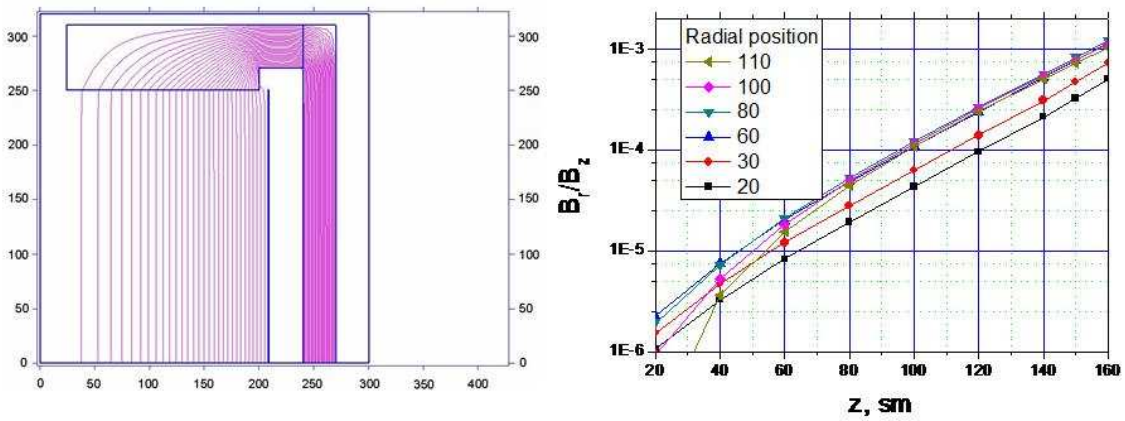

Fig. 2.5: a) Flux lines in the magnet (an axis of bundle z is vertical). b) Yhe ratio B_r/B_z vs z along the lines parallel the the z axis at various distances from the z axis.

allowance between turns). Predesigns show that at an inlet opening of the back of the yoke 500 mm diameter, the ratio B_r/B_z is less than 0.001 over the whole in the TPC volume (Fig. 2.5).

At larger sizes of an inlet opening it is practically sufficient to select sizes and density of winding of extreme sections and also their dilatational position relative to face parts of the yoke.

Chapter 3

MPD Barrel Design

3.1 TPC for the MPD Central Tracking

The TPC is an ideal tracker working well in a high multiplicity environment. It is the main tracking detector of the MPD central barrel, and together with the IT and TOF it should provide charged particle momentum measurement, particle identification and vertex determination, two-track separation, and dE/dx resolution. All these objectives are to be reached at the design luminosity of $10^{27}\ cm^{-2}s^{-1}$ for $Au + Au$ collisions at the NICA collider which corresponds to an interaction rate of about 10 kHz. The produced charged particle multiplicities are limited by ~ 1500.

Special attention should be paid to the following characteristics and features of the TPC:

- gas mixture and gas purity;
- drift velocity stability;
- uniformity of electrical and magnetic fields;
- space charge effect;
- calibration;
- space resolution;
- rate capability;
- occupancy;
- number and size of PADs;
- FE and readout electronics.

There is intention to keep R&D and prototyping works as minimal as possible to save the cost and time. So during the design and construction stage there is a plan to use the optimal solutions accepted for the STAR (version for upgrade) [26, 27] and ALICE [28] TPCs.

3.1.1 TPC tasks

The TPC should perform the following tasks in the transversal momentum region 0.1 GeV/$c < p_t <$ 3 GeV/c for $|\eta| \lesssim 1.0$:

- track finding;

- momentum measurement;
- particle identification.

3.1.2 Main requirements

- tracking efficiency $> 90\%$;
- momentum resolution $< 2.5\%$;
- dE/dx resolution $\approx 6\%$;
- two-track resolution < 5 MeV/c ($\approx$ 1cm);
- rate capability ≈ 10 kHz.

It is known from the NA49 experiment that particle densities of $(0.1 - 0.2)\ cm^{-2}$ can be safely handled for track reconstruction and even for dE/dx measurement. Two track separation and momentum resolution have to be kept to the limits imposed by multiple scattering and diffusion in order to measure two particle correlation function down to about 5 MeV/c (1 cm).

The TPC will have a cylindrical shape (see Fig. 3.1) of the following sizes, defining the acceptance in the region $|\eta| \lesssim 1.0$:

- outer radius: 110 cm;
- inner radius: 20 cm;
- drift length: 150 cm;
- total length: 300 cm.

Charged particles crossing the TPC create electrons by ionization. The electrons drift in the electric field to the Readout Chambers. The amplification factor of these chambers is $\approx 10^4$. The crucial parameters determining two track resolution are the diffusion constants and total drift length.

The mechanical structure is composed of outer vessels, end flanges, and inner vessels. Materials are carbon fiber composite and honeycomb (NOMEX).

3.1.3 Readout Chambers

The wire Readout Chamber sectors (30° in azimuth) are mounted on each side of the cylinder, on the endcap wheels. The TPC has in total 24 chambers (in both sides). The overall area to be instrumented is ≈ 8.0 m^2. The chambers will be conventional multiwire proportional chambers with cathode pad readout. To keep the occupancy as low as possible and ensure the required dE/dx and position resolution, there will be about 80,000 readout pads with two different sizes of 0.5 cm^2 at the inner part, and 1.0 cm^2 at the outer part. There is a plan to construct the gas system similar to the one of the ALICE TPC but with ≈ 7 times smaller capacity.

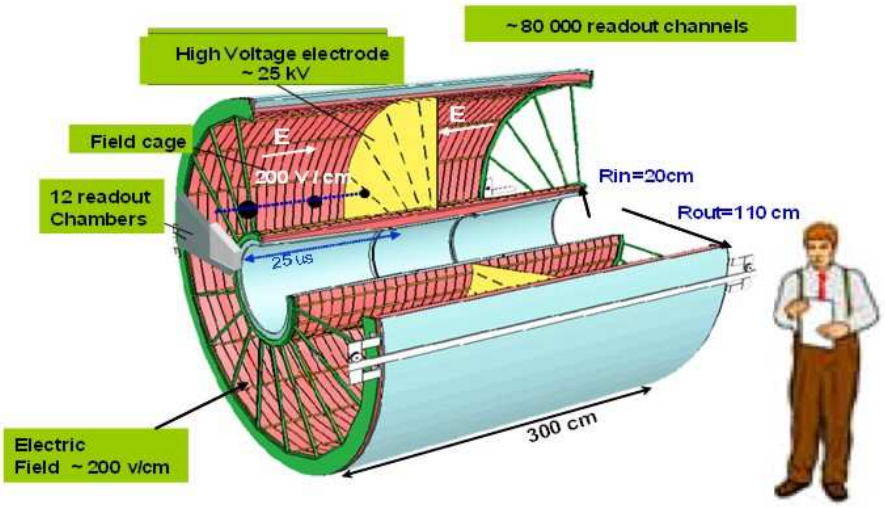

Fig. 3.1: Schematic view of the TPC.

3.1.4 Electronics

About 80,000 channels of Front-End Electronics for the TPC have to be highly integrated. Three basic units will be implemented for each channel: a low-impedance charge-sensitive preamplifier/shaper, a commercial 10-bit analog-to-digital converter (ADC) with up to 10 MHz frequency range, and an ASIC with a digital filter for tail cancellation, with base-line subtraction and zero-suppression circuitry, and a multiple event buffer, all to be implemented in CMOS technology. There is an intention to use the same Front End electronics as used for the ALICE TPC.

3.1.5 Two-track resolution

Two-track resolution has to be such that HBT measurements with a resolution in relative momentum of a few ≈ 5 MeV/c can be performed. This may require running at higher magnetic fields. Two-track resolution of ≈ 1 cm is expected.

3.1.6 Resolution on dE/dx

For hadron identification a dE/dx resolution of $\approx 8\%$ is desirable, following the experience of the NA35 experiment. For the MPD TPC a resolution on dE/dx of $\approx 6\%$ is expected (following Fig. 3.2).

It is also expected to get for the TPC alone:

- p/K separation in the momentum region of ≈ 0.7 GeV/c;
- $(p + K)/p$ separation in the momentum region of ≈ 1.2 GeV/c.

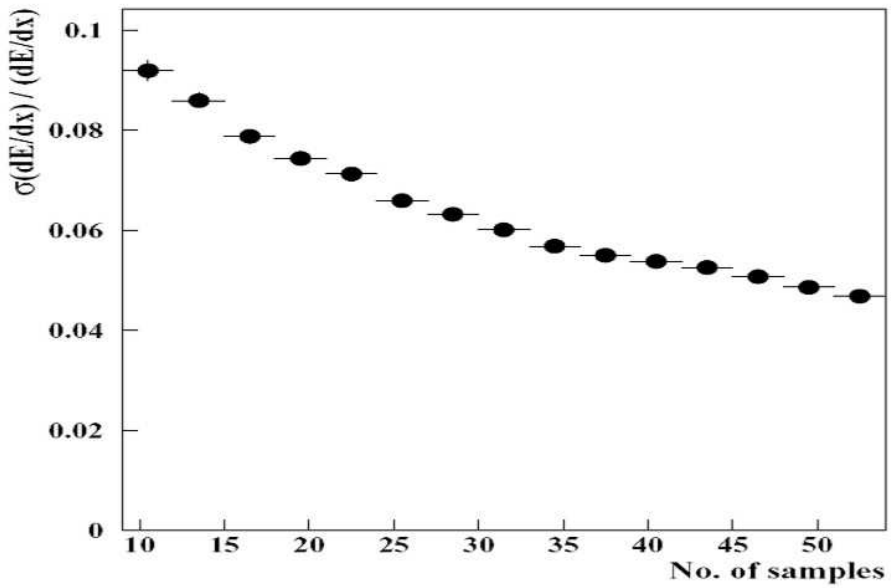

Fig. 3.2: dE/dx resolution as a function of the number of samples in the NA35 TPC. Sample length is 4 cm, the gas is Ar/CH_4 (91/9).

3.1.7 Track density

Simulation results of track density along the z axis of the TPC for central $Au + Au$ collisions are presented in Fig. 3.3.

3.1.8 Test and calibration

For test and calibration it is foreseen to use the 266 nm wavelength Nd-YAG laser. This device will permit the following:

- testing the electronics;
- alignment of the readout chambers;
- monitoring the variations of drift velocity (including also the influence of space charge effect).

3.1.9 The list of main parameters of the TPC

- outer radius: 110 cm;
- inner radius: 20 cm;
- drift length: 150 cm;
- total gas volume: ≈ 12 m^3;
- total number of readout chambers: 24 (12 for each side);
- total number of pads: $\approx 80,000$;

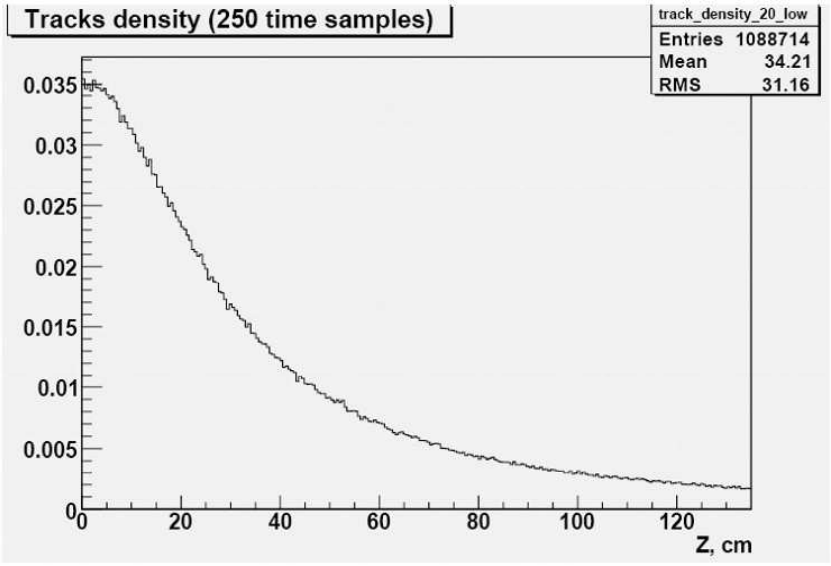

Fig. 3.3: Track density along the z axis of the TPC for central Au + Au collision (simulation results).

- number of pads to be read out after zero suppression: $< 10\%$;
- gas mixtures: Ar/CH_4 (90/10);
- gas amplification factor: $\approx 10^4$;
- drift time: $\approx 25 - 30$ μs;
- multiplicity: < 1500;
- occupancy: $< 10\%$;
- spatial resolution: $\delta z \approx 2.0$ mm, $\delta x \approx 0.6$ mm, $\delta y \approx 1.0$ mm;
- two-track resolution: ≈ 1 cm;
- dE/dx resolution: $\approx 6\%$ (75 samples $\times$ 2 cm);
- maximum rate: ≈ 10 kHz (at luminosity of 10^{27} $cm^{-2}s^{-1}$).
- uniformity of transverse magnetic field is $B_r/B_z < 6 \times 10^{-4}$.

3.2 Silicon Tracking System as an Inner Tracker of the MPD

The Inner Tracker (IT) is a detector system situated in the very heart of the MPD allowing sensors to work at the closest possible distance to the beam interaction volume.

In general, the IT major task is to improve the track finding of the TPC especially for events with high multiplicity up to ≈ 1500. Being more specific, the IT tasks are as follows:

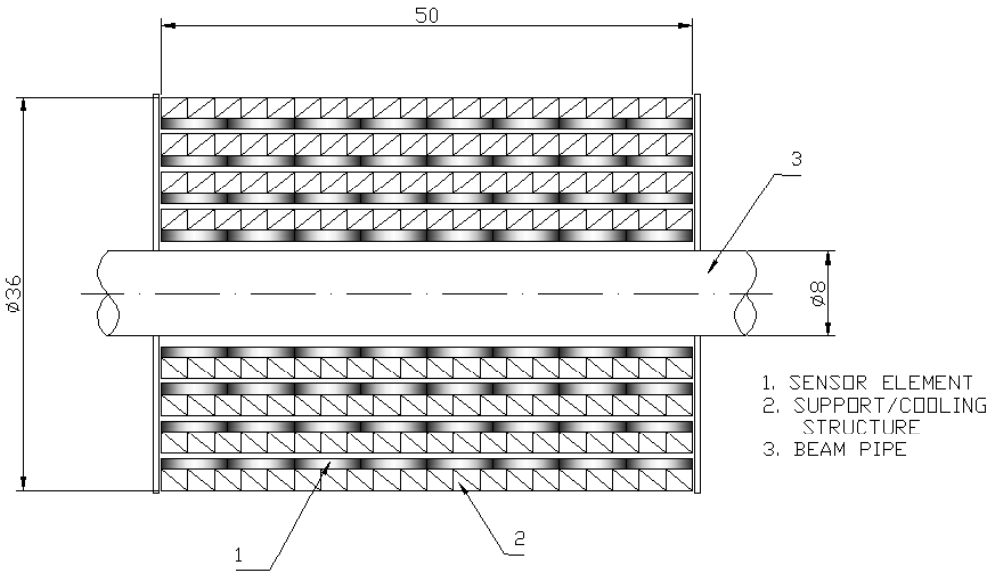

Fig. 3.4: Longitudinal view of the conceptual layout of the STS.

- to reconstruct events with multiplicities up to 1500 tracks;
- to provide track extrapolation to the barrel detector;
- to measure ionization and perform identification of low energy secondary particles (protons with energy $\geq$ 200 MeV, deuterons with energy $\geq$ 300 MeV);
- to reconstruct decay vertices of the secondary particles before they reach an active volume of the TPC.

A proposal to build a conventional Silicon Tracking System (STS) exploiting a widely used technique of particle tracking with Silicon Strip Detectors (SSD) acting as the MPD IT is briefly described below.

3.2.1 Conceptual design of the STS version of IT

The proposal was greatly inspired by the technology developments of the ALICE collaboration in building up the ALICE IT. The STS layout is schematically depicted in Figs. 3.4 and 3.5. Similarly to the other silicon trackers worldwide, it has a barrel-like structure with multiple sensor nodes forming the surfaces of eight cylindrical sensitive layers located at the closest distances from the interaction region of the two colliding beams.

The STS sensitive layers are located in the range of radii within 4 cm and 16 cm from the interaction point. This covers the rapidity range $\mid \eta \mid \leq 1$ for all vertices at the geometric centre of the STS. The outer radius is determined by dimension of the TPC entrance window to allow TPC and STS track segments to match. The inner radius of the STS has minimal technological clearance between the IT and the beam pipe.

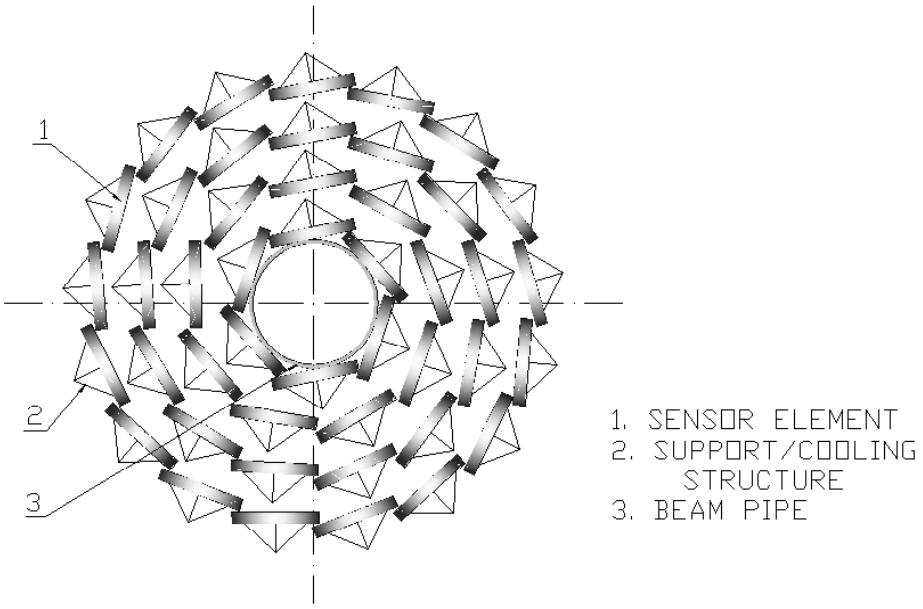

Fig. 3.5: Transverse view of the conceptual layout of the STS.

The above-mentioned requirement to detect low momentum protons and fragments makes it necessary to develop a system with a minimal possible material budget. Here the technological developments of the ALICE collaboration are to be exploited at full. All the layer support and cooling parts are to be manufactured of ultra-light carbon fiber composite materials [29] with all bonding of electrical contacts made with the help of modern Tape Automated Bonding (TAB) technology [30] suitable for the usage of ultra light cables manufactured of aluminum polyimide [31].

The average thickness of the layer including the cooling and electrical services is around 1% X_0 with another 1% X_0 needed for the electrical shielding of the sensors [32]. The total material budget of the STS for particles scattered at 90° is 7% or 14% of X_0 depending on the sensor type used in the setup to be described below.

3.2.2 SSD ladder as a basic element of the STS

The basic element of the STS is the so called SSD ladder shown schematically in Fig. 3.6. The basic components of the ladder are the ultra-light carbon fiber support and cooling structure holding the sensor elements with front-end electronics which are controlled by the back-end control boards – Back Cap controllers. Sensors, front-end electronics, and the Back Cap controllers are connected via ultra-light multi-strip flat cables [31].

3.2.3 Sensor description

The Silicon Strip Detectors (SSD) are used as basic sensor elements for STS. Both single and double sided versions of SSDs are now being considered with final decision to be taken after the R&D stage of the project is accomplished by the end of 2009. This document considers a less expensive version of the STS based on the technology of Single-sided

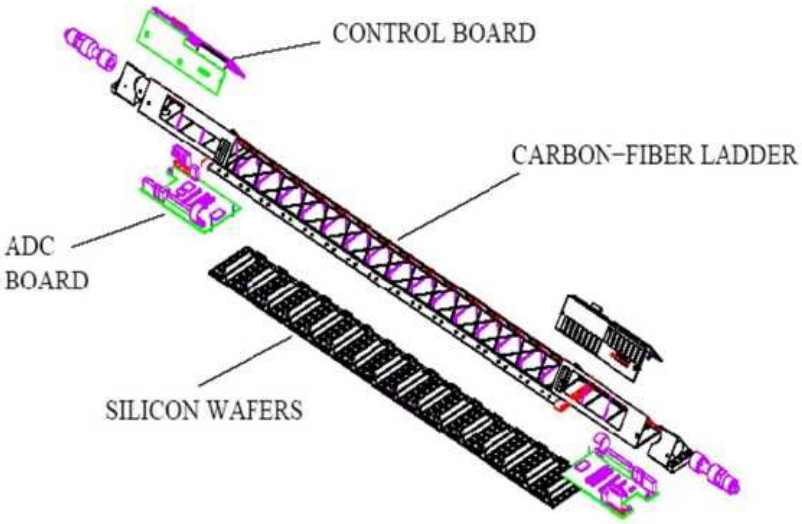

Fig. 3.6: The components the SSD ladder of the STS.

Silicon Strip Detectors (SSSDs) available for commercial production in Russia. Here the SSSDs are grouped in telescope-like modules of two SSSDs shown schematically in Figs. 3.4 and 3.5 as small shaded boxes mounted onto the carbon fibre support ladder. Two detectors of a module form a network of strips with 100 mrad stereo angle between the strips of each successive sensor. This angle provides an acceptable rate of ambiguities in track reconstruction while keeping the number of readout channels as small as possible and providing a resolution along the beam axis of around 0.5 mm. Two types of detectors are foreseen with the only difference in the tilting angle of the strips, i. e. 30 mrad and 70 mrad. Changing the order of sensors of different types in successive layers of the STS results in groups of sensors with four different strip orientations with respect to the beam. This considerably reduces the number of ambiguities in track reconstruction, because the ambiguities in different layers are basically not repeated.

The strip orientations are all nearly parallel to the direction of the magnetic field, so that the best position resolution is achieved in the particle trajectory bending direction. The 230 μm strip pitch and the 60 mm strip length define the system granularity. With this pitch the occupancy is less than 10% in the inner layer of the IT. All the sensors are 300 μm thick to provide good signal-to-noise ratio. The read-out system is an analog with a dynamic range not less than 12 MIP to supply dE/dx values for identification of protons and deuterons.

3.2.4 Support/cooling system

Multiple scattering in the silicon detector and its supporting/cooling structures set a fundamental limitation on its spatial resolution. This limiting factor is determined by the material budget, i. e. by the equivalent thickness of the detector in terms of radiation length.

The complete detector system consists of various elements such as front-end electronics, sensors, and hybrids holding the silicon elements mounted on a mechanical support with a cooling system. In the project the authors propose to investigate the techniques allowing the detector layers to be made as thin as possible, while remaining compatible with

realistic requirements on mechanical stability and handling procedures. The project will include, in particular, an in-depth study to reach the following self-contradicting goals:

- minimum of material budget in the area of track registration;
- "transparency" for incident particles using the materials with minimum atomic weight;
- stiffness of the support structure for silicon detectors, its high thermal and mechanical stability during the $\approx$ 10-year period of the running expertise.

The design of the ALICE IT mechanics [29] could be used to improve mechanical properties of the support/cooling structure of the MPD IT.

The classical three-edged space frame developed in Russia for the ALICE IT could serve as a basic element of support for the MPD IT after a minor upgrade. As compared with the other possible solutions, it is characterized by the largest stiffness-to-mass ratio. Besides, each lateral side of a frame free of SSD could house the other elements of the front-end electronics, cables, etc. The exact dimensions of the space frame for the STS will be optimized with the help of final element method (the ANSIS software). At present it is possible to manufacture the frame with $350-400$ μm elements. The thickness of STS frames will be reduced to $200-250$ μm after a certain R&D work aiming at improvement of the technology is accomplished. Anyway, manufacturing the space frames with effective specific linear density of 15 g/m seems feasible.

The ladders with SSDs are to be fixed horizontally and form a framework of the detector cylindrical layers, as depicted in Figs. 3.4 and 3.5.

The leakage current of sensors and the front-end electronics is high enough and dissipates approximately up to 1 kW. Therefore a compact cooling system is required to take the heat away. Such a cooling system for the STS is a subject of R&D. Cooling is an important issue since the quality of the TPC measurements is greatly affected by temperature instability.

The requirements to radiation hardness of the sensors imposed usually by the necessity of cooling them to low temperatures do not seem to be too high for the STS since the expected radiation levels are modest. However various cooling systems could be offered for the STS depending on the front-end electronics heat production (the latter is not yet clear):

- evaporative cooling system for heat loads $\approx$ 2 W/cm^2;
- contact method developed in Russia [29] for heat loads $\approx$ 0.5 W/cm^2;
- air cooling system for lower heat loads due to its simplicity [29].

3.2.5 Front-end electronics and cabling

Due to a large number of channels the price of the front-end electronics, though of a low-price type, causes most of the cost of any STS. That is why the decision on the exact type of the front-end electronics of the STS for the MPD is a subject mostly driven by the economical and organizational reasons. Due to an exceeding cost of the STS task it is not planned to develop any custom-built application-specific integrated circuit (ASIC),

but rather to exploit the existing ASIC already developed by other collaborations which have been working intensively in this field for the last 15 years.

The first candidate to be considered is the HAL25 chip developed for the ALICE IT in France [33, 34]. This is the 128-channel front-end chip which amplifies and shapes the signals from the sensor strips and contains a sample-hold circuit to store the analogue information after a trigger. The analogue-samples can be read-out serially at speeds up to 10^7 samples per second. The peaking time of the shaping circuit is adjustable between 1.4 and 2.2 μs. All parameters of the chip are controlled via a standard interface. The chip is 11 mm long, 3.5 mm wide, and 150 μm thick. It dissipates 380 mW.

One side of each sensor is connected to a hybrid with three HAL25 readout chips. The hybrids are mounted on the carbon-fiber heat bridges of the cooling system and are connected to the read-out Back Cap controllers situated at the back-ends of the supporting carbon-fiber space frames. Connections on the hybrid and connections between the front-end chips and the sensor are made by using ultra-thin micro-cables consisting of aluminum conductors on a polyimide carrier [31].

3.2.6 Organization and planning of work

The realization of the STS requires experts in different fields to join their efforts in feasibility studies, development of detectors, front-end electronics, and data acquisition systems. In order to make efficient the use of expertise, infrastructures, and resources, it is decided to pursue this project as a joint research and development activity of several Institutes in Russia and Ukraine. As a first step, the teams are establishing a consortium to design and manufacture prototype tracking detector modules based on silicon micro-strip sensors for the CBM project at the FAIR and MPD setup at the NICA. The consortium will comprise groups from the following institutions:

- Joint Institute for Nuclear Research (JINR), Dubna, Russia;
- Skobeltsyn Institute of Nuclear Physics of the Moscow State University (SINP-MSU), Moscow, Russia;
- V.G. Khlopin Radium Institute (KRI), St. Petersburg, Russia;
- State University of SPb, (SPbSU), St. Petersburg;
- Institute of Theoretical Physics (BITP), Kiev, Ukraine;
- State Enterprise Scientific Research Technological Institute of Instrument Engineering (SESRTIIE), Kharkov, Ukraine;
- Gesellschaft fur Schwerionenforschung (GSI), Darmstadt, Germany.

The Consortium is an open organization and any other institute can join provided it shares the goals of the Consortium and the member institutes have no objections. The distribution of tasks among the members of Consortium is as follows:

- JINR: Assembly of prototype ladder-sections for the STS and tests of the prototype modules with radioactive sources and relativistic particle beams;

- SINP-MSU: Design of double-sided silicon microstrip sensors, according to the requirements of the STS, and development of the technology for the production of the sensors;
- KRI: Development and production of mechanical and cooling systems for the STS in a dedicated workshop. Radiation tests of the silicon sensors at the KRI cyclotron neutron source which is to be developed for this purpose;
- SPbSU: Participation in the design and production of mechanical and cooling systems of the STS;
- SESRTIIE: Design and production of micro-cables for the STS. Development of tools and methods for assembling the ladder-section;
- BITP: simulations for the optimization of the ladder;
- GSI: Development of track reconstruction algorithms, optimization of the detector layout.

3.2.7 General features of the system

The main characteristics of the proposed STS are summarized in Table 3.1.

Table 3.1: IT characteristics.

Total area, m^2	2.6
Number of modules	720
Detector sensitive area, mm^2	35.4
Read-out channels per module	512
Radial position of the inner layer, cm	4.5
Radial position of the outer layer, %	16.0
Occupancy of the inner layer, %	10
Occupancy of the outer layer, %	1
Spatial precision r_ϕ, μm	200
Spatial precision z, μm	500
Two track resolution:	
r_ϕ, μm	300
z, μm	600

The estimated cost for building the STS for the inner tracking of particles in the MPD including 2 year R&D phase of the project is around 3600 k$.

3.3 Micromegas Gaseous Chambers as an Inner Tracker of the MPD (optional)

3.3.1 Conceptional design of the Micromegas Tracking System (MTS) version of IT

Recent developments of micromegas gaseous chambers (MMGCs) [35] have proven that the use of this novel technique is most promising for the construction of the IT provided additional R&D being undertaken with regard to the NICA-MPD project.

The requirements to tracking sensors located at small radii near the beam pipe up to the radial distance of about 20 cm are very strict. Indeed, the nominal $Au + Au$ ion interaction rate of 6 kHz leads to particle fluxes up to 10^3 cm^{-2}s^{-1} at a radial distance of R=10 cm from the beam. The flux drops to below 300 cm^{-2}s^{-1} for the radial distances above R=20 cm. It seems that the usage of MMGCs for tracking charged particles has a good chance to be feasible within the next few years up to average fluxes of 10^8 cm^{-2}s^{-1}. The MMGCs have to be radiation hard and not to show significant aging effects up to integrated doses of 0.1 Mrad/year. Good results have been reached in laboratory tests obtaining spatial resolution < 70 μm [35, 36]. We plan to use these techniques for development of the IT establishing collaboration with other institutes worldwide.

3.3.2 Sensor element development: chamber geometry and gas

The MMGCs sizes are presently limited by the abilities of industry to produce the hole pattern on 5 μm thick cooper foil with needed accuracy. Chambers with sensitive area up to 50×50 cm^2 can be presently built at CERN. For the MTS we need to develope chambers with maximum sensitive area of 50×14 cm^2.

The most serious requirements for the MMGCs for the IT application apart from rate and radiation hardness are as follows.

- Strip occupancy: a chamber is to be developed for the IT with 80 mm wide sensitive area with 196 strips and a pitch of the anode of only 400 μm. The expected strip occupancy of the chamber is less than 6%, and the hit resolution is ≈ 150 μm for the length of the strips of about 25 cm.

- Gap width: in the case of absence of any limitations on the drift time, a gap width of 3 mm seems to be feasible with a drift velocity ≥ 30 μm/ns, small Lorentz angle for $B = 0.5$ T, $E_{drift} \geq 2$ kV/cm, and a high gas gain. Primary ionization produces about 50 electrons in a 3 mm gap. Gas amplification of $5 \cdot 10^3$ in a 50 μm gap can be safely reached, leading to an average signal of 250,000 electrons. Aging effects are very critical for MMGCs and require a clean gas system.

- Material thickness: fiberglass FR4 with a thickness of 1.0 mm corresponding to $0.5\%X_0$ for NEMA G10 plate is to be used as an MMGC anode. Four MMGC double layers of chamber sensitive volumes are to be positioned on the radii starting from R=10 cm with secondary particles, subjects for tracking, passing through them. Thus, the anodes alone result in a sensor thickness of $4\%X_0$. In addition, there are several copper layers of 160 μm thickness totally contributing with an additional $1.15\%X_0$.

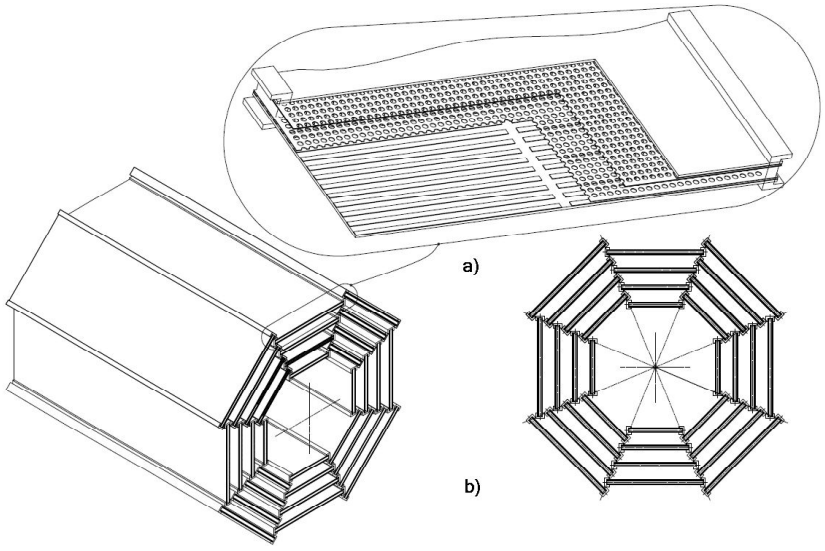

Fig. 3.7: a) Conceptual design of a double layer MMGC; b) Layout of proposed MMGC for the MTS.

In order to make the MTS as light as possible, a research is being undertaken to study the properties of double layer chambers with two strip layers and a common cathode. The final choice of technical solutions derived from results of the study will be made after additional critical evaluation of material thickness and the requirements for clean gas conditions.

3.3.3 The MMGC double layer chamber as an MTS basic sensitive module

A sketch of a double layer of MMGCs with two strip orientations is shown in Fig. 3.7.

The chamber is composed of two 1.0 mm thick Printed Circuit Boards bearing anode strips and a mesh stretched on a frame and mounted above the strip planes. The copper mesh is 5 μm thick and has circular holes of 35 μm in diameter placed with 60 μm pitch. The 50 μm gaps are maintained between the mesh and the strip planes by kapton pillars.

The design promises two advantages:

- it minimizes material thickness of the chamber;
- it keeps all chambers of a station at the same temperature, the same gas composition, and pressure.

3.3.4 Tentative layout of the MTS

As can be seen from Fig. 3.7 depicting the tentative layout of the MTS, the system could consist of 4 double layers of sensitive chambers around the beam line. Each double layer has a cylindrical shape with 8 sides. In each double layer one layer has strips parallel to the beam line, and the other layer has strips inclined by $+5°$ or $-5°$.

Digital strip readout is sufficient to obtain the necessary accuracy. On the other hand, the analogue readout would allow a better monitoring of the chambers at work. Strip signals from the MTS are to be pipelined in the same manner as the corresponding signals of the TPC.

3.3.5 General features of the system

The main characteristics of the proposed MTS are summarized in Table 3.2.

Table 3.2: MTS characteristics.

Total area, m^2	3.2
Number of modules	32
Detector sensitive area, cm^2	700
Read-out channels per module	784
Radial position of the inner layer, cm	10.0
Radial position of the outer layer, cm	20.0
Occupancy of the inner layer, %	6
Occupancy of the outer layer, %	0.5
Spatial precision r_ϕ, μm	150
Spatial precision z, μm	1000

Preliminary estimation of the cost is presented in Table 3.3.

Table 3.3: Cost estimate for the MTS.

Description	Number of units	cost / unit	total cost in k$
MMGC detectors (mechanics)	32	6k$/chamber	192
Readout electronics (strips)	35000	10$/channel	350
Mechanics/support			20
Gas system			100
HV supplies			10
R&D			65
Miscellaneous			13
Total cost			750

3.4 Outer Tracker

3.4.1 Introduction

The Outer Tracker (OT) is an ancillary straw tracker providing supplementary cross-checks for track reconstruction, and allowing an independent triggering on charged particle multiplicity at the pseudorapidity range of $|\eta| < 1$. Straw trackers are commonly used for both the accelerator fixed target [37, 38] and the collider experiments [39].

The OT will complement TOF triggering capabilities in the above-mentioned pseudo-rapidity range, allowing more detailed studies of various systematic effects.

3.4.2 Requirements

The OT is to operate successfully at high multiplicities in central $Au+Au$ collisions, have high spatial resolution (~ 200 μm), small sensitive time ($40 \div 100$ ns) and material budget ($< 0.1\% X_0$ per straw) to provide effective detector operation. The use of the segmented straws [40, 41, 42] makes it possible to reduce the detector occupancy.

To provide a low occupancy, the diameter of the straws will be 4 mm and the granularity of the barrel straws will be raised by the straw segmentation (three segments per straw). The current design of the MPD tracking system consists of a silicon vertex tracker (SVT), TPC, and TOF. The OT is to be placed between the TPC and the TOF. The sizes of the OT are presented in Fig. 3.8.

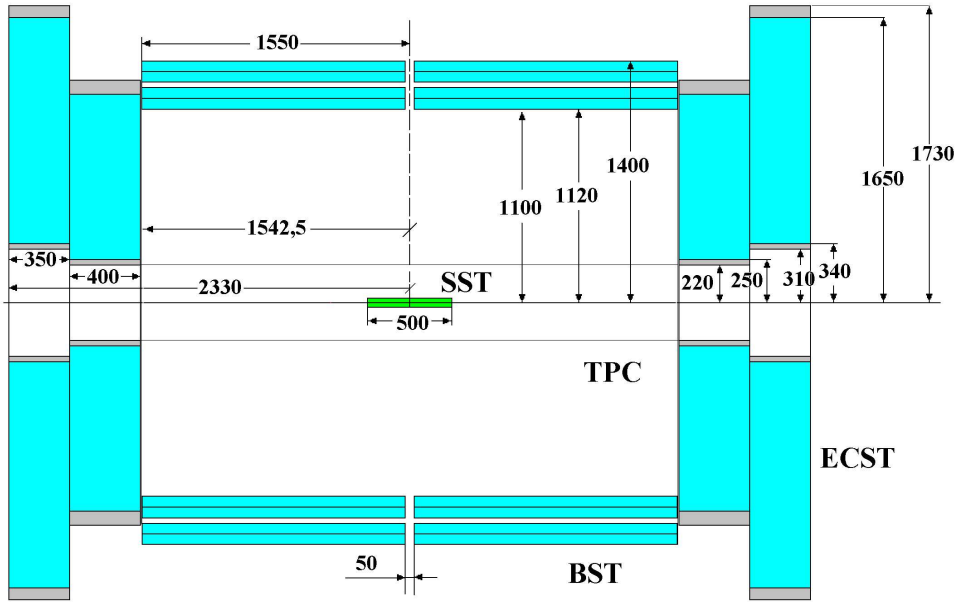

Fig. 3.8: Layout of the MultiPurpose Detector (MPD). The straw Tracker system (Endcap Tracker and Outer Tracker) is shown in gray colour.

Fig. 3.9: Common view of the OT (left) and the double layer fragments of the OT (right).

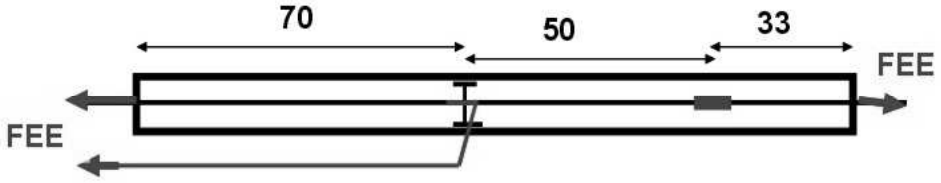

Fig. 3.10: A straw for the barrel chambers. Length of a segmented straw is ∼ 153 cm. Positions of the readout electronics of each straw segment are indicated by arrows.

3.4.3 Conceptual design

The OT is located at the overall radii of 1120 mm and 1400 mm, and at ±1620 mm in the z direction to cover the angle range ±40 degrees (Fig. 3.8). The OT consists of two modules with two double layer chambers each. The gap between the left-right modules will be about 50 mm. The construction of the OT is like the above placed TOF. Each chamber contains twelve plate fragments with 2×150 reinforced 1525 mm long straws. The overall size of one double layer of the OT fragment is 1650 mm×624 mm. The straws of each double layer are shifted by one straw radius. Each fragment will be assembled, tested, and located in the carbon plastic support frame of the OT (Fig. 3.9). The OT contains 48 fragments.

Each straw consists of three detecting segments of varying lengths; occupancies of these segments with lengths of 330 mm (central), 500 mm and 700 mm are below 4%. Fig. 3.10 shows the segmentation of the straws. Readout from the outer segments will be carried out through the end-plugs, and readout from the central segment through the straw wall by a special low-mass cable. The front-end electronics (FEE) modules are placed at both ends of each straw. The total radiation length of the double layer straw planes will be about 0.25%X_0. A summary of the major characteristics of the OT is given in Table 3.4.

Table 3.4: Summary of the OT parameters.

Feature	**Value / Quantity**	**Driving physics goal**
Angular coverage	$-1 < \eta < 1$	Improve the TPC tracking at mid rapidity
Spatial resolution	200 μm	
Efficiency for MIP	99%	
Granularity	13.2 – 28.0 cm^2	
Occupancy	$\leq$4%	
Radiation thickness	0.5%X_0	Minimize photon conversion
Number of double layers	2	Minimize gaps in occupancy
Length/diameter of straws	∼155.0 cm/0.4 cm	Cover full TPC acceptance
Total number of straws	15072	
Total number of readout channels	45216	

3.4.4 Cost estimation

For the cost estimation of the Outer Tracker we used experience of the TRT of the ATLAS collaboration. Table 3.5 presents the cost estimate for the main items of the barrel straw detectors for the ATLAS TRT and NICA. Currently we do not show financial resources related to organization of the infrastructure, Outer Tracker detector assembly area, and the test beam.

Table 3.5: Outer Tracker cost estimate

	TRT ATLAS		**NICA**		
	Number of units	**Cost per unit, k$/channel**	**Number of unit**	**Cost per unit, k$**	**Total, k$**
Total length of the straws, m	∼75000		∼24000		
Number of readout channels	105000		45300		
Mechanics		0.013		0.013	589
FE electronics and cables		0.012		0.012	547
Flexible motherboards		0.006(EC)		0.003	136
HV systems		0.005		0.004	182
Ancillary service		0.022 (EC)		0.002	74
Contingency					20%
Total					**1830**

3.5 Time of Flight System

3.5.1 Introduction

The TOF system of the MPD is the main detector for particle identification. In order to separate π/K in the momentum range 0 – 2.5 GeV/c and p/K in the range 0 – 4.5 GeV/c, it should have a time resolution better than 100 ps. The TOF system consists of two subdetectors. One includes two stations of scintillation counters situated around the beam pipe on both sides from the interaction region and designed to give the start signal. The barrel of fast detectors gives the stop signal. In the picture of the MPD detector (Fig. 2.1) the barrel TOF is marked by green colour. As a fast detector for time measurement we choose the multigap RPC (MRPC). Several experiments: ALICE[43],[44], CBM[45], PHENIX[46], STAR[47], HADES[48] have chosen the multigap RPC as a basic element of the TOF system.

3.5.2 Requirements

1. The total time resolution of the system $T_{start} - T_{stop}$ must be better than 100 ps;

2. The detector segmentation must allow for the occupancy below 10 – 15%;

3. The system must be able to work at particle flux rates up to 100 Hz/cm^2;

4. The detector must be able to work in a magnetic field up to 0.5 T;

5. The detector must cover the region $-1 < \eta < 1$;

6. The detector must be inexpensive, reliable, and simple in construction.

The density of charged particles created in central collisions in the region of $-1 < \eta < 1$ at the distance of 1.3 m from the interaction point is expected to be as large as 0.003/cm^2. For the average luminosity of the collider $L = 27$ cm^{-2}s^{-1} the rate of $Au + Au$ collisions at $\sqrt{s_{NN}} = 9\ GeV$ is about 6000 Hz. The number of charged particles per second crossing a unit of the TOF surface is

$$N = 6000 \text{ Hz} \times 0.003/\text{cm}^2 = 20 \text{ Hz/cm}^2.$$

So the TOF system has to demonstrate reliability for a particle flux up to 20 Hz/cm^2. The multigap RPC can work with high efficiency and with no time resolution degradation up to 1000 Hz/cm^2 (Fig. 3.11, [43]).

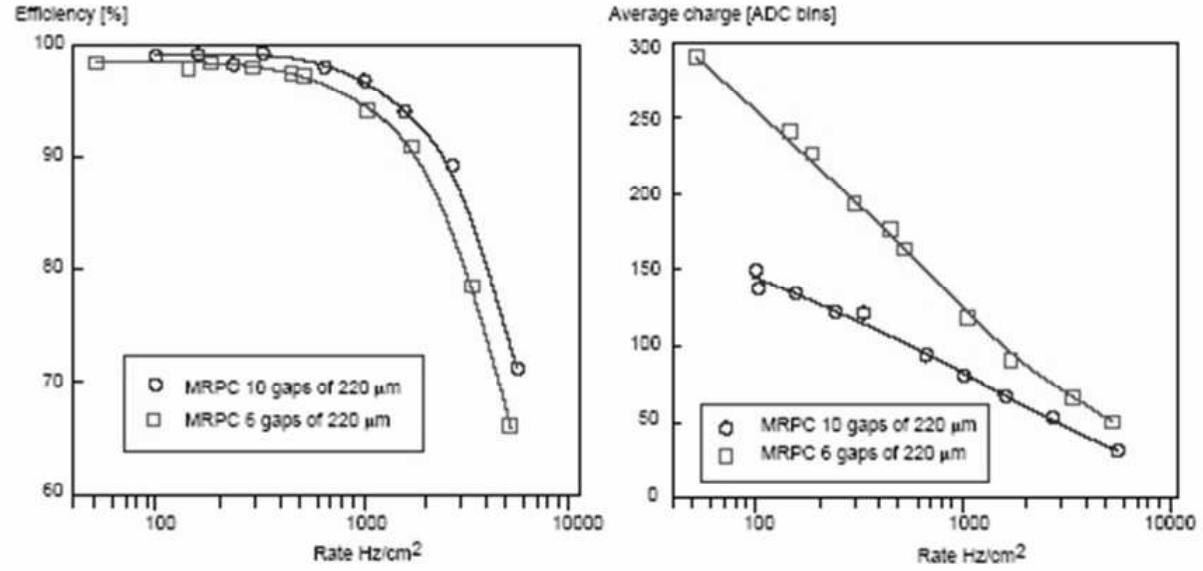

Fig. 3.11: Efficiency and average charge versus particle rate for double stack RPCs.

3.5.3 Detector design

Mechanical construction of barrel. The TOF system looks like a barrel with a length of 355 cm and radius of 1.3 m (see Fig. 3.12). Along the beam it covers the region $|\eta| < 1$.

The surface of the barrel TOF detector is about 30 m^2. The dimensions of one multigap RPC counter are 7 cm×67 cm, it has 64 pads with a size of 2.3 cm×2 cm. The RPC counters are organized in modules.

In total there are 12 modules in the barrel.

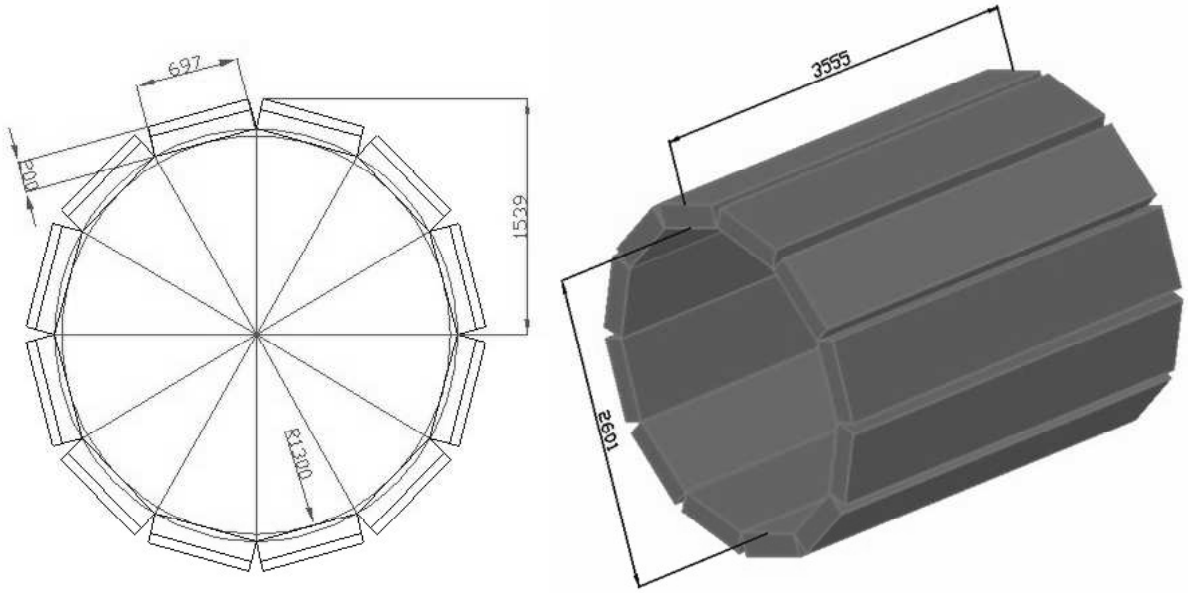

Fig. 3.12: Barrel of TOF.

The full barrel is covered by 512 counters. The total number of readout channels is 32800.

The geometry efficiency in the region $|\eta| < 1$ is 93%.

Design of one module. The layout of the multigap RPC distributed in the module is presented in Figs. 3.13 and 3.14. The detectors are to be placed in the module perpendicular to the beam axes.

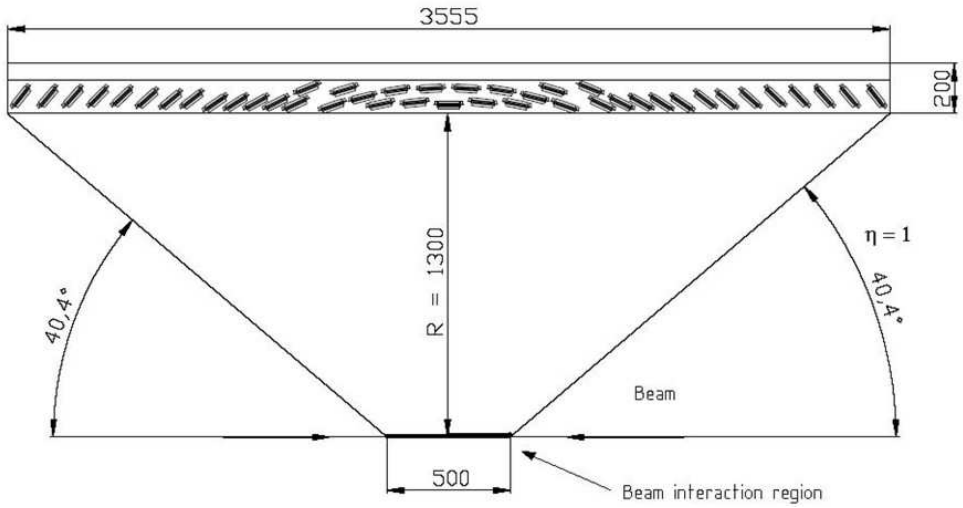

Fig. 3.13: Distribution of the RPC elements in the barrel

In total there are 43 detectors in each module. The detectors are placed in such a way that the readout pad is perpendicular to the line coming from the interaction point. In order to exclude dead zones, the detectors in the module are designed to overlap.

Fig. 3.14: View of the multigap RPCs distribution in the module box.

Design of the multigap RPC module. The multigap Resistive Plate Chamber consists of a stack of 12 plates of glass separated from each other by 220 μm thick spacers forming 10 equal gas gaps. In order to avoid a problem connected with processing a small signal and diminishing multihit signals a 10 gap construction was chosen.

The ALICE TOF collaboration [44] demonstrated that the RPC made of commercial soda-lime glass with bulk resistivity of $\sim 10^{13}$ Ω·cm can operate at a flux in excess of 1 kHz with no degradation in performance. In case of the NICA MPD the flux is expected to be less than 20 Hz/cm^2.

The scheme of the detector basic element is presented in Fig. 3.15. The detector consists of two parts of 5 gaps each. The outer glass electrodes have a thickness of 0.8 mm. The internal glass electrodes have a thickness of 0.5 mm.

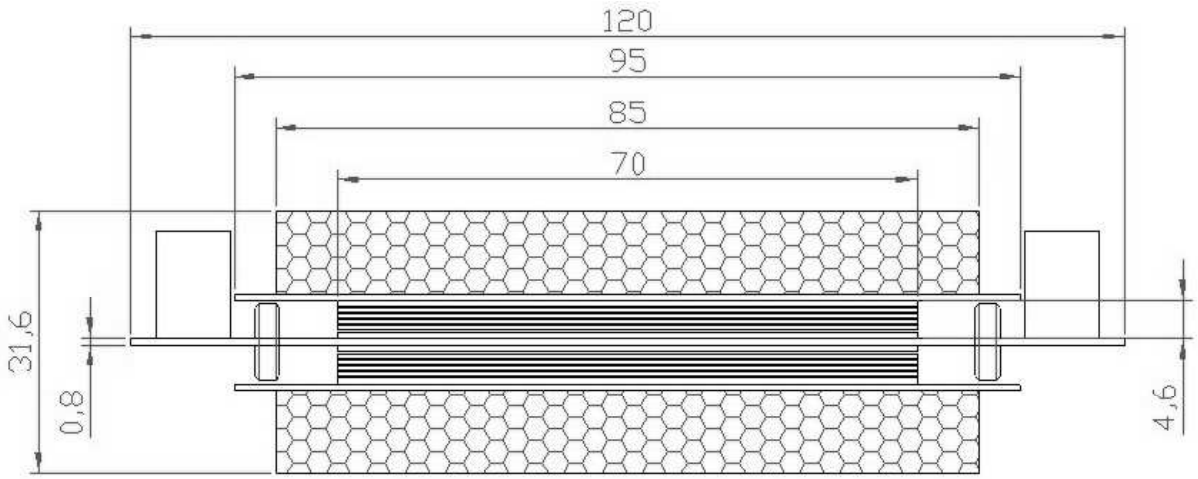

Fig. 3.15: Drawing of the basic element of the timing RPC.

The fishing line as a spacer defines the 220 μm gap between all electrodes. The outer part of two external glass electrodes is covered by a conductive tape with surface resistivity of about 5–10 MΩ/cm^2 to apply high voltage and the ground. All internal electrodes are floating. The pick up pads are made on 0.8–1 mm thick PCB board.

One has to note that the readout pad geometry and dimension is a subject of further studies. A final decision will be taken after optimization of tracking capabilities of the whole MPD detector. The coordinate from the TOF could be used as a seed coordinate

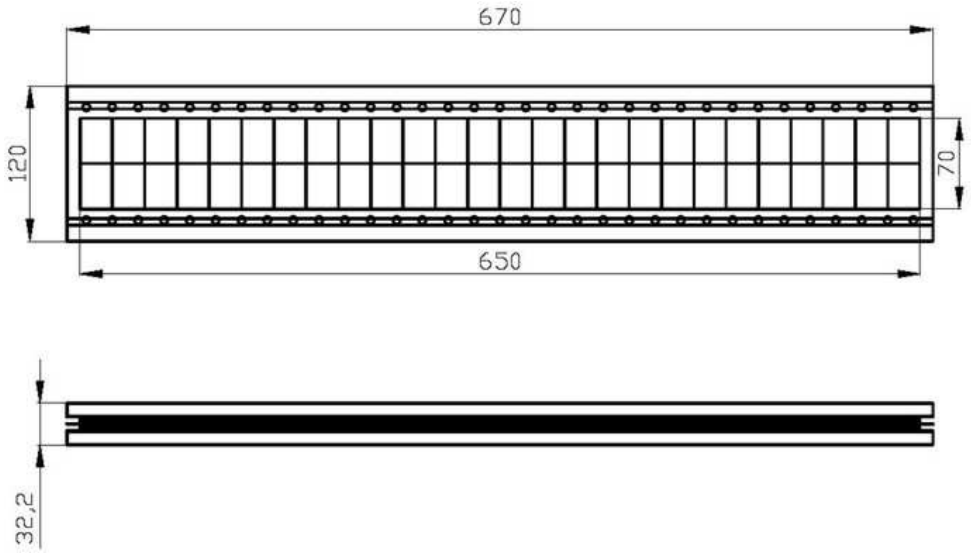

Fig. 3.16: Layout of pads on the readout plane and main dimensions of the MRPC element.

in the track finding procedure for track reconstruction by using data from the TPC and IT.

3.5.4 Time resolution and efficiency of the Start system

The start detector is an element of the TOF particle identification system. The goals of the Start detector array are the following:

- to provide start signal for the barrel TOF system with accuracy better than 50 ps;
- to measure interaction point along the beam line with accuracy of about 1.5 cm;
- to provide a signal for L0 trigger;
- to give information about event multiplicity.

It is proposed to use Cherenkov radiators coupled to photomultipliers as basic elements of the Start detector. In order to measure the beam collision z coordinate there should be two stations of Start detectors placed on both sides from the interaction point. To estimate the resolution of the start system positioned at the distance of 1 m away from the primary vertex, the Geant-4 package and the UrQMD generator were used. For the simulation the Start detectors were presented as array of disks situated around the beam pipe with an inner diameter of 10 cm and an outer one of ∼23 cm. The scheme of array is shown in Fig. 3.17. There are two arrays of detectors on the left and right sides of the MPD detector.

Figure 3.18 demonstrates the time-of-flight distributions for charged particles and photons escaping from the interaction point and arriving at the start detector placed 1 m away from the interaction point. From the distributions one can see that there are on the average about 3 photons in the time range of 10 ps, and 1 charged particle in 20 ps which get in each array of detectors from the central event and provide statistics for the start signal and measurement of the vertex position along the beam line. The time resolutions defined as differences between the time of particle arrival to the left and right detector

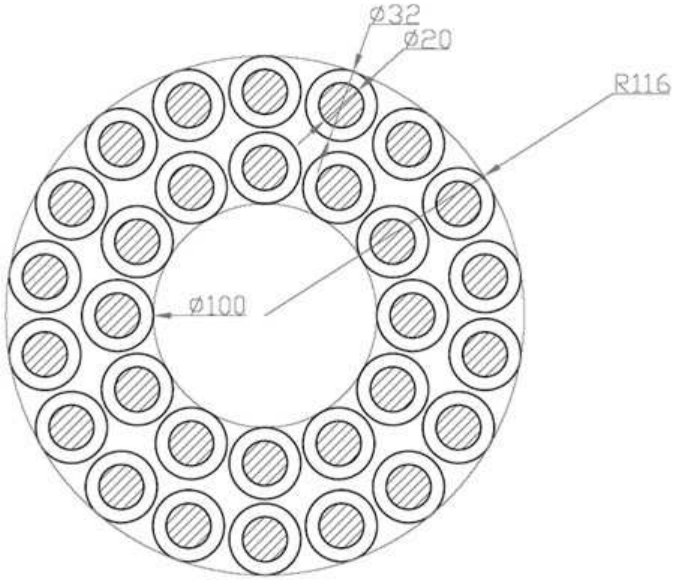

Fig. 3.17: Position of array of T0 counters around the beam pipe placed in two rows with 30 counters. Dashed circles represent quartz absorber with the diameter of 2 cm, open circle outside the dashed one is photomultiplier FEU-187 with 30 mm diameter.

arrays are presented in Fig. 3.19. One can make a conclusion that there are enough particles to provide good timing resolution with efficiency of about 99%.

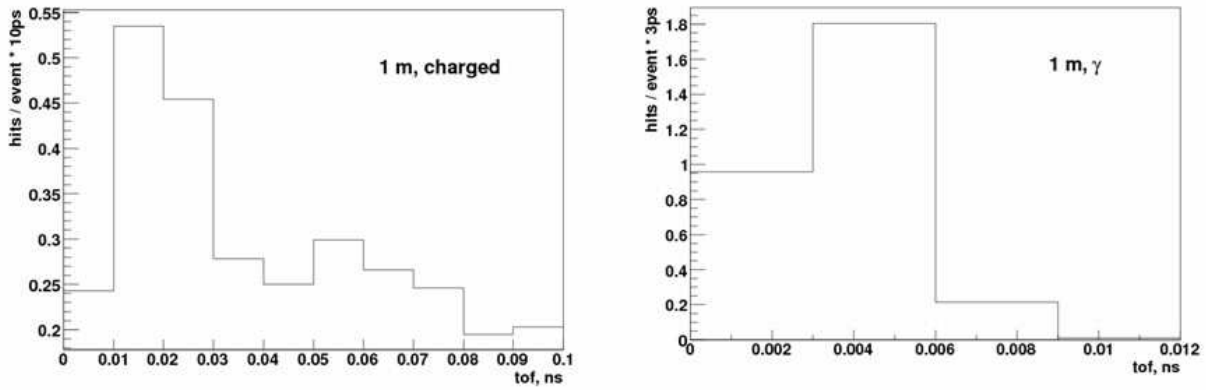

Fig. 3.18: Arrival time distribution average over one event for photons (left plot) and charged particles (right plot) to the start detector at the distance of 1 m from the interaction point.

The distribution of events when interaction products hit both the Start arrays within a time interval of 50 nsec for a various positions of the arrays along the beam line are presented in Fig. 3.20. This analysis allows one to choose the optimal position of the Start arrays along the beam.

In order to see how the efficiency of the Start system behaves if some of the phototubes fail to work during the experiment, we present the dependence of efficiency of beam interaction position measurement on the number of particles crossing both Start arrays (see Fig. 3.21).

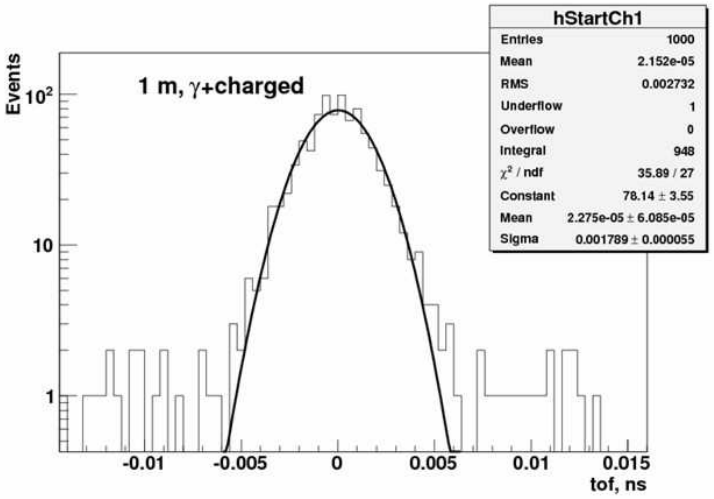

Fig. 3.19: Difference of arrival times between the left and right start detectors situated 1 m away from the interaction point. Both fast charged particles and photons were used.

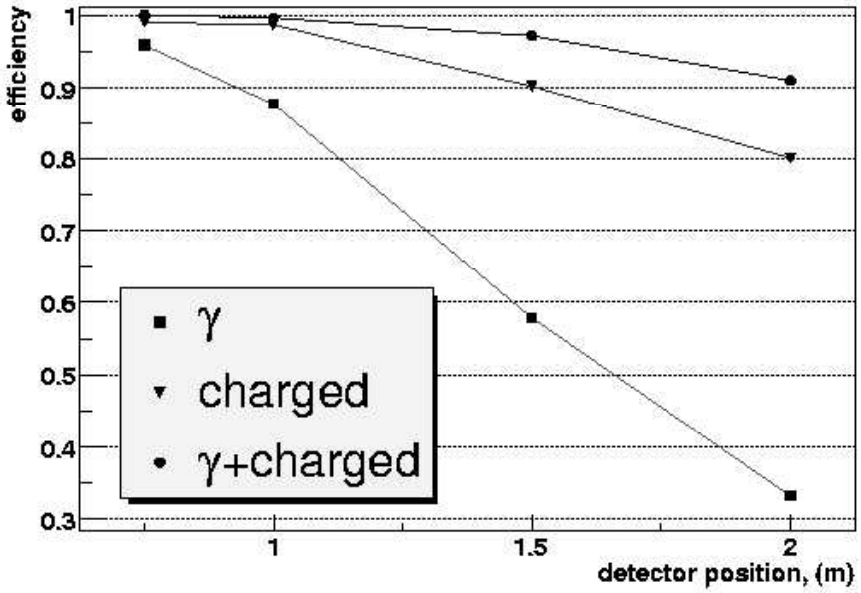

Fig. 3.20: Efficiency of the z position of beam collision measurement with two start detectors arrays as a function of their position along the beam. The beam collision density has Gaussian distribution along the z axis with a standard deviation of 25 cm.

3.5.5 Mechanical construction of the Start detectors

From the UrQMD generator one can see that there are many photons from $Au + Au$ interaction which hit the start detector. So one could choose a fused Quartz radiator with a diameter of 2 cm and 3 cm long. As a photomultiplier it is considered FEU 187 produced in Russia and R6178 by Hamamatsu Photonic. The above-mentioned phototubes have the diameter of 30 mm and 14 mm respectively. From the formula

$$N_{ph} = 2\pi\alpha \left(\frac{1}{\lambda_1} - \frac{1}{\lambda_2} \right) \sin^2 \theta$$

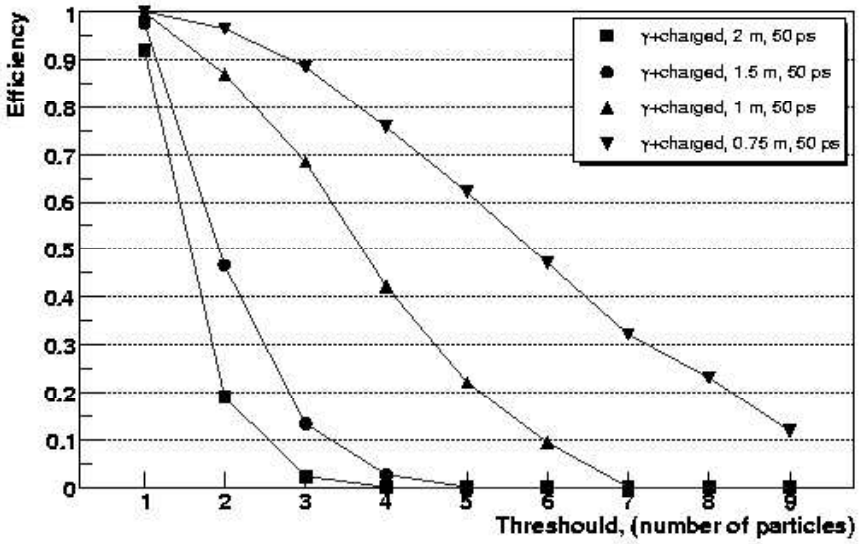

Fig. 3.21: Efficiency of the z-position measurement with left-right Start arrays as a function of a number of required coincidences for a different z position of arrays (right).

one may estimate the number of Cherenkov photons in quartz with refractive index n=1.458. For the photocathode sensitivity of FEU-187 presented in Fig. 3.22 (taken from [44]) there are 440 photons in the range of 300–550 nm. If one assumes the quantum efficiency of photocathode is around 15%, there are 66 emitted photoelectrons. Phototubes

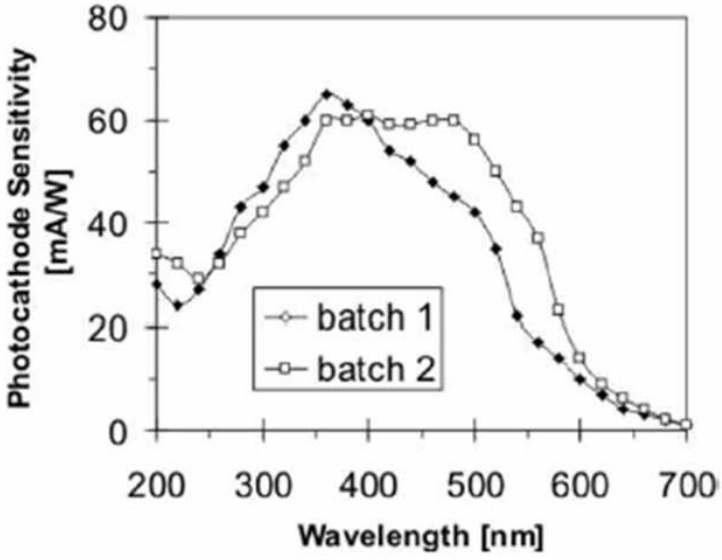

Fig. 3.22: Photocathode sensitivity of Russian phototube FEU-187

FEU 187 are chosen for the TOF Start system of Alice [43], R6178 photomultipliers were developed for PHENIX BBC [46]. Both the systems demonstrated timing resolution better than 50 ps.

3.5.6 Schedule of realization and cost estimate

Table 3.6 presents a schedule for the TOF system realization.

Table 3.6: Schedule of the TOF system realization.

Element, work	2008	2009	2010	2011	2012	2013
The first prototype test	◯					
Test of prototype of Start-Stop system		◯				
Simulation multigap RPC	◯	◯				
The first full scale prototype assembling			◯			
Beam tests of the full scale prototype				◯		
Readout electronics design and test			◯	◯		
Construction of clean room for mass production of RPC				◯		
Mass production of multigap RPC					◯	
Mass tests of assembled mRPC with cosmic rays					◯	◯
Installation of the TOF system in the MPD						◯

For estimation of the cost of the TOF barrel system the experience of the ALICE and CBM collaborations was used. The Table 3.7 presents the cost estimation for the main items of the barrel TOF detectors ALICE, CBM, and NICA.

The table does not include financial resources related to the organization of the infrastructure, TOF detector assembly area and the test beam. Authors estimate these costs to be as much as 100 k$.

Table 3.7: TOF cost estimation.

	ALICE	CBM	NICA
FE electronics (Euro/ch)	13.76	12.3	12
FEE digitizer (Euro/ch)	26.0	30.0	28
Number of channels	160000	65000	27000
Active area (m^2)	135	110	24
The total cost of electronics (k$)	6543	2800	1300
Parts of detectors, mechanical frame (k$)	3311	1900	1000
LV, HV systems, cooling (k$)	871	450	300
Cables and connectors, crates (k$)	982	400	300
Gas system (k$)	250	200	200
Start detectors (k$)			400
Spare parts, prototyping, R&D (k$)		1080	500
Total: (k$)	11957	6830	4000

3.6 Electromagnetic Calorimeter

3.6.1 Design considerations

The main goal of the photon detector is to detect γ, e^+/e^- and to reconstruct π^0 and measure its momenta. In order to reach the required sensitivity in the π^0 reconstruction under the conditions of a high photon flux, we have to measure the photon energy with high precision.

The expected high multiplicity environment (Fig. 3.23) implies a high segmentation of the calorimeter, a large enough distance to the vertex, and the use of a dense active medium with a small Molière radius. To have an adequate space resolution and allow separation of overlapping showers, the transverse cell size should be of the order of the Molière radius. A minimal shower overlap is required in order to ensure a reliable reconstruction of photons and mesons. The particle occupancy should not exceed 3% in order to be able to determine the photon reconstruction efficiency with high accuracy. At this occupancy the photon reconstruction efficiency can be measured to an accuracy of 2%.

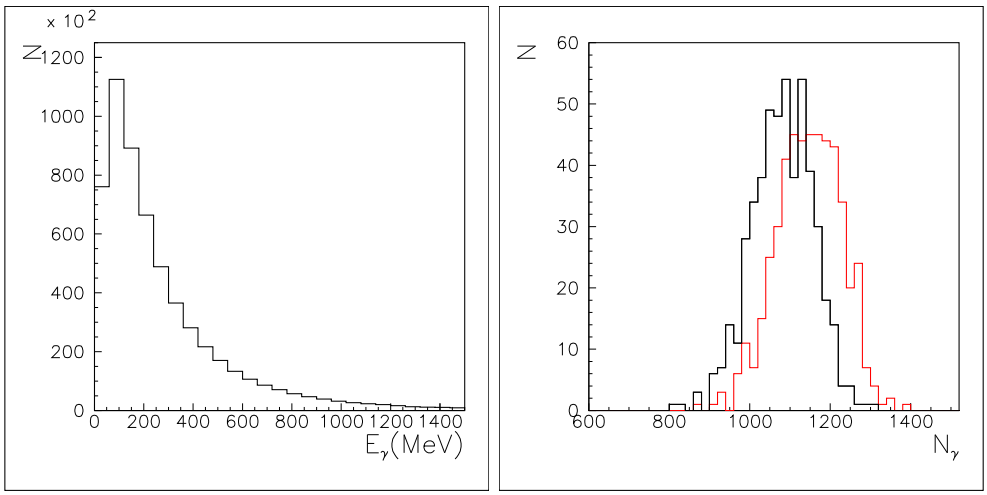

Fig. 3.23: Energy spectrum of photons (left) and photon multiplicity distribution (right) in the central Au + Au collision ($\sqrt{s_{NN}}$ = 9 GeV). Photons from the π^0 decay are presented by the red colour.

A material with a small Molière radius is needed for the photon detection (at r = 1.3 m) in order to keep the occupancy within the required range in central $Au + Au$ reactions (up to $N_\gamma \sim 1000$), Fig.3.23. Rectangular 3×3 cm detector cells will guarantee occupancy below 3% for all regions (Fig. 3.24).

Energy resolution of the photon detector is a critical point in the conditions of high photon multiplicity (Figs. 3.25, 3.26). It is highly desirable to achieve an energy resolution below 2.5%. A study carried out by the COSY collaboration [49] proves it to be possible.

Neutral hadron rejection can be achieved by a cut of the shower width, which operates at all energies, and/or by a cut of time of flight. Indeed, over a distance of 1.3 m, hadrons will arrive later than a photon. This may cover a relevant energy range. Therefore, an option of sub-nanosecond time-of-flight measurement in the photon detector is currently under study and will be described later.

Finally, the photon detector must be able to operate in the full MPD magnetic field up to 0.5 T and it should be compact enough to be integrated into the MPD set-up.

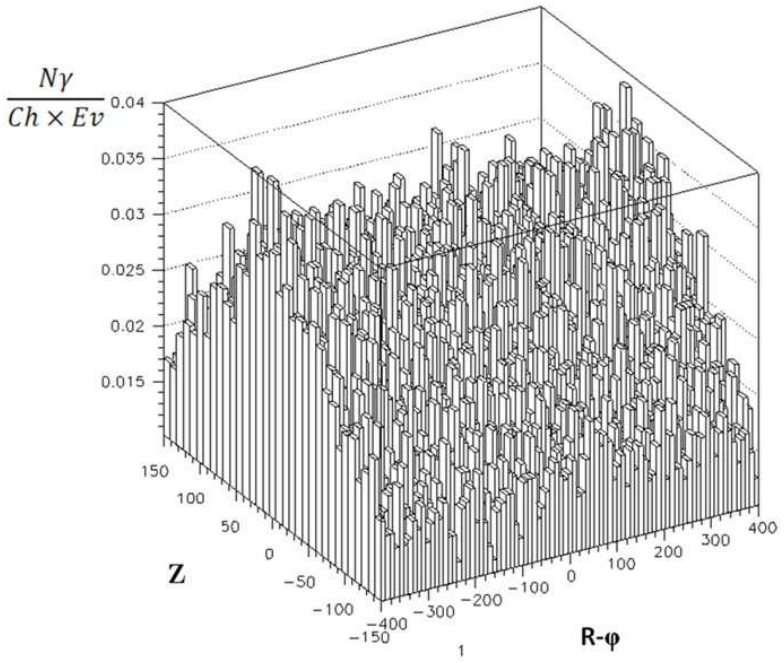

Fig. 3.24: Average occupancy per channel for the barrel part of the MPD photon detector equipped by the 3×3 cm crystals. Central Au + Au collision ($\sqrt{s_{NN}} = 9$ GeV).

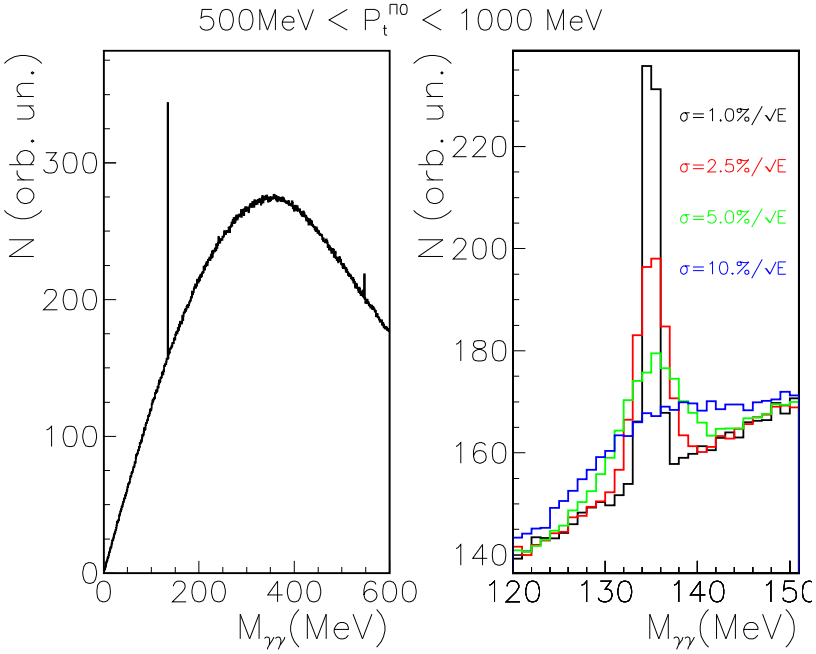

Fig. 3.25: The π^0 reconstruction in the intermediate P_{π^0} transverse momentum regions for various photon detector energy resolution. Left plots: ideal detector. Central Au + Au collision ($\sqrt{s_{NN}} = 9$ GeV).

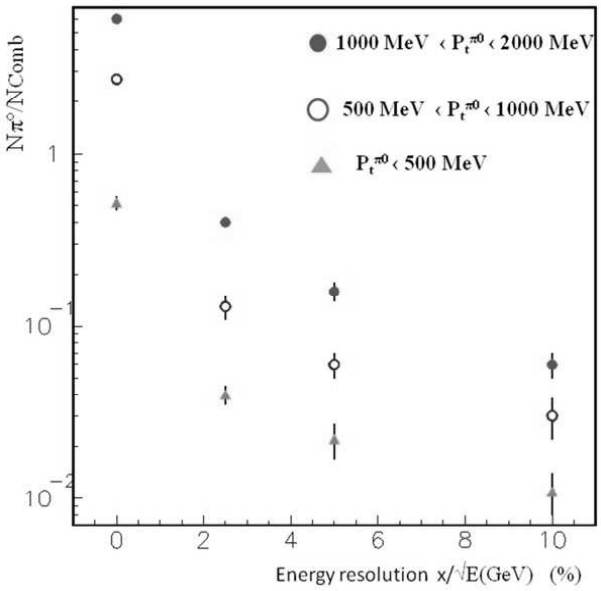

Fig. 3.26: Ratio of reconstructed π^0 event number to that due to combinatorial background in various P_t regions vs calorimeter energy resolution.

3.6.2 Module design

Two solutions satisfy the listed requirements for the MPD electromagnetic calorimeter. Authors consider a lead scintillator of "Shashlyk" type as a baseline option of calorimeter, that is a well proved and cost effective solution for this kind of detectors. If physics dictates the necessity to have the ultimate performance of the electromagnetic calorimeter, an optional solution based on lead-tungstate crystals can be considered.

In the following we describe the design for both the options.

1. Baseline option - "Shashlyk" calorimeter

The Pb-scintillator electromagnetic calorimeter of the "shashlyk" type can be used in the MPD detector. This kind of calorimeter is used in the PHENIX [50], KOPIO [51], LHCB [52], T2K [53], and some other detectors. Calorimeters of this type have a relatively low cost, provide good radiation hardness, and have a robust design. Their energy resolution can be as good as $\sim 3\%/\sqrt{E}$. Their spatial resolution is determined by optical segmentation and can be easily adjusted to the requirements of the experiment. It is interesting to note that the "shashlyk" calorimeter can in addition provide time resolution of about $100 - 150$ ps as a complementary time-of-flight measurement.

An example of a "shashlyk" calorimeter module is shown in Fig. 3.27.

For the MPD electromagnetic calorimeter it is proposed to have the basic building block as a module (e.g., 12×12 cm^2) consisting of 16 optically isolated towers which are read out individually. Each Pb-scintillator tower contains 100 sampling cells consisting of alternative tiles of Pb and a plastic scintillator. The cells of each tower are optically combined by 9 longitudinally penetrating wavelength shifting (WLS) fibers for light collection. The light collected with 9 fibers is read out by avalanche micropixel photodiode (AMPD) units with a sensitive area of 3×3 mm^2. The 16 towers, mechanically grouped together, make a module. The module with 18 radiation lengths will have a thickness of approximately 36 cm. That will increase the size of the solenoid magnet by ∼10%

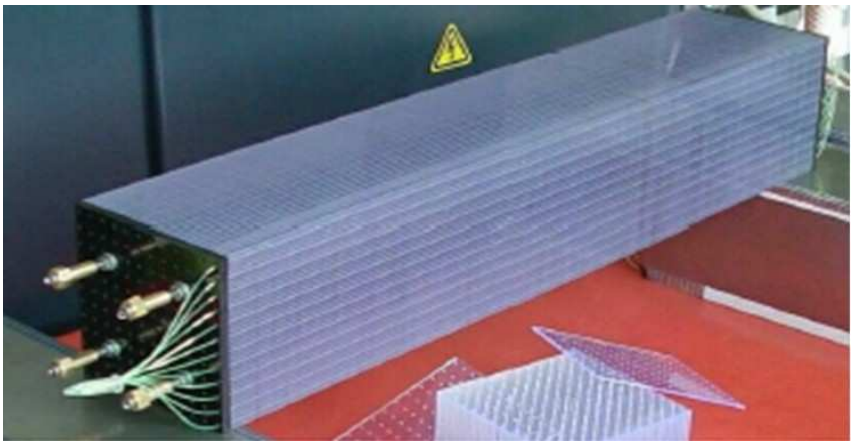

Fig. 3.27: A "shashlyk" module.

with respect to the crystal calorimeter option (its module has a size of 22 cm). In the forward region, where the longitudinal size is not so critical and, moreover, the radiation hardness is a key parameter, the "shashlyk" calorimeter is fully adequate to the design requirements. The π^0 yields and spectra are to be measured via their two-photon decays. The measurement has to be carried out with special care, i.e. high and well-known accuracy, in the 50 MeV/c – 2 GeV/c momentum range (Fig. 3.23), to determine precisely the background for the measurement of direct photons in the same full p_t range. For a detector of a given area and shape the efficiency depends on the details of crystal positioning. This will be selected after MC simulation. The geometrical acceptance was calculated by means of a Monte Carlo simulation.

The π^0 yields will be extracted from the invariant mass spectrum, on top of a large combinatorial background. The signal-to-background ratio S/B is inversely proportional to the mass resolution σ_M. A better mass resolution entails higher statistical significance and lower systematic errors for the meson yields and spectra.

The mass resolution is given by the following expression:

$$\frac{\sigma_M}{M} = \frac{1}{2}\sqrt{\frac{\sigma^2_{E_1}}{E_1^2} + \frac{\sigma^2_{E_2}}{E_2^2} + \frac{\sigma^2_{\Psi}}{\tan^2(\Psi/2)}},$$

where E_1 and E_2 are the photon energies and Ψ is the opening angle between the photons, whose error is given by the position error. The energy resolution can be parameterized as (E in GeV)

$$\frac{\sigma_E}{E} = \sqrt{\frac{a^2}{E} + \frac{b^2}{E^2} + c^2},$$

where a is the stochastic term, b is determined by the readout noise, and the constant term c is due to the detector and readout inhomogeneity and to the calibration error. Since the photon detector will measure relatively low-energy photons ($E < 2$ GeV), the first two terms are more important than the third. The prototypes of the "shashlyk" type calorimeters were extensively studied by several collaborations. As an example, the results of the test beam study of the KOPIO "shashlyk" calorimeter are shown in Fig. 3.28. The results are in excellent agreement with the simulation.

The main parameters of the "shashlyk" calorimeter are presented in Table 3.8.

Estimated cost of each module is 888 $. It includes the items listed in Table 3.9.

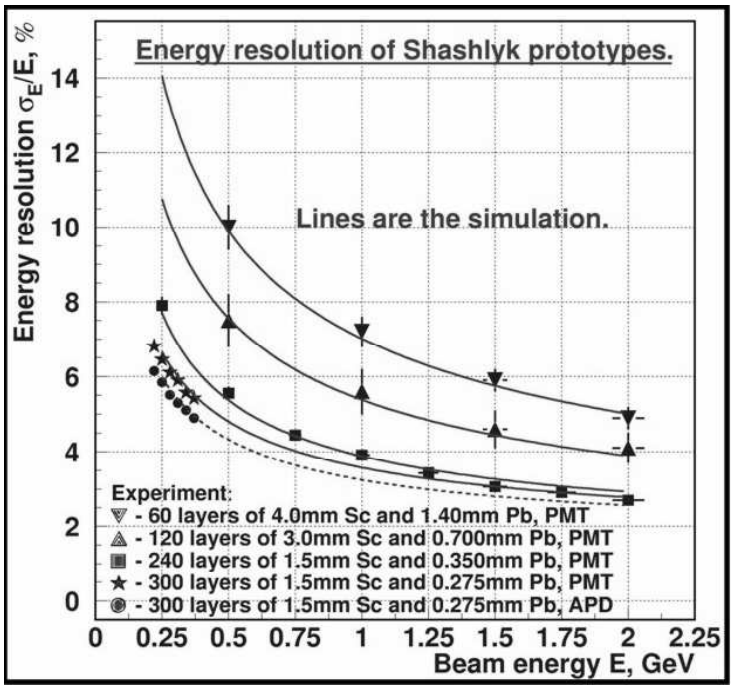

Fig. 3.28: "Shashlyk" calorimeter beam test results.

Table 3.8: Parameters of the prototype "shashlyk" module for the AMPD.

Transverse size	120×120 mm^2
Number of layers	100
Polystyrene scintillator thickness	2.0 mm
Lead absorber thickness	1.0 mm
Number of holes per layer	12×12
Hole spacing	10 mm
Hole diameter	1.2/1.3 mm
WLS fibers per module	144×0.5 m≈72 m
Diameter of WLS fiber	1.0 mm (1.2 mm)
Dimension of fiber bundle	3×3
Effective radiation length, X_0	17
Effective Molière radius, R_M	37 mm
Active length	306 mm/18X_0
Number of AMPD per module	16

2. Optional solution - Lead-tungstate calorimeter

Lead tungstate ($PbWO_4$) crystal is the promising material for the photon detector. Today, it is still the only material which fulfils requirements for the Molière radius, light yield, and cost. This crystal was chosen by the CMS, ALICE and COSY collaborations for their electromagnetic calorimeters, although the experimental conditions in their studies are quite different.

The possibility of using this crystal for electromagnetic calorimetry has been studied

Table 3.9: Estimated cost of a "shashlyk" module.

Plastic scintillator (100 plates $120 \times 120 \times 2$ mm^3)	222 \$
Lead plates (100 plates $100 \times 100 \times 1$ mm^3)	148 \$
Wavelength shifting fibres	165.2 \$
Other components and assembly work	310.8 \$

in recent years [54, 55, 56, 57, 58, 59, 60], and very significant progress was made towards its use in large calorimeters. Its physical and chemical properties are given in Table 3.10.

Table 3.10: $PbWO_4$ properties.

Density	8.28 g/cm^3
Radiation length	0.89 cm
Interaction length	22.4 cm
Molière radius	2.19 cm
Melting point	1123 ^{o}C
Hardness	4 Moh's
Refractive index along z axis (λ=632 nm)	2.16
Decay time, ns	5 (39%) 15 (60%)
Hydroscopicity	none
Chemical activity	inert

Lead tungstate is a scintillating monocrystal with a rather complex emission spectrum, including two broad bands of 440 nm and 530 nm. The decay time constant has a mean value of about 10 ns at room temperature.

The light yield of lead tungstate crystals at room temperature is 5% of that of BGO, i. e. 40-65 photons/MeV for a 16 cm long crystal. However, the light yield is constantly being improved and the most recent crystals produced for CMS have reached more than 80 photons/MeV. Rather good longitudinal response homogeneity was measured for a crystal coupled to a photomultiplier and exposed to a ^{60}Co source which was displaced along the crystal.

The light yield strongly depends on the temperature. The temperature coefficient is $-2\%/1°$C at 20°C, and increases to $-4\%/1°$C at $-25°$C, as shown in Fig. 3.29.

The temperature dependence offers the possibility to increase the intrinsic light yield of the crystal. At a working temperature of $-25°$C the light yield will be enlarged by about a factor of 2.5 and furthermore the electronics noise of the photon detector will be reduced. Both the effects will lead to an improved energy resolution.

Lead tungstate ($PbWO_4$) is grown from a 50%–50% mixture of lead oxide (PbO) and tungsten oxide (WO_3). Homogeneous crystals can be grown to the required size by the Czochralski technique in platinum crucibles. The large-scale crystal production technology exists, e.g. in Russia and Ukraine. Considerable variations in optical properties are induced even by small changes in the crystal production process.

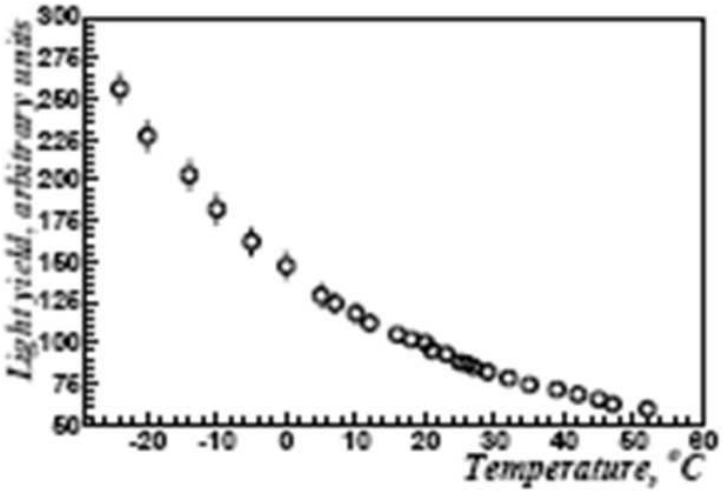

Fig. 3.29: The light yield temperature dependence for the $PbWO_4$ crystal.

The primary choice for light readout is the silicon PIN diodes. However, PIN diode response to charged particles traversing them and the energy resolution can be spoiled by this shower punchthrough effect. This effect will be acceptably small at a crystal length of 16 cm. Thus 16 cm long single crystals with transverse size 3×3 cm^2 have been preliminarily chosen as an MPD photon detector. A final decision concerning crystal segmentation, location, and type of the light detectors can be taken only after extensive simulations and beam tests.

The stochastic and constant terms a and c (which are most important terms[61]) have been measured to be $a = 3\%$ and $c < 1\%$ [62], with some of the most recent results as low as $a = 2.8\%$ and $c < 0.5\%$ [50].

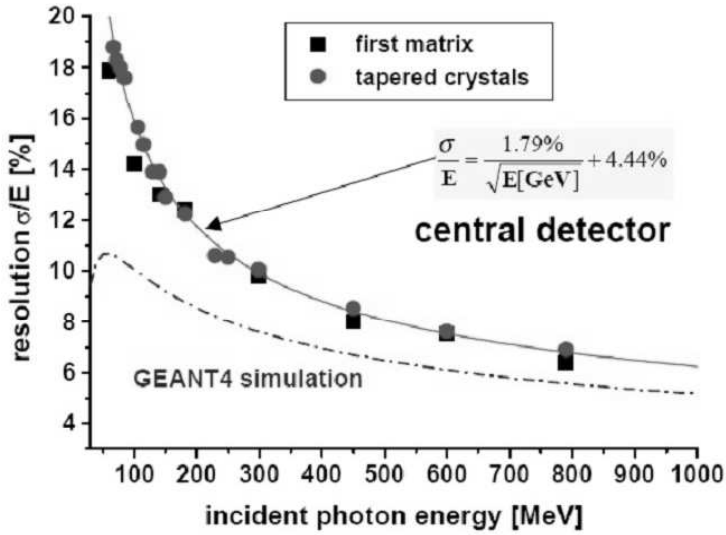

Fig. 3.30: $PbWO_4$ crystal energy resolution vs incident photon energy.

With a light yield of 80 photons/MeV at 20°C one could expect up to 200 photons/MeV at a temperature of −25°C. Cooling of the electronics, which is placed close

to the crystals, as well as ongoing R&D for light detectors, and preamplifier optimization will lead to further improvement.

The basic element of the calorimeter is a module of the size $3\times3\times16(50)$ cm^3 wrapped in Tyvek. Light detectors are glued onto the outer face of the crystal. Every 64 crystals arranged in a 8×8 square will form a module of size $24\times24\times22(55)$ cm^3, including light detectors and preamplifiers. The module will have 0.5 mm thick walls made of a folded aluminium plate fixed to the aluminium support. The photon detector module is shown in Fig. 3.31.

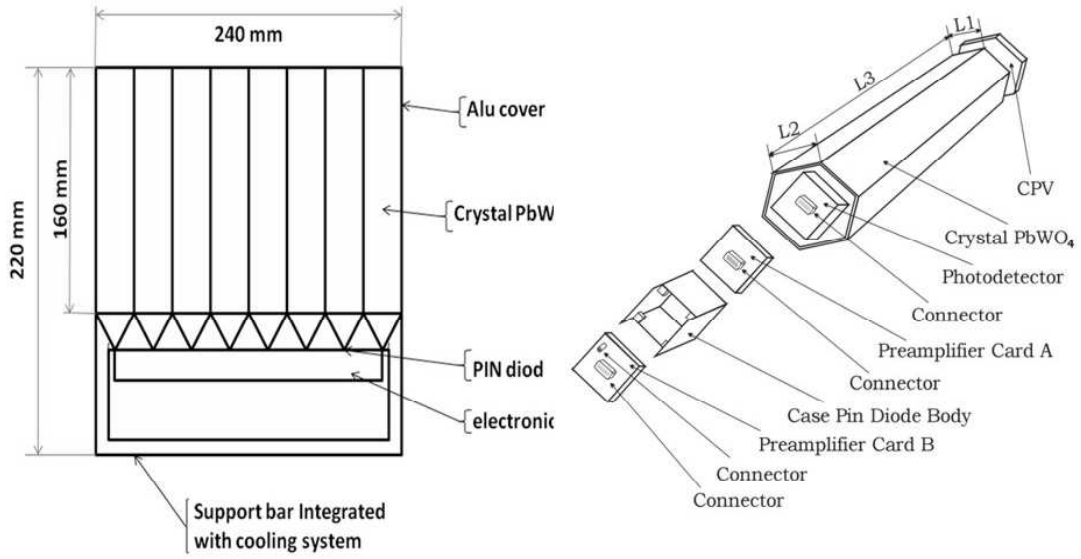

Fig. 3.31: Two variants of the photon detector module.

Fifteen modules will be mounted in line on a 3.5 m long, U-shaped aluminium bar parallel to the beam axis. The photon detector will comprise a total of 34 U-shaped bars (15 modules in each bar), 510 modules with 32640 crystals in the barrel part. Similar structure with 9070 crystals will form endcaps. Its total area will be 28.6 m^2 in barrel and 8.6 m^2 in the endcaps.

The heat-producing electronics will therefore be separated from the modules and mounted inside the bars. The bars will be cooled. If the crystal-based detector is chosen, an extra cooling system with binary ice for the crystals will be needed. Only the light detectors which have a very small heat output (2 μW per channel) will be in close contact with the $PbWO_4$ crystals. Thermoinsulation of each module as a whole will help to keep the inside temperature stable around -25°C with 0.1°C accuracy. Binary ice is chosen as a coolant because it provides a possibility to maintain low temperature with high precision.

3.6.3 Photodetector

Photon detector is to be operated inside a magnetic field of up to 0.5 T. This requires a readout which is able to operate in this field. The PIN photodiode with the amplifier is considered as the best candidate. It is compact and insensitive to magnetic fields. The present design makes use of 10×10 mm^2 PIN diodes but can easily incorporate larger area diodes. The choice will mainly depend on the development of future costs. The use

of PIN diodes presents, however, certain disadvantages. They are sensitive to charged particles, so even a small shower leakage can worsen the energy resolution.

The alternative option would be an avalanche micropixel photodiode (AMPD) which is a novel photodetector with a multipixel intrinsic structure on the common silicon substrate. The advanced version of the AMPD with a deep microwell for charge collection has density of pixels of more than $10^4/\text{mm}^2$ [63]. Each pixel works as an independent photon microcounter on the common load in the Geiger mode, where the discharge is limited by an individual quenching resistor (negative feedback like in the gas Geiger counter) included in each pixel feeding chain located on the common substrate. Actually, each pixel operates digitally "yes/no" in response to an incident photon but AMPD as a whole is an analogue device which can measure the light intensity within the dynamic range corresponding to the total number of pixels. Figure 3.32 shows the AMPD design structure, principle of operation, and a general view.

The required design parameters of the calorimeter determine also requirements to the photodetectors: they have to be compact, insensitive to the magnetic field, and a have large dynamic range and linearity when measuring particle energy. The Deep Micro-Well AMPD matches these parameters exactly. The present AMPD design of 3×3 mm^2 can be easily used for light detection of 9 fibers of a "shashlyk" calorimeter single tower. For the crystal option the sensitive area of the AMPD could be increased or several AMPD per module can be used.

3.6.4 Calibration and monitoring

In order to keep the energy and space resolution of the calorimeter at the required level, the detectors and readout electronics have to be calibrated and monitored. Each tower (or crystal) of the calorimeter photon detector will be calibrated before installation with a relatively low-energy (hundred MeV) electron test beam at several electron energies.

Additional *in situ* calibration will be performed during datataking by using the photodetector amplitude spectra. The truncated mean of the amplitude spectrum can be used for relative calibration and the π^0 peak position for absolute calibration. Monitoring will be carried out constantly during datataking. Light emitted by the LED will be used for the continuous calibration of a full readout chain.

In case of the lead-tugstate crystals the following additional values will be monitored:

- The temperature of the lead tungstate crystals with 0.1°C accuracy – one measurement per module (64 crystals).
- The gain of the readout electronics. For this purpose each preamplifier will have a calibration input. One measurement per crystal will be performed.
- Transparency of the lead tungsten crystals and their optical contacts with the light detectors. This value will be monitored by calculating the truncated mean of the spectrum of each crystal for a certain time (typically 5–20 minutes) and comparing it with previous measurements. One value per crystal will be measured.

If the PIN diodes are chosen as photodetectors, there will be no need for gain monitoring. However, if the AMPD will be chosen for light detection, additional monitoring systems will be needed.

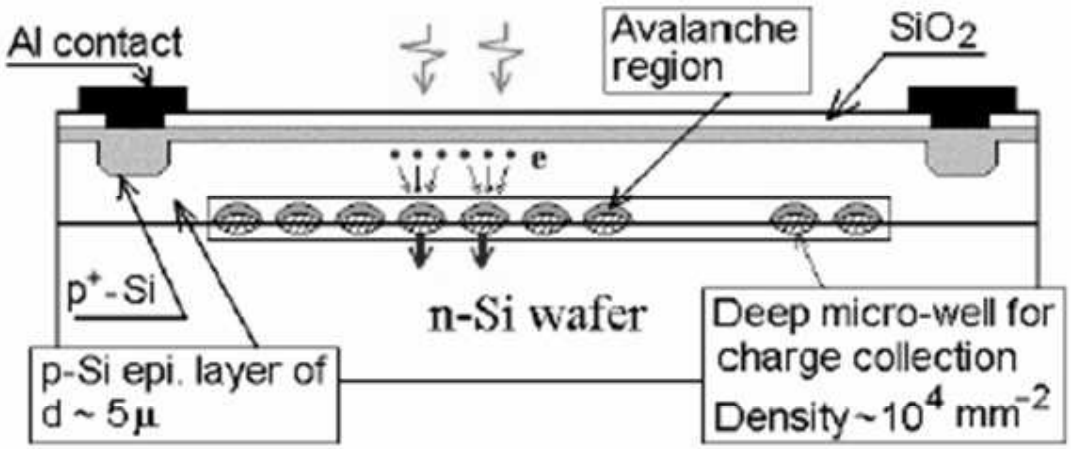

AMPD with deep micro-wells

Patent application #2005108324 from 24.03.2005.

Fig. 3.32: AMPD detector.

3.6.5 Cost

Cost estimation for the Barrel calorimeter as well as the prices of its components are presented in the Table for both the main and the optional versions. The cost of the EndCap calorimeter is estimated to be 1924 K$ in case of the "shashlyk" version and 4292 K$ for the crystal one.

Table 3.11: Estimated cost of Barrel (PbSc/PbWO4 options).

Item	Unit price ($)	Cost (K$)
Barrel (32640 detectors)	56.2/207.2	1924/6808
PIN-preamp/MAPD	29.6/148	1036/4884
Mechanics, cooling		444
FEE	44.4	1480
Monitoring system		296
Tools		148
Prototype		296
Total		5624/14356

Chapter 4

MPD End-Cap Design

4.1 EndCap Tracker

4.1.1 Introduction

The EndCap Tracker (ECT) is a straw tracker which is proposed to extend the acceptance of the MPD experiment and enhance the TPC tracking at the pseudorapidity range of $1 < |\eta| < 2.5$. It covers the full azimuthal range on both sides of the MPD and measures momenta and production rates of positively and negatively charged particles. Event-by-event observables like $\langle p_T \rangle$, fluctuations of charged particle multiplicity, and collective flow anisotropies can also be studied. The increased acceptance improves the general event characterization in the MPD and allows the study of asymmetric systems like $p + A$ collisions. Furthermore, the ECT will significantly enhance the triggering capabilities of the MPD and improve event reaction plane detection.

4.1.2 Requirements

The above physics opportunities set the requirements for the EndCap Tracker. The primary requirement for the ECT is to provide a high spatial resolution for the track reconstruction and successful operation at high multiplicities in central $Au+Au$ collisions.

Technical aspects are described in the Barrel Straw Tracker section of this document (see also [37, 38, 39, 40, 41, 42]). The ECT is to be located behind both sides of the TPC. The sizes of the ST are shown in Fig. 3.8 (BST section).

4.1.3 Conceptual design

The ECT is located near the beam pipe on both sides from the interaction region to cover the θ angle range from 10 to 43 degrees (Fig. 3.8). Each of the left and right EndCap detectors is located in the z-range of (1550÷2330) mm from the detector center, and contains three (two module option is considered as well as a minimal one) wheel modules each with the overall radii of ∼1290 mm, 1730 mm, and 1730 mm, respectively. The first module consists of seven wheel submodules with the 960 mm long straws, the second contains six wheel submodules with the 1310 mm long straws, and the third contains three wheel submodules with the 700 mm long straw. The thickness of the submodule with four straw layers is ∼60 mm. Each wheel submodule consists of two main carbon-plastic rings with the holes for straw installation and an additional one for creation of the outside gas-manifold. The angle precision of the holes should be within 0.002°. The 4 mm diameter reinforced straws will have the radial positioning or possibly non-radial (variable angle) positioning (to be clarified during the R&D phase), see Figs. 4.1 and 4.2 for details. Currently the possibilities of the radial and variable angle (±7°) positioning

of straw layers are explored. In the variable angle design every submodule will have two layers with the radial (straight) straw positioning and two layers with $+7^\circ$ and -7° inclined straws. Each layer will have the identical straw density.

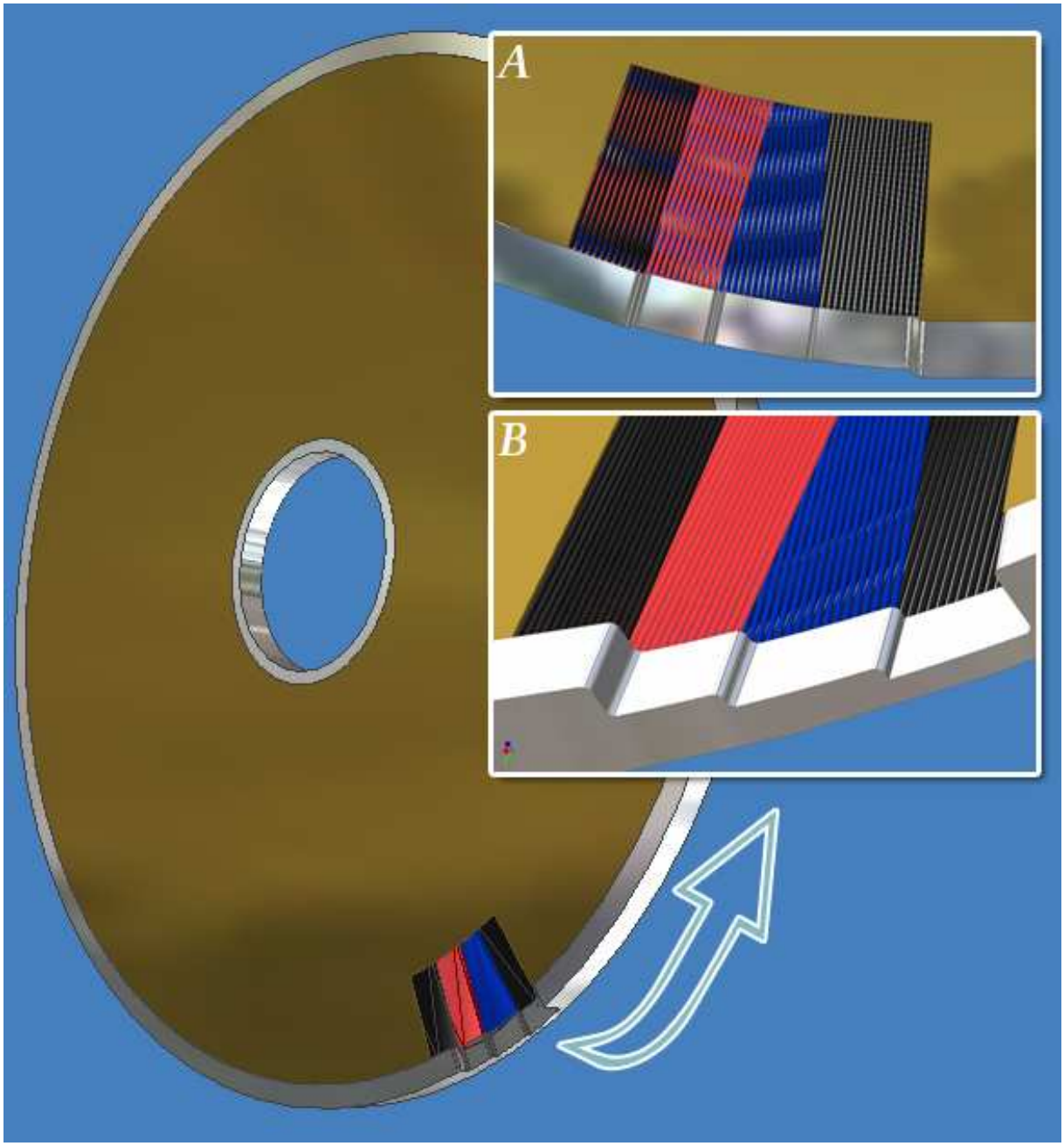

Fig. 4.1: Artistic view of the ECT submodule with four straw layers. A,B zooms show details of the internal straw positioning: A) $\pm 7^\circ$ inclined angle of the second and third layers; B) equidistant positioning of adjacent layers.

The distance between the straw centres of two neighbouring straws of the layer will be about 5.2 mm for the inner ring of the submodules, the interior angle will be 1.196/0.876/0.314 degrees for the first, second, and third modules, respectively. The relative angle incline of the same name straws for the subsequent layers of the wheel will be $0.3^\circ/0.22^\circ/0.078^\circ$ for the first, second, and third modules (radial design), respectively.

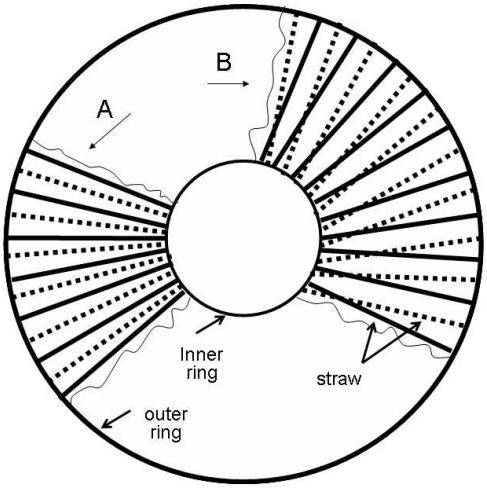

Fig. 4.2: Fragments of schematic designs for two subsequent straw layers : A) radial positioning; B) positioning with variable straw angle. The first straw layer is shown solid lines, dashed lines represent the second straw layer. A single design will be selected for the final ECT setup.

The ECT will be made of up to 64 straw layers per each side.

The primary track reconstruction parameters for the ECT are track pseudorapidity which is extracted from the number of hits in the ECT azimuthal angle, which is determined by straw spatial resolution and the track curvature which is determined by an angular shift of straw hits in sequential layers.

Estimation of the number of hits per track vs. particle pseudorapidity (for the first ECT module only) by using radial straw positioning is shown in Fig. 4.3 (left). It was simulated using the full Geant tracking (realistic straw geometry description) in the magnetic field 0.5 T. These results allow extracting the initial pseudorapidity information from ECT data. It is expected to obtain better results with the variable angle straw positioning. Basic estimation for an average number of hits for three modules is shown at Fig. 4.4. Fig. 4.5 gives an impression on how the track reconstruction efficiency vs. pseudorapidity will look like. Estimation of the expected TPC reconstruction efficiency (rough, based on STAR experience) is shown in grey and the expected ECT efficiency is shown in blue.

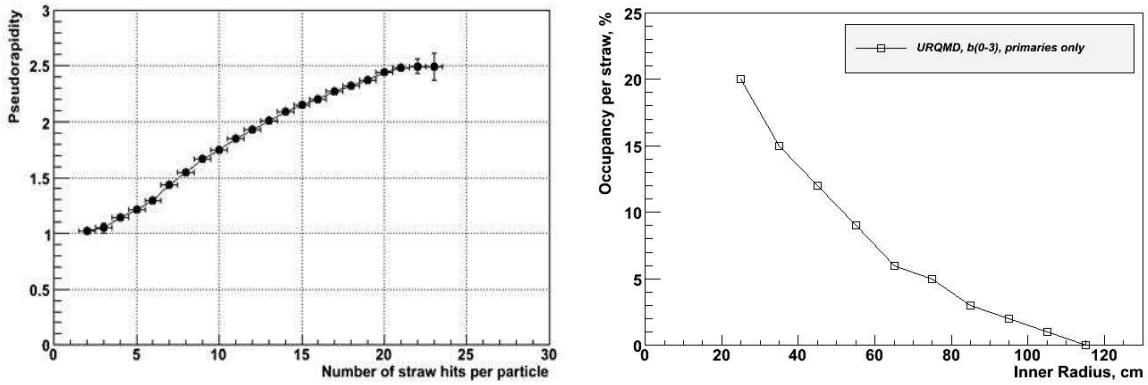

Fig. 4.3: Number of straw hits vs pseudorapidity (left) and occupancy per straw vs variable inner radius (right) of the first module of the EndCap Straw Tracker.

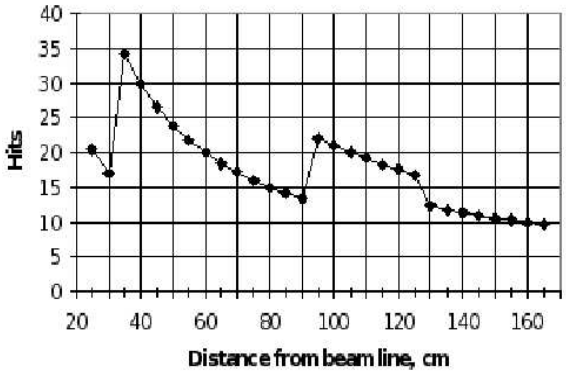

Fig. 4.4: Number of the hits for the ECT with three modules.

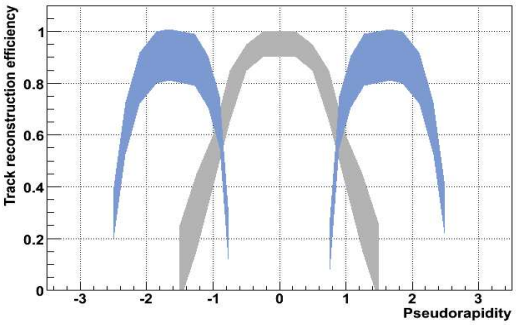

Fig. 4.5: Expected track reconstruction efficiency versus pseudorapidity for the TPC (grey filled area) and ECT (blue filled area). See text for details.

Table 4.1: Summary of the ECT (M1+M2) parameters.

Feature	**Value/Quantity**	**Driving physics goal**
Pseudorapidity coverage	$1 < \|\eta\| < 2.5$	Event-by-event observables like $\langle p_T \rangle$, fluctuations of charged particle multiplicity and collective flow anisotropies studies
Number of straw layers (per side)	52	
Angle resolution, rms	0.3°	
Radiation thickness of ECT (per site)	$< 2.95\% X_0$	Minimize photon conversion
Occupancy	$\leq$20% (TBD)	Minimize charged hadron occupancy
Straw length/diameter, cm	96/0.4 and 131/0.4	
Total number of straws	~64000	

The most important parameter is the detector occupancy in central $A + A$ events. Figure 4.3, right, shows the ECT occupancy estimation for central $Au + Au$ collisions at $\sqrt{s_{NN}} = 9$ GeV from the URQMD model prediction. In these calculations, the inner radius is varied (outer radius is fixed at 1210 cm), and the occupancy per straw is plotted. The preliminary ECT design described in this paragraph covers the $1 < |\eta| < 2.5$ range which leaves some space to fine tune the detector parameters later on. It is worthwhile to mention that the URQMD (also the HIJING) model may overestimate a total number of charged hadrons at these energies. Exact pseudorapidity coverage and occupancy studies as well as track reconstruction algorithm development will be carried out at the R&D phase, which will also allow optimization of submodule diameters and number of straw layers.

Readout will be carried out at outer straw ends, the FEE will be placed near the outer ring of the wheels.

4.1.4 Cost estimation

For the cost estimation of the EndCap Tracker we used the experience of the ATLAS collaboration. In Table 4.2 we present the cost estimation for the main items of the barrel and endcap straw detectors for the ATLAS TRT and NICA. We do not include into the table financial resources connected with the organization of the infrastructure, EndCap Tracker detector assembly area, and the test beam.

Table 4.2: Cost estimation: EndCap Tracker.

	TRT ATLAS		**NICA**		
	Number of units	**Cost per unit, k$/channel**	**Number of unit**	**Cost per unit, k$**	**Total, k$**
Total length of straws, m	∼105000		∼62000		
Number of readout channels	250000		∼64000		
Number of wheels	80		32		
Diameter of ring up to, m	2		3.3		
Straw length (max), cm	40		130		
Mechanics (k$/wheel)		62 [a]		124 [b]	3970
FE electronics and cables		0.012		0.012	576
Flexible motherboards		0.006		0.007	336
HV systems		0.005		0.005	240
Ancillary service		0.022		0.002	960
Contingency					30% [c]
Total					**7900**

[a] TRT Wheel diameter (inner/outer) is (1/2) m
[b] NICA Wheel diameters are (0.5/2.5)m, (0.8/3.4)m and (2.2/3.4)m
[c] Due to complexity of the endcap construction

4.2 Beam-Beam Counter

4.2.1 Introduction

The main role of the MPD Beam-Beam Counter is to produce a signal for the MPD Level-0 trigger. At low energies ($\sqrt{s_{NN}} = 5 \div 9\ GeV\ (Au + Au)$) it is critical to have reliable minimum bias trigger which will work from most of the central events to peripheral ones.

4.2.2 Requirements and detector configuration

The BBC consists of two scintillator annuli, installed around the beam pipe, on the east and west poletips of the MPD magnet. This corresponds to a pseudorapidity range from 1.5 to 4.5 over the full azimuth.

The BBC needs to satisfy the following requirements:

1. Since the BBC is proposed to be placed in a very high-level radiation area around the beam pipe near the interaction region, the BBC should be radiation hard.

2. The BBC is proposed to be installed just in front of the MPD magnet poletip. The expected magnetic field in this area is 0.5 T; therefore, the BBC needs to work in the high magnetic field environment.

To satisfy the above requirements, we choose the following configuration. The BBC scintillators will be cut from the 1 cm thick Kuraray SCSN-81 which is radiation resistant. Scintillation light produced within a tile is collected by four 0.83 mm diameter Y-11 doped optical fibers inserted into grooves machined within the depth of the scintillator from both surfaces. The ends of the fibers are aluminized. The grooves ramp down from the scintillator surface and have fiber guides cut to trap the optical fibers. The fibers form a nearly circular loop within a distance of 2 mm from the isolation grooves limited by the 3 cm minimum bend radius of the fiber to ensure response uniformity independent of where an ionizing particle penetrates the tile.

Regular hexagonal tiles are defined by cutting 2 mm wide and 5 mm deep optical isolation grooves in a Mercedes pattern from both sides of the scintillator and then back filling these grooves with MgO2-loaded epoxy. Since grooves are cut on both sides, the optical isolation is complete. After machining, the sides of the hexagons are covered with white reflecting paint to trap scintillation light within each tile. Each scintillator surface is then covered with 1-mil thick aluminized mylar, taped to the painted scintillator edges. The reflectors are then covered by 10-mil thick black construction paper and black electrician's tape to make the assembly light tight.

The outer radius of the BBC is about 110 cm and the inner radius is just larger than the beam pipe – 5 cm, corresponding to the clearance between the BBC and beam pipe of 1 cm (Fig. 4.6).

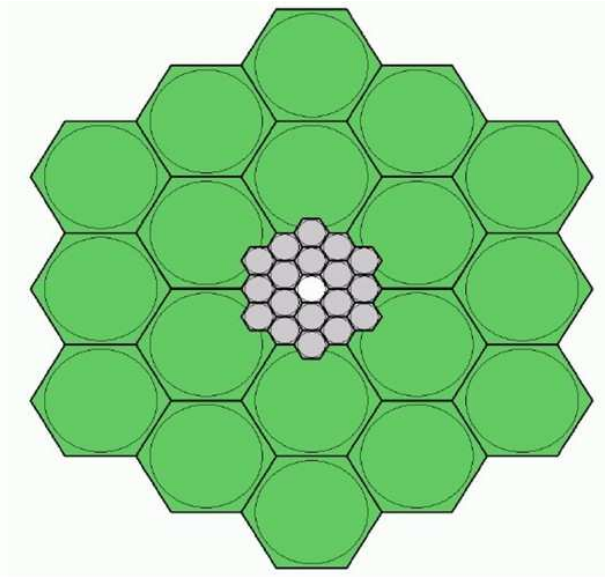

Fig. 4.6: Beam-Beam Counter front view. Small tiles can be inscribed in a circle with 12 cm diameter, large tiles are exactly four times larger. Inner empty space is left for the beam pipe.

4.2.3 Triggering capabilities

The pseudorapidity region proposed for the BBC is $1.5 < \eta < 4.5$, which is outside the TPC acceptance, and therefore will not introduce a trigger bias to physics measurements which mostly rely on the $-1.0 < \eta < +1.0$ pseudorapidity region. A minimum bias trigger will require both the BBCs (east and west) to reduce beam gas background contamination. Further cuts on the vertex position using timing information from the BBCs and signal amplitude will allow selecting clean minimum bias events.

We estimated the efficiency of the proposed BBC setup for minimum bias triggering. According to HIJING simulations, the impact parameter range for minimum bias is $0 < b < 15.8$ fm for $Au + Au$ collisions at $\sqrt{s_{NN}} = 5 \div 9$ GeV. The proposed BBC is sensitive to all above-mentioned region (Fig. 4.7). It is assumed that the Zero Degree Calorimeter (ZDC) will provide trigger capabilities in the ultraperipheral region beyond (e.g. for $b > 15.8$).

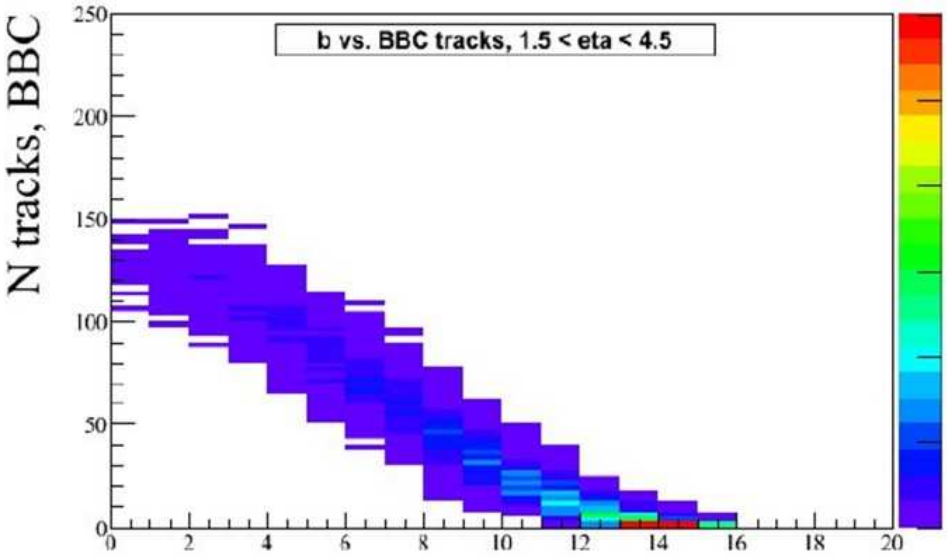

Fig. 4.7: Simulated $Au + Au$ collisions at $\sqrt{s_{NN}} = 9$ GeV. The expected number of charged tracks in the BBC acceptance vs. the impact parameter, HIJING predictions.

4.3 Zero Degree Calorimeter (ZDC)

4.3.1 Physics goal

In nucleus-nucleus collisions dense (and/or hot) hadronic matter is created in more central collisions. For centrality determination many experiments utilize the measurement of the energy of the forward-going particles (see for example [64], [65]) using the Zero Degree Calorimeters (ZDC).

In a simple geometrical picture, forward-going matter reflects the degree of centrality of each event. In a more central collision, fewer fast particles enter the forward region of the small solid angle around the beam. In peripheral collisions, a large fraction of the beam energy remains in the forward region (this scenario is schematically shown in Fig. 4.8).

In the experiments of heavy nuclei collisions, ZDCs are used for event characterization and triggering. For the study of event-by-event fluctuations experimental identification of the critical fluctuations requires a very accurate control of the fluctuations caused by the varying number of interacting nucleons due to the event-by-event changes in the collision geometry. Therefore, the number of noninteracting nucleons from a projectile nucleus should be determined with the best possible precision.

For this purpose ZDCs should have an excellent energy resolution (better than $50\%/\sqrt{E}$) and transverse uniformity of this resolution ($< 5\%$). These parameters as well as the linearity in a wide energy range ($3 \div 1000$ GeV) and the Gaussian shape of the detector signal are crucial in the appropriate description and subsequent correction of the physical parameters to the detector response.

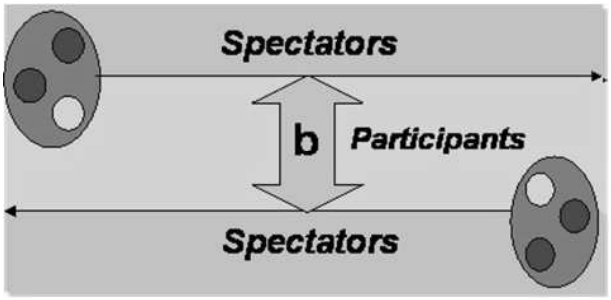

Fig. 4.8: Schematic view of the nucleus-nucleus collisions for the impact parameter **b**.

In order to exclude the fluctuations due to the varying number of the produced neutral pions in a specific nucleus-nucleus collision, ZDCs should produce equal signals from hadronic and electromagnetic showers. This could be achieved by a full compensating modular lead-scintillator calorimeter.

4.3.2 Parameters

The transverse dimension of ZDCs (at the fixed longitudinal position $L_z(ZDC)$) should be determined by the two following features of the collisions and MPD setup. The first feature is the momentum distribution of the evaporated particles (which are forward-going particles). The second feature connected with the MPD setup is the difference of the trajectories in the magnetic field of the detector for different kinds of forward-moving particles (neutrons, protons and light nuclei).

Projectile fragmentation in heavy ion collisions was studied [66, 67] at the Bevalac and SPS energies [65]. According to the hypothesis of limiting fragmentation [68], these cross sections and spectra have weak beam energy dependence above the kinetic energy of about a hundred AMeV.

Within the scenario of limiting fragmentation, the fragmentation of forward-going projectile matter at the NICA energies would be similar to those which were measured at the Bevalac [69, 70], SIS [70, 71], AGS [72, 73], SPS [65] and RHIC [64] energies. From these data it follows that the transfer momentum of the forward-going fragments has values less than 0.3 GeV/(A c).

Therefore with a zero magnetic field the radius of ZDCs is determined by the relation

$$R_{ZDC} > \frac{0.3}{p_b(GeV/(cN))} \cdot L_z(ZDC).$$

The magnetic field of the MPD detector is parallel to the beam axis (OZ). Hence, there is no reason to expect a visible deviation of the protons from the reaction axis. The results of simulation shown in Fig. 4.9 confirm this statement. One can see that proton and neutron distributions over the horizontal direction are similar, and the ZDC radius should be $R_{ZDC} = 30 \div 40$ cm.

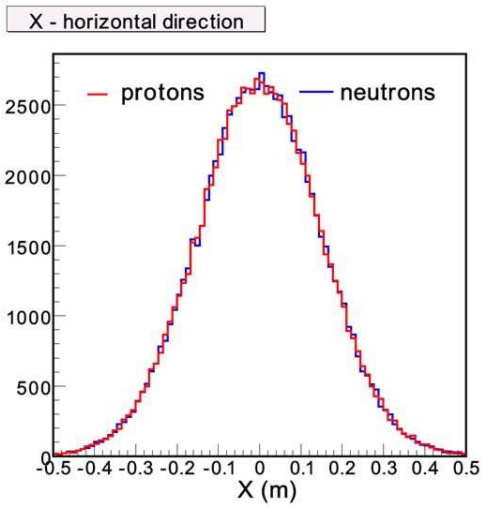

Fig. 4.9: Spectator proton (red) and neutron (blue) distributions (X is the horizontal direction) in front of ZDCs for a magnetic field of B=7 KGs.

In agreement with this, it is proposed that each ZDC should include an assembly of 76 modules of hadron calorimeters. It could be placed at a distance of about 280 cm from the interaction point (see Fig. 4.10). Each module of the hadron calorimeter consists of 60 layers of lead-scintillator sandwiches with the sampling ratio 4 : 1 (the thickness of the lead plates being 16 mm and that of the scintillator plates 4 mm) to satisfy the compensation condition. The transverse dimension of the module is 10×10 cm^2.

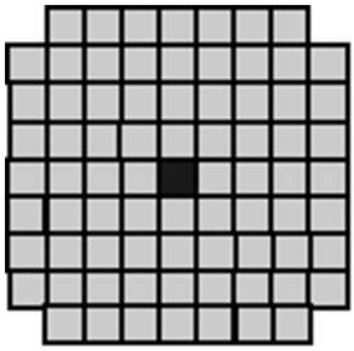

Fig. 4.10: Front view of the ZDC.

All of the 60 layers in each module are tied into one block about 120 cm in length (about 6 nuclear-interaction lengths) with a 0.5 mm thick stainless steel tape. Then this block is loaded into a box made of the same steel and covered by another similar box. The two boxes are point welded to each other. The weight of each module is about 120 kg. A view of a module is shown in Fig. 4.11.

Fig. 4.11: A view of a module of the ZDC.

Light readout is provided by the WLS-fibers embedded in the round grooves in the scintillator plates, which ensures high efficiency and uniformity of light collection over the scintillator tile within a very few percent.

WLS-fibers from each 6 consecutive scintillator tiles are collected together and viewed with a single photo detector at the end of the module.

The longitudinal segmentation in 10 sections ensures uniformity of light collection along the module as well as rejection of secondary particles from the interaction in the target.

10 AMPDs [63] per module are placed at the rear side of the module together with the front-end-electronics (amplifiers). Such a configuration ensures easy access to the AMPDs.

The dependence of energy deposited in both the ZDCs on the impact parameter (b) for minimum bias $Au + Au$ collisions at $\sqrt{s_{NN}} = 9$ GeV is shown in Fig. 4.12. From this plot one can see that the proposed construction of the ZDCs allows centrality determination with a reasonable accuracy.

4.3.3 Very forward ZDC (optional)

A possibility of using a hadron calorimeter for luminosity measurement in nucleus-nucleus collisions is discussed here. In a heavy ion collider the cross section for Coulomb dissociation of one of the ions is many times larger than the geometric cross section [74]. With such a large cross section available, it was suggested that the correlated forward-backward Coulomb dissociation would provide a clean monitor of the beam luminosity with the very forward (zero degree) calorimeters proposed for the NICA project.

The requirement of forward-backward coincidences of two neutrons greatly reduces the full counting rate due to these sources except for accidentals. The cross section of mutual Coulomb dissociation with emission of two neutrons for the NICA energy is estimated to be about 0.35–0.4 bn. For the RHIC and LHC energies this cross sections are equal to 0.45 ($Au + Au$ collision) and 0.53 ($Pb + Pb$ collisions), respectively [75].

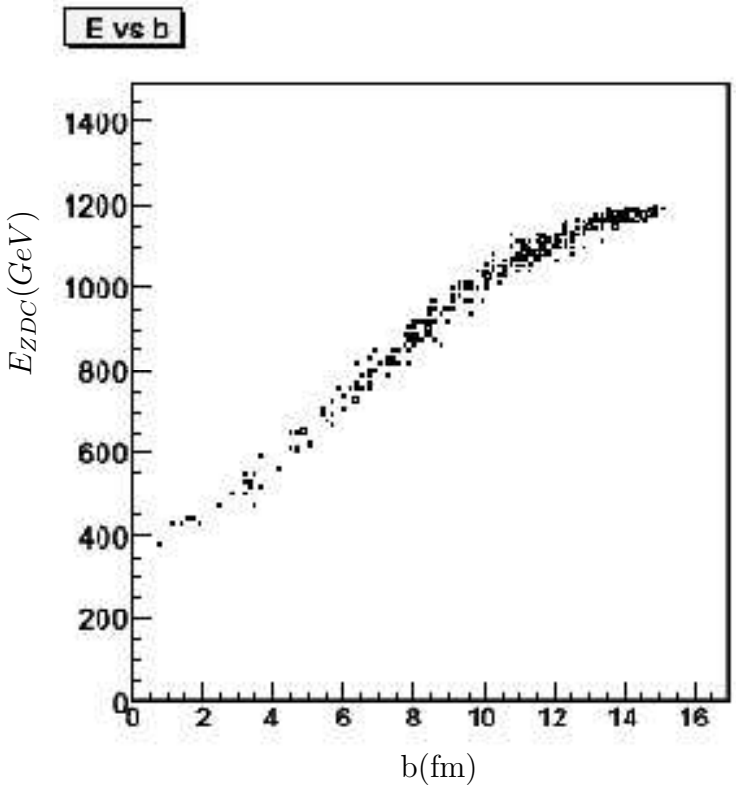

Fig. 4.12: The energy deposited in both the ZDCs as a function of the impact parameter b.

The dimension of this Very forward calorimeter should be determined using the condition that the emitted neutrons move within the polar angle at about 0.02 with respect to the beam direction. The location of the calorimeter depends on the collider design near the colliding point.

Chapter 5

Trigger, DAQ and Computing

5.1 Data Acquisition System and Trigger

The main tasks of the Data Acquisition (DAQ) and Trigger systems are:

1. maximum readout efficiency with no dead time;
2. data selection and compression;
3. independent operation of subdetectors for testing and calibration.

The general structure of the MPD detector is the same as used in STAR and ALICE. It allows subdetectors to operate independently.

All subdetectors will be connected to readout systems that include the local data collector (LDC) and detector readout electronics (DRE) boards. The central trigger processor (CTP) is common for all detectors; it generates trigger signals and synchronizes the operation of the MPD. The LDC and GDC are connected together with the DAQ network with 10Gbit Ethernet links.

The DRE module (Fig. 5.1) consists of front-end cards (FEC) and read-out card (ROC). The FEC is an electronic module that amplifies analogue signals coming from a subdetector and digitizes them. It has a pipeline structure that eliminates the subdetector dead time. The module is capable of zero suppression and data selection based on the L1 trigger. The FEC sends data to readout card by a 2.5 Gbps front-end data link (FEDL). The FEC issues a trigger request signal (TRQ) when it has any nonzero data. The readout card analyzes all TRQ signals and produces a trigger signal $L0 = f(TRQ1...TRQn)$. The DRE boards connected to subdetectors not included in the trigger decision logic have no trigger signals TRQ and L0.

The central trigger processor analyzes L0 signals from subdetector readout electronics and generates the L1 trigger signal. The readout cards move data selected by the L1 trigger to a local data collector.

Complex algorithms of data processing allow further data selection by the L2 trigger generated by the CTP. By L2 signal the data from the local data collector moves to the global data collector.

Fig. 5.2 shows the estimated data rates from subdetectors. The calculation is made assuming that the event rate is 6000 events per second and multiplicity is 500.

The development of electronics is proposed to be based on the custom ASIC designed for different detector types (PASA, ALTRO, HPTDC, etc.) and advanced data communication protocols. The electronics will contain monitoring functions for temperature, supply voltage and current.

The MPD collaboration plans to detect ion collisions during a minimum of 120 days per year starting in 2014. Assuming an overall efficiency of 60% and 6 kHz event rate,

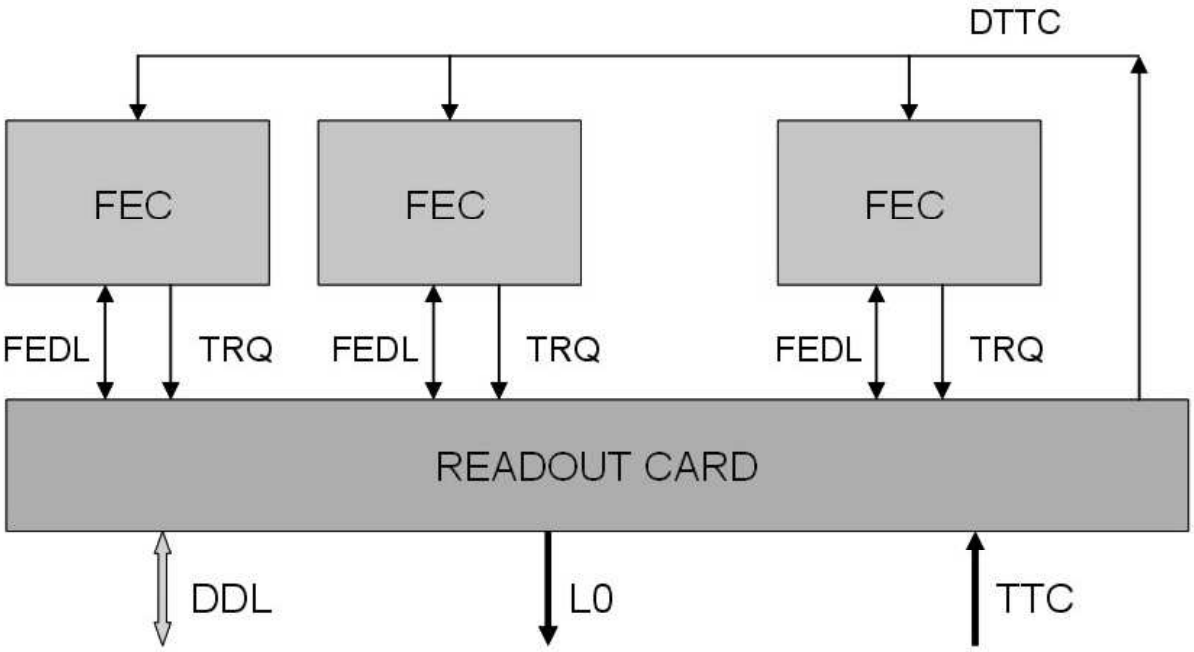

Fig. 5.1: Detector Readout Electronics.

this would allow collection of about 19 billion raw events $(U + U)$ per year. Assuming ~ 4.7 GB/s data rate from the detectors (see the previous section), the total raw data volume per year of running can be estimated as 30 PB, and 8.4 PB after compression and zero suppression. The computing resources necessary for handling of so large amount of data are estimated in this section. The estimations are based on the DAQ characteristics, previous experience, and similar estimations performed for the ALICE experiment [76].

5.2 Data Processing Model

The data processing model will correspond by the scheme presented in Fig.5.3. Data coming from the MPD subdetector PCs (directly connected with the experiment readout) are collected by the event builder on-line PC-farm (EB), and written to disk storage of the offline PC-farm after event formation via a dedicated 10 Gbps optical fiber link. Each EB writes a single "work file" every 1 minute of data taking.

After an L3 production process, the accepted events are written to the RAW file (one file per 1 minute of data taking), and then fully reconstructed. The fully reconstructed event is written to disk in a special format. At the end of the process the RAW data are copied to the disks (tapes), and finally the work files and the RAW files are deleted from the disk.

The RAW event size is estimated to be about 0.45 MB. The mean CPU time required for event reconstruction is about 2 s.

5.3 Computer Resources for the Experiment

Using the estimation of the data rate, the expected event size, and reconstruction speed, one can calculate the computer resources required for the experiment in terms of disk

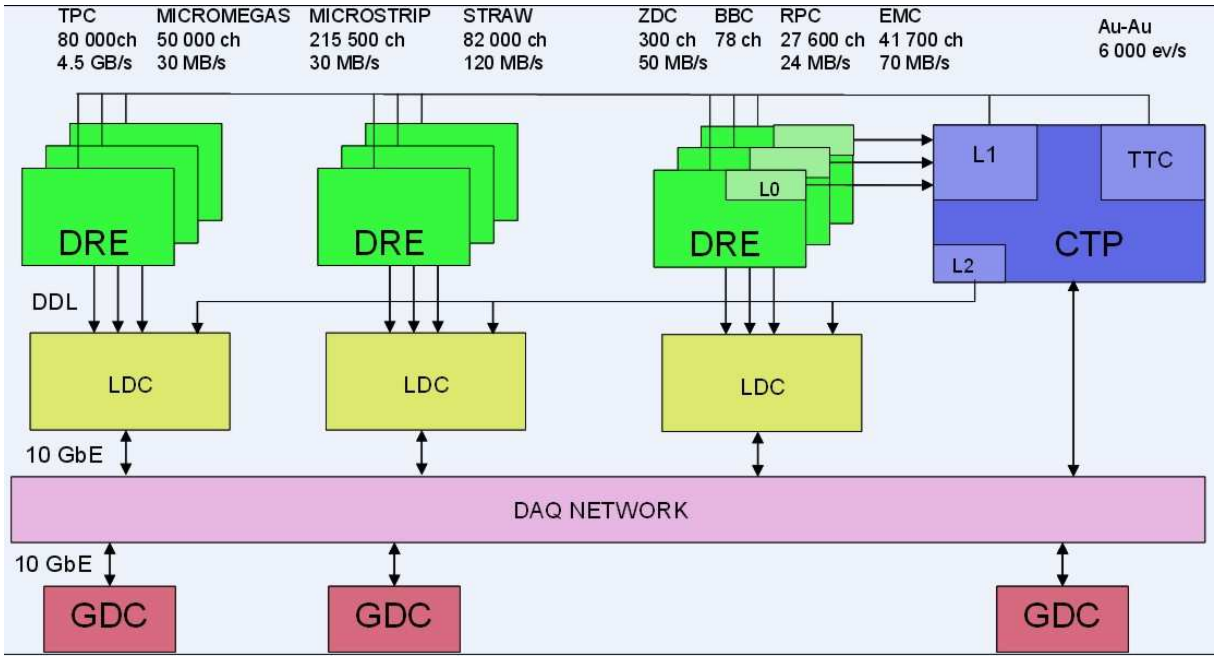

Fig. 5.2: MPD Data Acquisition System.

storage and processing power.

Assuming that no selection is applied during the first production step of L3 (before reconstruction), the expected data rate coming from the experiment is 1.3 GB/s, or about 70 TB/day. From the size of a single event of 0.45 MB, the expected trigger rate (6 kHz), and the reduction factor due to the past future protection (0.5), the total required data storage is estimated as 8.4 PB/year for RAW data. Taking into account ∼20% simulation events and the expected sizes of some compact data files produced on special request of the experts, the total required disk space is estimated as 10 PB/year.

Using the expected CPU time of 2 s/event required for reconstruction, a total time in 1K SI2K units is estimated as $37.4 \cdot 10^9$ s. This allows estimating the number of the offline 1K SI2K PCs as about 1480. Together with the online PC-farm and ∼ 20% processing power for simulation, the total number can be estimated as 1800 1K SI2K PCs. The specific character of events requests a minimum of 2 GB RAM for each CPU.

Full information and calculations for the above estimation is presented in Table 5.1.

The total estimated cost for all the necessary equipment in current prices (1 TB – \$1.5K, 1 KSI2K – \$1K) is equal to \$16.8M (without communication and remote control equipment, power supplies, conditioning system, and network infrastructure which can be estimated to be ∼ 20% of the total cost). Taking into account a gradual purchase of the equipment in 2008–2014, and the expected cost reduction factor evalated using the Moore's law [77] (see estimation in Table 5.2), the full cost is estimated as \$1.46M.

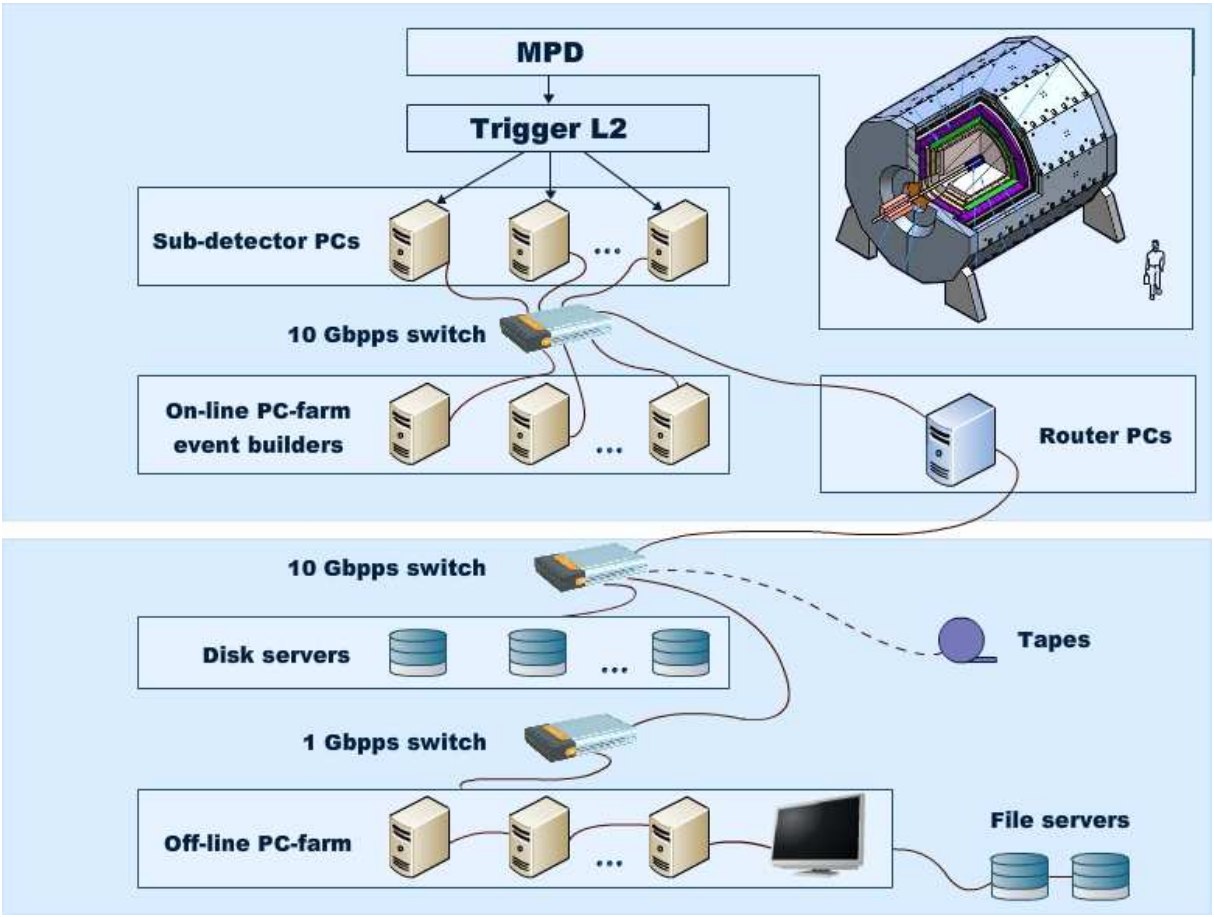

Fig. 5.3: MPD data processing model.

Table 5.1: Estimation of the necessary disk space and power of PCs.

Parameter	**Value**	**Unit**	**Value**	**Unit**
Data rate from L2	4.7	GB/s	0.0045	TB/s
Experimental run duration	120	day	10368000	s
Efficiency	60	%	0.6	
Event rate	6	kHz	6000	events/s
Past future protection	50	%	0.5	
Total number of events	**18.7**	B event	$\mathbf{1.87 \cdot 10^{10}}$	event
Mean number of tracks per event			500	track
Mean number of hits per particle (TPC + eCAL)			20	hit
Mean number of bytes per hit			45	byte
Total size of RAW data	**8.4**	PB	**8398**	TB
Total necessary disk space	**10**	PB	**10000**	TB
Mean reconstruction time per event by 1K SI2K PC			2	s
Total time per year for 1 PC	7000	hour	25200000	s
Number of 1K SI2K PCs for reconstruction			**1480**	
Total number of necessary PCs			**1800**	

Table 5.2: Cost estimation based on the Moore's law.

Year	**2008**	**2009**	**2010**	**2011**	**2012**	**2013**	**2014**	**Total**
Price of 1 TB disk space (K$)	1.5	0.75	0.38	0.19	0.1	0.05	0.03	
Part of disk space	0.001	0	0.02	0.5	0.2	0.6	0.13	
Cost	15	0	76	95	200	300	39	**725**
Price of 1K SI2K (K$)	1	0.75	0.56	0.42	0.32	0.24	0.18	
Part of computers	0.01	0.01	0.02	0.05	0.2	0.6	0.11	
Cost	18	14	20	38	115	259	36	**500**
Communications, remote control, power supply, condition and consumables (K$)	10	15	20	30	70	60	30	**235**
Total cost (K$)	**43**	**29**	**116**	**163**	**385**	**619**	**105**	**1460**

Chapter 6

Integration and Services

6.1 Facility Integration

Figure 6.1 shows the detector located on the beam line. The experimental hall 205 has two cranes (50 and 10 ton) on a single bridge. Crane capacity and coverage are sufficient to assemble the detector.

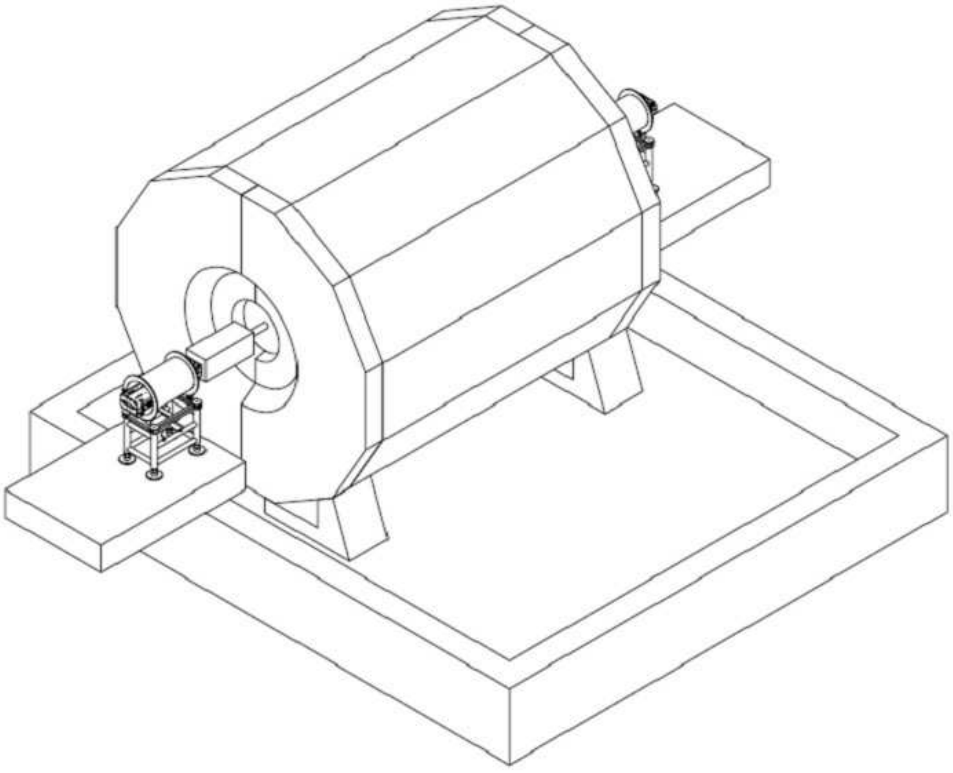

Fig. 6.1: View of the MPD detector in the operating position.

The hall 205 has concrete plates inset into the floor to carry the weight of the detector which was previously located at the MPD location; a new rail system to distribute the detector load and guide the detector transport system will have to be designed.

A building to house the cryogenic plant will be located on the existing pad outside the southern wall of the hall 205. Cryogenic tanks will be located on another pad above the hill at the end of the building. A gas mixing house and gas storage rack will also be erected near the building. The existing detector control and data analysis room appears to have sufficient space for computers and workstations. The existing shielding blocks from the TPC experiment will be used. Several new blocks will be cast to contain the cable labyrinth. A study of radiation skyshine will have to be performed to determine the

adequacy of the existing concrete curtain that completes the shield wall from the crane hook to the building roof.

Conventional systems consist of the mechanical and electrical utilities required to power and cool the detector subsystems. They also include the assembly and service fixtures and the permanent platforms that house racks and equipment that must be near the detector.

A Resource Requirement Report (RRR) detailing the detector conventional system needs and defining the conventional system interfaces with the NICA facility will be developed prior to the Conceptual Design Report.

The electric power requirement for the detector consists of filtered electric power for the subsystems and facility power to run the cryogenic plant, pumps, and other equipment. Emergency power and uninterruptable power will be supplied to critical subsystems and controls. An integrated approach to common electrical design issues will be addressed. This will include clean alternating current (AC) power distribution for all subsystems, an electrical grounding plan, cable and connector selection, rack and cableway design, and emergency power.

Chilled water distribution and control will be supplied to the detector subsystems for thermal control of heat dissipated by the electronics.

There will be an electronics platform to house racks for the data acquisition system crates and power supplies. In order to facilitate access to the racks when the detector is located on the beamline, a shield wall with cable labyrinth will be erected between the detector and the electronics platform.

The electronics platform will be transported with the detector from the assembly area to the beamline location. This will eliminate the need to disconnect the cables running between the detector and the platform after subsystem testing is completed. The area of the two story platform will be determined based on the number of racks and other equipment that must be housed on it.

6.2 Mechanical Integration

Subsystem dimension control. Overall subsystem envelope dimensions are specified to define the detector volume. The subsystem envelope dimensions describe the entire subsystem volume including space required for mechanical support, electronics, cables, machining tolerances, and assembly clearance. Figure 6.2 shows a section of the detector.

As the subsystem designs evolve, the envelope drawings will facilitate the subsystem dimension control procedure; changes to the envelope dimensions will require the approval of the Technical Board.

Cable and utility routing. Plans for cable and utility routing will be incorporated early into the design of the detector. A list of expected services (including allowance for future upgrades and packing factor) will be compiled to determine the required service space. Figure 6.3 shows the preliminary routing plan for the detector. Services to and from the silicon vertex detector are routed inside the support tube along the beam line. Drift chamber electronics readout is located only at the backward end. The drift chamber and barrel particle identification services are routed along a 5 cm gap between the calorimeter barrel and end cap. These cables are first joined by the calorimeter services, then exit via a 15 cm gap between the magnet cryostat and the magnet return iron. All services

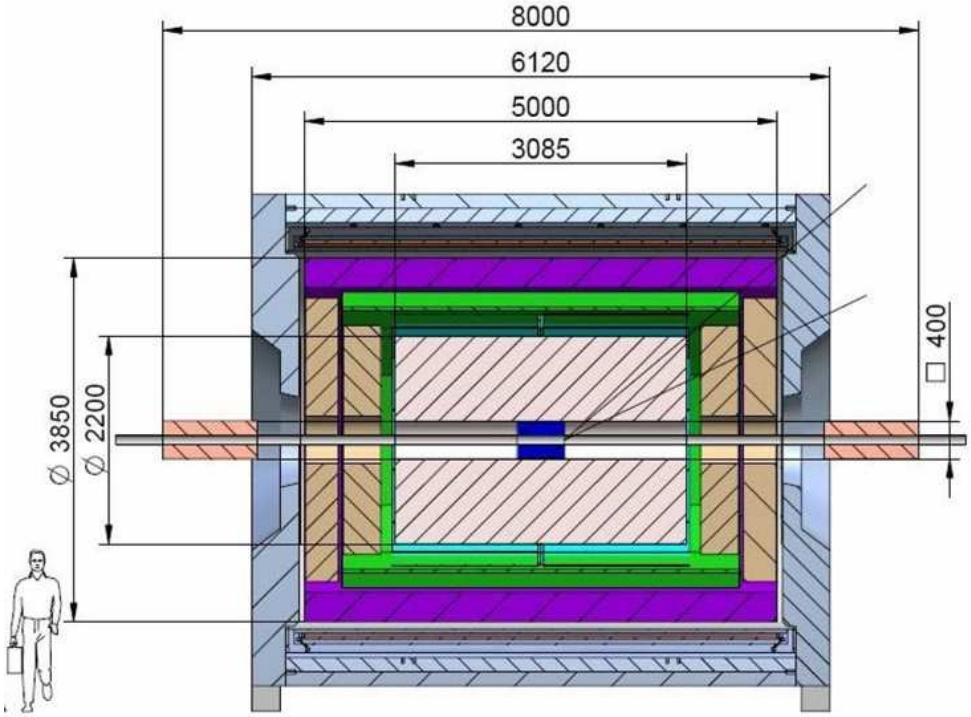

Fig. 6.2: Subsystem envelope dimensions in mm.

then exit the detector through slots between the barrel return iron and the pole tips as indicated in Fig. 6.3.

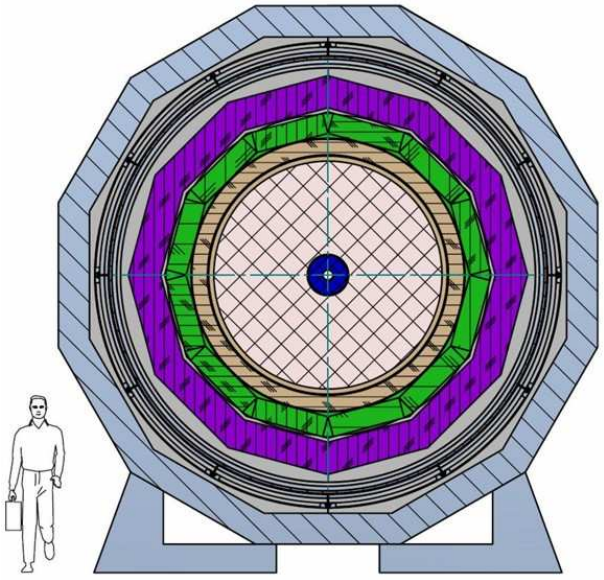

Fig. 6.3: Cross-sectional view of preliminary cable/utility routing path.

Detector assembly. Installation of the detector should be possible in the space available in the hall 205 outside the shield wall making possible to assembly the detector while

commissioning activities are going on.

The instrumented iron section will be designed to facilitate handling with the available 50-ton crane. The barrel return flux will be assembled into a self-supported structure which will house the transport mechanism. The detector transport system will be tested before completing the assembly of other subsystems. The magnet coil will be inserted into the iron with a C-lifting fixture.

The normal installation sequence would involve calorimeter, particle identification and then tracking subsystems after the solenoidal field is mapped. Depending on the installation schedule, the particle identification system could be installed inside the calorimeter before inserting the calorimeter into the coil with an insertion beam, although this is unlikely.

The drift chamber will be installed using a small insertion beam and temporarily supported on the coil support ring. The vertex detector will be mounted inside the support tube while assembling the beampipe, masks, Ql an Bl magnets are assembled. The support tube will then be installed as a single piece inside the detector.

The electronics platform will be partially assembled outside the 205 hall and brought into the hall in large pieces for final assembly after completing the installation of the detector components. When the detector has been commissioned on cosmic rays, the shield wall will be removed and the detector rolled onto the beam line. The detector alignment and final beam line installation will then take place.

Assembly and service fixtures required for common assembly work of such platforms and general lifting fixtures will be procured and maintained by the engineers and support personnel of the installation group. Fixtures such as rails or beams required for specific elements of the detector will be designed and built by each subsystem group in consultation and under the review of the Technical Coordination group.

Access requirements for the detector service are divided into two major categories, depending on the access frequency and duration. By retracting the end doors a rapid access to the inner detector will be possible at either end. Figure 2.1 shows the detector on beamline with an end door retracted. An access platform will be erected to facilitate reaching the drift chamber endplate. This procedure can be carried out without disrupting the beam line system, disconnecting cables, or removing mechanical support elements. It is expected that the door can be opened and closed in less than one shift allowing service to be performed during normal beam down periods. Access to the vertex detector is more complicated because the beam line has to be disassembled. The work can be performed during longer shutdown periods without moving the detector.

Detector interface. The integration specialist will provide oversight on issues concerning the detector and machine interface. At a strictly hardware level, this includes integration of accelerator elements (optics, pumps, etc.) in the support tube that carries the vertex detector, design of the vacuum chamber and its mating to the accelerator. At present, it is planned that the load from the support tube itself will be carried by vertical members which are themselves affixed to the magnet support ring. Any necessary detector protection interlocks (e. g. radiation monitors for the silicon vertex detectors or the drift chamber, etc.) will be the responsibility of the Technical Coordinator, who will also be responsible for coordination in implementation and testing of the Personnel Protection System (PPS). There will be a specialist in QA/QC matters who will actively monitor the fabrication and assembly of the coil and flux-return, the detector subsystems, and

their installations. This person will work with system managers, engineers, and physicists to advise on the writing of proper fabrication, assembly, and inspection procedures and protocols to assure that the detector is built in an expeditious and efficient manner.

Environmental safety and health. There will be a specialist in ES&H matters who will actively advise and monitor safety issues surrounding choice and implementation of detector technologies, safety in the experimental hall, and appropriate operational issues.

Safety analysis report. There will be a Preliminary Safety Analysis Report (PSAR) on the timescale of the submission of the Conceptual Design Report. This report will be updated as the technology choices are established. A final Safety Analysis Report (SAR) must be approved by the LHE Director and appropriate LHE ES&H staff before operation of any elements of the detector that require review in the SAR is permitted.

Electrical engineering integration. To insure that the detector electronics and data acquisition system is designed and built in a coherent and cost-effective manner, there will be a chief electrical engineer. Since the components will be designed and fabricated in many institutions, integration and the imposition of common standards will be critical. Electronics for all subsystems in the detector includes data acquisition systems, monitoring systems, control systems, and cable plant.

Software engineering integration. To insure that the data acquisition system software, the offline software, the interface, and the computing hardware is designed and put in place in a coherent and effective manner, there will be a chief software engineer. Elements of the software system will necessarily be developed at many institutions. Hardware will to some extent be distributed as well. Integration and adherence to common standards will be important to the success of the project.

6.3 Slow Controls

6.3.1 Introduction

The MPD Slow Controls system is responsible for configuring, monitoring and controlling the equipment of the experiment. Power supplies, crates and more detector-specific components are among controlled hardware devices. The system also involves computing devices (personal computers – PCs) and software being executed on those PCs. The system is designed to follow preprogrammed steps and perform automatic actions such as automatical recovering from an error state. The detector operator is able to interact with the system via user interfaces that indicate the system state and enable the operator to issue commands. Configuration information consisting of physical locations, hardware addresses, and settings for the various system states is stored in a database. Many heterogeneous subsystems are combined in a cohesive manner to ensure reliable and safe operation.

6.3.2 Technical requirements

The control system should be designed to be easily upgradeable on demand. In order to accomplish a flexible control system, the system should be designed to provide a high degree of modularity so that frequent software changes do not affect the interfaced subsystems.

There are multiple options for the core software system, Supervisory Control, and Data Acquisition System (SCADA), including several commercial software packages as well as noncommercial options such as EPICS [78, 79], developed primarily at LANL and DESY. The system will be used to connect to the hardware, acquire data, monitor performance, and react to various situations. The two most important options are EPICS and PVSS/JCOP [80], the latter approach is primarily used at CERN. The EPICS system is available under the EPICS Base license. It complies with the Open Source Definition. PVSS is a commercial software used by some companies and most importantly by the LHC experiments.

The EPICS system has several advantages: distributed IOCs and no event manager, ChannelAccess as an alternative to the DIM server, TCP/IP, a configuration database with capabilities of mass configuration, event logging and alarm handler, a lot of freely available tools and applications and, of course, a large community. Communication performance is bounded by the channel access protocol, TCP/IP packet overhead, and the physical communication media. Channel access makes efficient use of the communications overhead by combining multiple requests or responses. For point to point connections, 1000 monitors per second will use about 3% of the 10 Mbit Ethernet band-width ($\approx$ 30 bytes per monitor), as it is shown in Fig. 6.4.

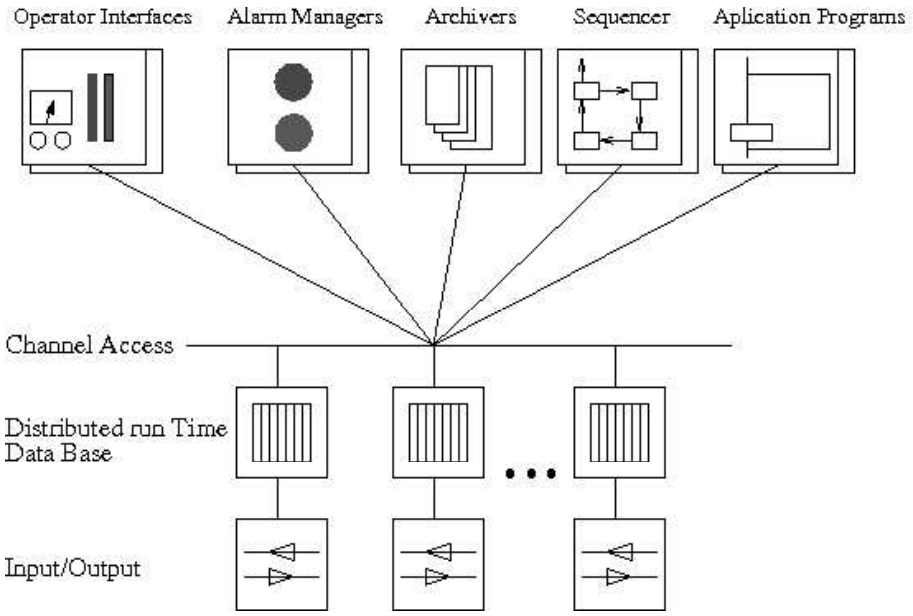

Fig. 6.4: EPICS Software Architecture.

Many features of the PVSS system are similar to those available in the EPICS framework. PVSS provides a set of drivers and libraries. The main difference between those

packages is the event-managing system which collects data from the IOCs and provides an event service to the subscribed event-managing services. PVSS also provides a true object-orientated API to the IOC data (see Fig. 6.5).

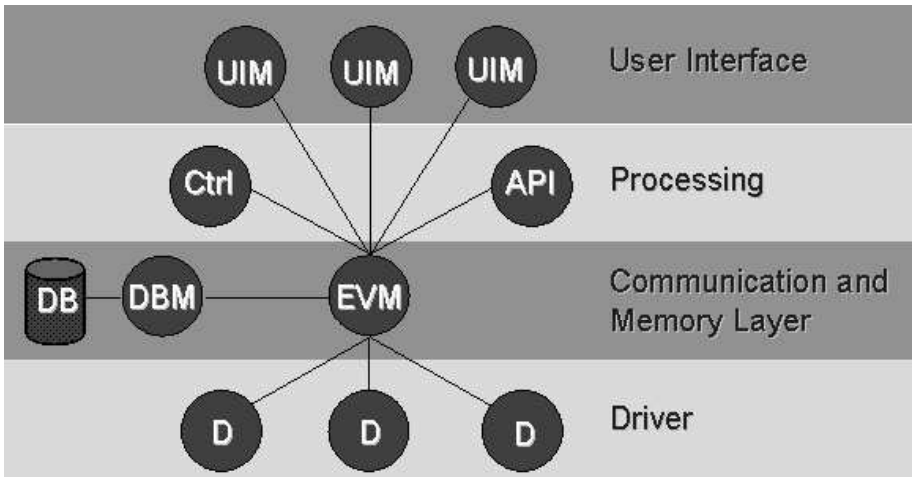

Fig. 6.5: PVSS Software Architecture (EVM Event Manager, DBM – Data Base Manager, API – Application Programming Interface).

Also such an important issue as system security must be addressed. The whole control system will use a private Ethernet network to communicate among its parts and communicate at a higher level to the data acquisition system. The private network will be accessible in only a limited mode from the rest of the Internet. This will prevent an anonymous user from running a portion of the experiment in an unforeseen way. However, the ability to quickly communicate news items or experimental data is quite feasible and appropriate.

If the development and support will be outsourced to a commercial company, the cost will include the initial license, development/implementation, ongoing software support, and possible license updates. Alternatively, the development can be carried out by the collaboration and partially outsourced to a company. A good example of the partial outsourcing approach is a project carried at KEK-B [81]. This would reduce the overall cost but would require additional Full Time Equivalents (FTEs) committed to the project. Based on experience at the STAR experiment, the initial system development can be done with two FTEs within two years. The project support will require half of an FTE during the lifetime of the project. The software support and upgrade license fee is equivalent to one-and-a-half FTE which is about the manpower necessary to support new hardware and to upgrade EPICS based system.

6.3.3 Summary

Depending on the requirements and funds available, the solution can combine a collaborative effort and commercial solution. Custom hardware, special timing requirements and requirement on availability of the source code will force the project to be developed mainly by the collaboration. As long as EPICS stays an active collaboration with robust and rapid development, it will be preferable over the commercial software solution.

6.3.4 Cost estimate

Assuming that the project will be based on the open-source EPICS software, the total initial cost is estimated to be at the level of $\approx$ 280 k$ to complete. This includes cost for two FTE for two years to develop and support the initial Slow Controls System, $\approx$ 160 k$, hardware cost estimated to be $\approx$ 120 k$. Annual ongoing cost is expected to be at the level of $\approx$ 20 k$. The exact cost would be calculated upon the final detector design.

Chapter 7

Physics and Detector Performance

7.1 Detector Simulation Software Packages

The software framework for the MPD experiment (mpdroot) is based on the FairRoot [82] framework to provide a powerful tool for detector performance studies, development of pattern recognition algorithm for reconstruction and physics analysis. Recently, this framework has already been used by the CBM [83], PANDA [84] and other experiments in GSI.

In the applied framework the detector response simulated by a package currently based on the Virtual Monte Carlo concept [85] allows performing simulation using Geant3, Geant4 or Fluka without changing the user code. The same framework is used for simulation and data analysis.

The schematic design of the FairRoot and mpdroot framework is shown in Fig. 7.1.

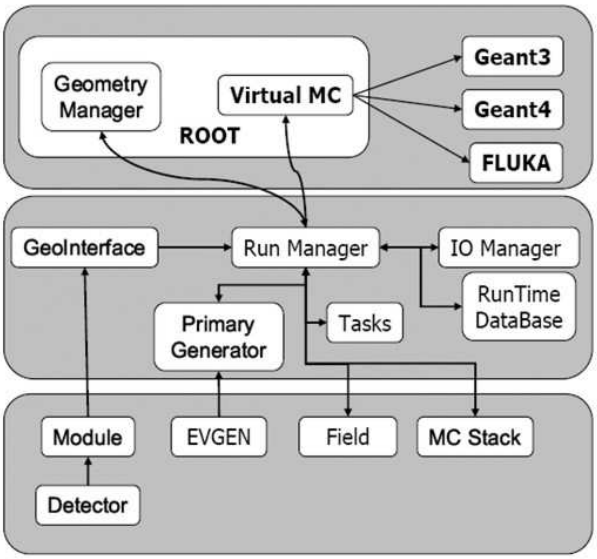

Fig. 7.1: Schematic view of the general part of FairRoot framework.

A useful advantage of the framework is that a new geometry reader was developed for it. The input of this reader is in the form of TGeoVolumes (Root Geometry format). This reader is used by the PANDA collaboration to read the detector geometries which are converted from the Step file format (CAD system) to the Root format. After importing geometry data the database (MySQL) can be used to efficiently store the detector geometry, materials and parameters. The view of the MPD detector geometry implemented in the framework is shown in Fig. 7.2.

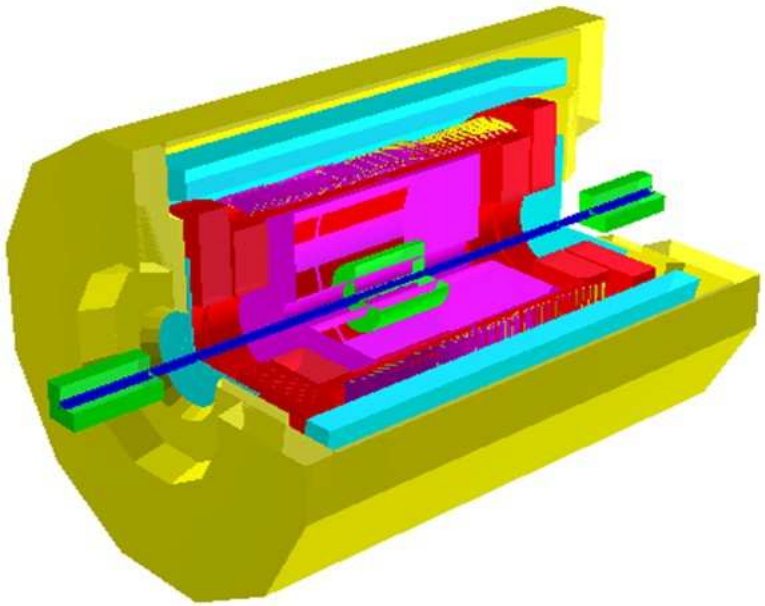

Fig. 7.2: A view of MPD geometry from the simulation package.

For a realistic simulation of various physics processes an interface to the Monte Carlo event generators for nuclear collisions (UrQMD [86] and FastMC [25]) was provided. Superposition of minimum-bias events can also be generated with the programme. The detector performances given in the following chapters was obtained with a simpler version of the detector geometry. A more detailed detector description and careful cross checks with the program described above will be made in future.

7.2 Event Reconstruction

An example of an event for the $Au + Au$ collision at $\sqrt{s_{NN}} = 9$ GeV is shown in Fig. 7.3. The event of central $Au + Au$ collision at energies of the NICA collider contains up to 1000 charged particles. The challenge is to reconstruct all these particles from the particle hits measured in various subdetectors of the MPD experiment.

The data produced by the event generators contain the full information about the generated particles: particle identification (PID) and momentum. As these events are processed via the simulation chain, the information is disintegrated and reduced to that generated by particles when crossing a detector. The reconstruction algorithms restore the information about the particle trajectory and identity from the information contained in the raw detector data. In order to evaluate the software and detector performance, simulated events are processed through the whole cycle and finally the reconstructed information about particles is compared with the information taken directly from the Monte Carlo generation.

The process of event reconstruction consists of several independent steps. In the first step, the data of each detector are converted to spatial coordinates or space points, depending on type of a detector. The next step is a local pattern recognition within sub-detectors. The third step consists of global track finding and fitting to perform a full event reconstruction in the experimental setup.

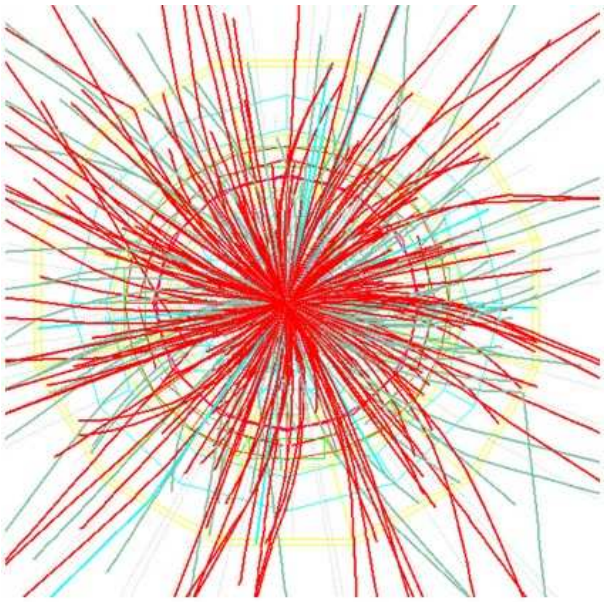

Fig. 7.3: Event of $Au + Au$ interaction at $\sqrt{s_{NN}} = 9$ GeV generated within the UrQMD model and simulated in the mpdroot framework.

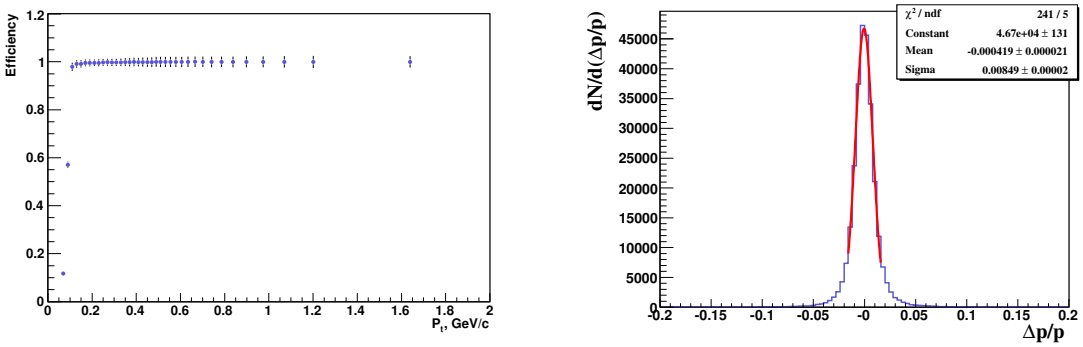

Fig. 7.4: Efficiency of track finding in TPC (left). Relative momentum errors for all particles (right).

At the current stage of simulation of the detector responses we study only the feasibility of event reconstruction with the TPC detector as the main tracking device. The track finding efficiency was evaluated for all charged particles entering the TPC acceptance with the transverse momentum $p_t \geq 100$ MeV/c. In the case of homogeneous magnetic field inside the TPC a reasonable choice for pattern recognition to find hits belonging to the track is the conformal mapping method [87]. As it is shown in the Fig. 7.4, this method gives a good efficiency for track finding in high multiplicity events. A standard Kalman filter implementation for track fitting [88] is used, and relative momentum errors of $\Delta p/p \approx 1 - 2\%$ can be achieved for particles in the considered momentum range, as shown in Fig. 7.4.

7.3 π/K Separation with TOF Detector

For estimation of the identification efficiency and contamination level we have to keep in mind that performance of the TOF system depends, besides the intrinsic time resolution, on the accuracy of particle momentum measurement by the whole detector and track length measurement by the tracking system. The mass of the particles generated by UrQMD is reconstructed by the formula

$$M = \frac{p}{\gamma\beta} = p\sqrt{\frac{1-\beta^2}{\beta^2}} = p\sqrt{\frac{1-\frac{L^2}{t^2c^2}}{\frac{L^2}{t^2c^2}}} = p\sqrt{\frac{t^2c^2}{L^2} - 1},$$

where p is particle momentum, L is track length, t is particle time of flight, c is the speed of light.

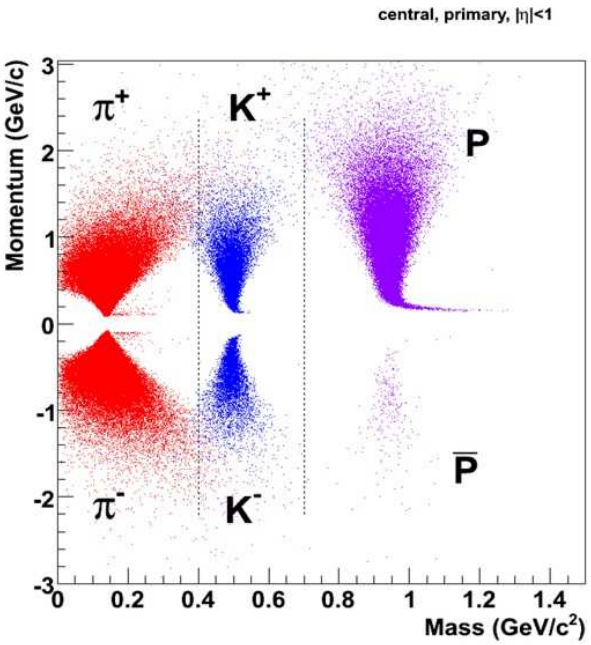

Fig. 7.5: Mass separation with the TOF detector as a function of momentum (central collisions, primaries).

A momentum resolution $\Delta p/p = 1\%$ and a time resolution 100 ps were used for the mass reconstruction. The accuracy of track length reconstruction was taken 0.5 μm. Later on we intend to use a more realistic number.

In Fig. 7.5, mass separation capabilities of the TOF MPD system are presented. We made crude estimation of the efficiency and contamination level. We put simple boundaries as straight lines on the Figure to define type of the particles. We consider that particles of a given type outside the appropriate boundaries result in a loss of efficiency, and particles of wrong type in a region result in contamination. The results for pions, kaons and protons are presented in Fig. 7.6.

Contamination levels of kaons K_{cont} in the pion region and of pions in the kaon region π_{cont} was calculated as follows:

$$K_{cont} = \frac{N_K}{N_K + N_\pi}, \quad \pi_{cont} = \frac{N_\pi}{N_K + N_\pi}.$$

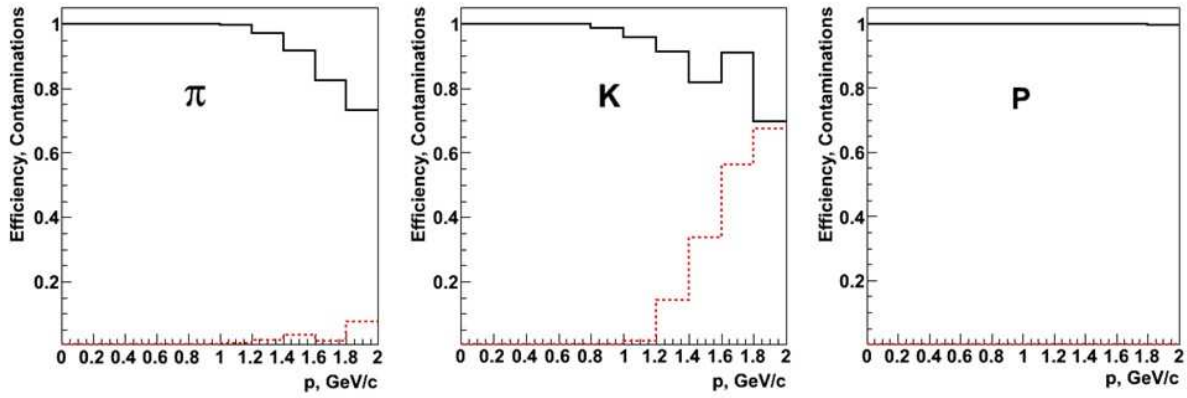

Fig. 7.6: Particle identification efficiencies (solid lines) and contamination levels (dotted lines) as functions of momentum for central collisions, primary particles, B=0.5 T, $|\eta| < 1$.

From Fig. 7.6 one can see that the contamination level to the identified K mesons steeply increases at the momentum larger than 1.2 GeV/c, where it has a value about 15%. The efficiency of identification is about 90%.

7.4 Study of Hyperons

Feasibility of the Λ-hyperon detection is illustrated for central $Au + Au$ collisions at $\sqrt{s_{NN}} = 7$ GeV. The invariant mass spectrum for proton-pion pairs selected in events generated by the UrQMD is shown in Fig. 7.7. To simulate the resolution of track reconstruction, each component of particle momenta was artificially biased by Gaussian values with 1% relative errors of momentum.

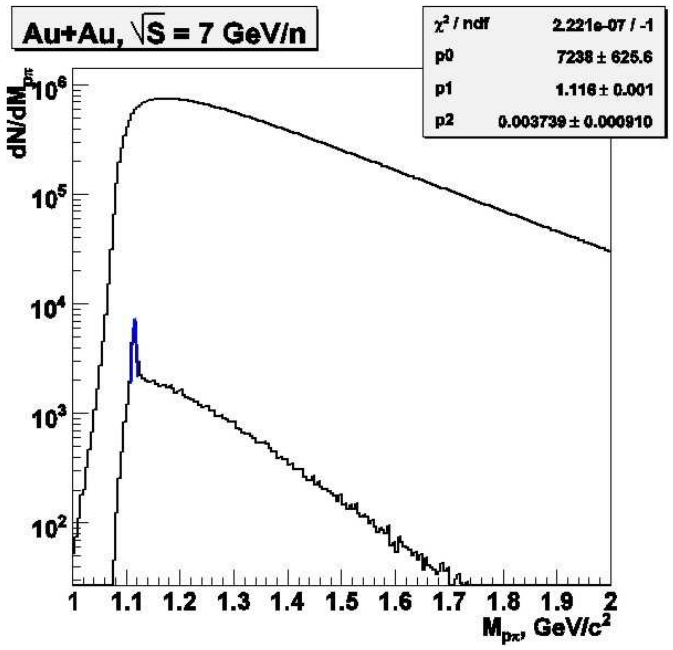

Fig. 7.7: Invariant mass spectrum for $Au+Au \to p\pi^-$ in central Au+Au collisions at $\sqrt{s_{NN}} = 7$ GeV; upper curve is for all $p\pi^-$ combinations, lower curve is for $p\pi^-$ pairs from the Λ vertex.

Chapter 8

The Total Cost

A preliminary cost estimation for the MPD is presented in Table 8.1. The presented numbers are calculated as sums of the subdetector element costs. However, those estimations are based on different approaches taking into account different stages of R&D, which are either already available or just starting from scratch. It is expected that the future collaboration will re-evaluate the corresponding numbers which should be adopted to the regulations and requirements of the participating institutions.

Table 8.1: Preliminary rough cost estimation.

Sub Detector		**Cost, k$**	**Cost, k$**
Magnet		3 138	
TPC		9 500	
Silicon IT		3 600	
MICROMEGAS	*optional*		750
Outer tracker	*optional*		1 830
TOF (barrel)		4 000	
EmCal ("shashlyk")		5 624	
EmCal (crystal)	*optional*		14 356
End Cap Tracker		7 900	
BBC		390	
ZDC		598	
DAQ		3 000	
Slow control		280	
Computing		1 460	
Engineering		2 000	
	Sum:	**41 490**	

Acknowledgements

We are grateful to D.K. Dryablov, A.S. Khvorostukhin, E. Pershina, I.A. Rufanov, T.M. Solovjeva, A.G. Solovjev for the help in preparation of the present document, and to M.A. Kozhin and A.V. Friesen – for the participation in the simulation and design.

Bibliography

[1] A. N. Sissakian, A. S. Sorin, M. K. Suleimanov, V. D. Toneev, and G. M. Zinovjev, Proceedings of the 8th International Workshop 'Relativistic Nuclear Physics: From Hundreds MeV to TeV', Dubna 2005, Russia, 306 (2006), nucl-th/0511018.

[2] A. N. Sissakian, A. S. Sorin, M. K. Suleimanov, V. D. Toneev, and G. M. Zinovjev, *Bogoliubov Laboratory 50 years* (JINR, 2006), pp. 73 – 95, nucl-ex/0601034.

[3] A. N. Sissakian, A. S. Sorin, M. K. Suleimanov, V. D. Toneev, and G. M. Zinovjev, Part. Nucl. Lett. **5**, 1 (2008), nucl-ex/0511018.

[4] A. N. Sissakian, A. S. Sorin, and V. D. Toneev, Proceedings of the 33rd International High Energy Physics conference, ICHEP'06, Moscow, Russia **1**, 421 (2006), nucl-th/0608032.

[5] A. Sissakian *et al.*, *Design and Construction of Nuclotron-based Ion Collider fAcility (NICA), Conceptual design report* (JINR, Dubna, 2008).

[6] A. Andronic, P. Braun-Munzinger, and J. Stachel, Nucl. Phys. **A772**, 167 (2006), nucl-th/0511071.

[7] J. Cleymans and K. Redlich, Phys. Rev. Lett. **81**, 5284 (1998), nucl-th/9808030.

[8] Z. Fodor and S. Katz, JHEP **404**, 50 (2004), hep-lat/0402006.

[9] M. Stephanov, (to be published in PoS Lat2006) **024**, hep-lat/0701002.

[10] G. S. F. Stephans, J. Phys. **G32**, 447 (2006), nucl-ex/0607030.

[11] G. Stephans, RHIC-Workshop (2006), https://www.bnl.gov/riken/QCDRich/.

[12] P. Senger, J. Phys. **G30**, 1087 (2004).

[13] *FAIR Baseline Technical Report* Vol. 1 (GSI, 2006).

[14] NA61, A. Laszlo, arXiv:0709.1646.

[15] The NA61/SHINE homepage [http://na61.web.cern.ch].

[16] V. Skokov and V. Toneev, Phys. Rev. C **73**, 021902 (2006), nucl-th/0509085.

[17] A. Khvorostukhin, V. Skokov, V. Toneev, and K. Redlich, Eur.Phys. J. **C 48**, 531 (2006), nucl-th/0605069.

[18] T. Satagota *et al.*, (to be published in the Proc. of 4th Int. Workshop on Critical Point and Onset Deconfinement, Durmstadt, 2007) , 0710.2485.

[19] R. Hunbury-Brown and R. Twiss, Phil. Mag. **45**, 663 (1956).

[20] R. Hunbury-Brown and R. Twiss, Nature **178**, 1046 (1956).

[21] E891, S. Ahmad *et al.*, Phys. Lett. **B 382**, 35 (1996).

[22] E895, C. Pinkenburg *et al.*, Nucl. Phys. **A698**, 495 (2002), nucl-ex/0104025.

[23] NA49, A. Mischke *et al.*, J. Phys. **G 28**, 1761 (2002).

[24] NA49, A. Mischke *et al.*, Nucl.Phys. **A 715**, 453 (2003).

[25] N. S. Amelin *et al.*, Phys. Rev. **C74**, 064901 (2006), nucl-th/0608057.

[26] J. Thomas, News about RHIC, in *Proc. of SQM-06@UCLA*, 2006.

[27] STAR, *STAR: Conceptual design report for the Solenoidal Tracker at RHIC* , chap. 4C-TPC, BNL-PUB-5347.

[28] ALICE, (1995), CERN-LHCC-95-71.

[29] G. A. Feofilov *et al.*, Inner Tracking System for ALICE: Conceptual Desing of Mechanics, Cooling and Alignement, in *Proceedings of the International Workshop on Advanced Materials for High Precision Detectors, Advance Proceedengs*, edited by C. H. B. Nicquevert, pp. 73–81, Geneve, 1994, CERN 94-07.

[30] O. Nakagawa *et al.*, Journal of Electronic Materials **18**, 633 (1989).

[31] A. P. de Haas *et al.*, Aluminum microcable technology for ALICE silicon strip detector: status report, in *Proceedings of the Eighth Workshop on Electronics for LHC Experiments*, Colmar, France, 2002, CERN/LHCC 2002-034.

[32] M. Bregant *et al.*, Nucl. Intr. Meth. in Phys.Res. **A 569**, 29 (2006), and refences therein.

[33] C. Hu-Guo *et al.*, The HAL25 front-end chip for ALICE silicon strip detectors, in *Proceedings of the Seventh Workshop on Electronics for LHC Experiments*, Stockholm, Sweden, 2001.

[34] C. Hu-Guo *et al.*, Test and evaluation of HAL25: the ALICE SSD front-end chip, in *Proceedings of the Eighth Workshop on Electronics for LHC Experiments*, Colmar, France, 2002, CERN/LHCC 2002-03.

[35] Y. Giomataris, Nucl.Instr.and Meth. **A419**, 239 (1998).

[36] D. Arogancia *et al.*, (2007), arXiv:0705.2210v1.

[37] V. N. Bychkov *et al.*, Nucl.Instr. and Meth. in Phys.Res. **556**, 66 (2006).

[38] S. G. Basiladze *et al.*, Submitted to Prib.Tekh.Eksp. .

[39] ATLAS, (1997), CERN-LHCC-97-17.

[40] V. Davkov *et al.*, Annual Report 2006 **FZD-461**, 34 (2007).

[41] V. Davkov *et al.*, Part.Nucl.Lett. **4(140)**, 545 (2007).

[42] K. Davkov *et al.*, submitted to Nucl.Instr. and Meth. **A** (2007).

[43] ALICE, (2000), CERN-LHCC-2000-012, ALICE TDR 8.

[44] ALICE, P. Cortese *et al.*, (2002), CERN-LHCC-2002-016, Addendum to the ALICE TDR 8.

[45] *CBM Technical Status Report 2006* .

[46] K. Ikematsu *et al.*, (1998), arXiv:physics/9802024 v1.

[47] F. Geurts *et al.*, Nucl.Instr.Meth. **A508**, 60 (2003).

[48] H. Alvarez-Pol *et al.*, Nucl.Instr.Meth. **A535**, 277 (2004).

[49] R. Novotny *et al.*, IEEE Trans. Nucl. Sci. **47**, 499 (2000).

[50] L. Aphecetche *et al.*, NIM **A499**, 521 (2003).

[51] G. Atoian *et al.*, Nucl.Instrum.Meth. **A531**, 467 (2004).

[52] S. Barsuk, in *XI Int.Conf. Calorimetry in High Energy Physics*, Italy, 2004.

[53] D. Karlen *et al.*, Nuclear Physics **B 159**, 91 (2006).

[54] W. van Loo, Phys. Stat. Sol. **28**, 227 (1975).

[55] W. Moses and S. E. Derenzo, IEEE Trans. Nucl. Sci. **36**, 173 (1989).

[56] M. Kobayashi *et al.*, Nucl. Instrum. Methods **A333**, 429 (1993).

[57] V. G. Baryshevsky *et al.*, Nucl. Instrum. Methods **A322**, 231 (1992).

[58] P. Lecoq *et al.*, (1994), CMS TN/94-308.

[59] Y. Borodenko *et al.*, in *Int. Conf. on Nuclear Tracking and Radiation Measurements*, Amsterdam, 1995.

[60] M. N. Khachaturian, Particles and Nuclei **34**, 1316 (2003).

[61] ALICE, Answers to LHCC Questions, Internal Note ALICE 93-33.

[62] A. Fyodorov *et al.*, Internal Note ALICE 94-29.

[63] Z. Sadygov, Nucl.Instr.Meth. **A567**, 70 (2005).

[64] C. Adler *et al.*, NIM **A 499**, 433 (2002).

[65] NA49, H. Appelshauser *et al.*, Eur. Phys. J. **A 2**, 383 (1998).

[66] H. H. Heckman *et al.*, Phys. Rev. Lett. **28**, 926 (1972).

[67] D. E. Greiner *et al.*, Phys. Rev. Lett. **35**, 152 (1975).

[68] J. Benecke *et al.*, Phys. Rev. **188**, 2159 (1969).

[69] W. Christie *et al.*, Phys. Rev. **C 48**, 2973 (1993).

[70] G. Kunde *et al.*, Phys. Rev. Lett. **74**, 38 (1995).

[71] A. Schauttauf *et al.*, Nucl. Phys. **A 607**, 457 (1996).

[72] J. Barrette *et al.*, Phys. Rev. **C45**, 819 (1992).

[73] M. Cherry *et al.*, Phys. Rev. **C 52**, 2652 (1995).

[74] A. Baltz, M. Hoades-Brown, and J. Weneser, Phys. Rev. **A 54**, 4233 (1996).

[75] J. Anthony, C. Chellis, and S. N., (1998), arXiv:nucl-ex/9801002.

[76] ALICE, P. Cortese *et al.*, (2005), CERN-LHCC-2005-018.

[77] G. Moore, Electronics **38** (1965).

[78] http://www.aps.anl.gov/epics/.

[79] http://aps.anl.gov/epics/EpicsDocumentation/EpicsGeneral/epicsX5Farch-1.html.

[80] http://itcobe.web.cern.ch/itcobe/Services/Pvss/welcome.html.

[81] http://epaper.kek.jp/ica03/PAPERS/TH501.PDF.

[82] M. Al-Turany, D. Bertini, and I. Koenig, *CBM Simulation and Analysis Framework, GSI scientific report 2004* (GSI, 2004), FAIR-EXP-07.

[83] http://www.gsi.de/fair/experiments/CBM.

[84] http://www-panda.gsi.de.

[85] http://alisoft.cern.ch/.

[86] S. Bass *et al.*, Prog. Part. Nucl. Phys. **41**, 225 (1998), nucl-th/9803035.

[87] P. Yepes, NIM **A 380**, 582 (1996).

[88] R. Fruhwirth, NIM **A 262**, 444 (1987).